Università di Pisa

SCUOLA DI INGEGNERIA
Corso di Laurea Magistrale in Ingegneria Meccanica
Dipartimento di Ingegneria Civile ed Industriale

Tesi di laurea magistrale

Design of the cooling system of the Mu2e electromagnetic calorimeter at Fermilab

Candidato:
Federico Crisci
Matricola 481877

Relatori:
Prof. Ing. Marco Beghini
Dott. Ing. Fabrizio Raffaelli
Prof. Simone Donati

Anno Accademico 2016-2017

A nonno Sauro
e a me stesso

Abstract

This paper is my Master Thesis in Mechanical Engineering. My research project has been the design of the Mu2e electromagnetic calorimeter cooling system. The physics goal of the Mu2e experiment at Fermilab is the search for the neutrino-less coherent conversion of a muon to an electron in the field of an aluminum nucleus, a physics process which would be the unambiguous evidence of the existence of physics beyond the Standard Model. The calorimeter has the fundamental function of measuring the electrons energy, time and position of impact which aids significantly the reconstruction of particle trajectories. It is a challenging detector, designed to operate in a hostile environment: large magnetic field, harsh radiation level and in vacuum.

Chapter 1 provides a brief description of the Mu2e experiment physics motivation and the employed experimental techniques, along with a description of the Fermilab accelerator complex and the Mu2e experimental apparatus, which includes the tracker, the electromagnetic calorimeter, the cosmic ray veto and the data acquisition system.

Chapter 2 reports the technical specifications and a more accurate description of the electromagnetic calorimeter, including mechanics and electronics systems design. Since this is relevant to quantify the amount and distribution of dissipated power and to design of the cooling system, photo-sensors, front-end and power electronics, as well as the data acquisition boards, are described in more detail.

Chapter 3 describes the design of the part of the cooling system relative to the data acquisition boards and crates and the supply and return manifold connected to the crates. A detailed hydraulic analysis of the circuit has been performed

Chapter 4 discusses the thermal simulation and analysis of the DAQ boards and crates. I have estimated the thermal resistance of all the components of the thermal circuit, electronic devices, printed circuit boards, aluminum parts, and the thermal interfaces which, in vacuum, require a dedicated and accurate study.

Chapter **??** describes the first 10% reduced-scale prototype of the calorimeter. I have worked on the design and hydraulic tests of the front-end cooling system.

Chapter 6 reports the conclusions and a description of the future development of my research activity.

Contents

ingraziamenti

Ringrazio i miei genitori, perché mi sono stati vicini in tutti questi anni, nella buona e nella cattiva sorte senza mai farmi mancare niente, come un porto sicuro nella tempesta.

Ringrazio i miei nonni, in particolar modo nonno Sauro, il quale mi ha insegnato ad accettare con umiltà le sconfitte e a celebrare con pacatezza i successi. Sarebbe molto fiero di me in questo giorno.

Ringrazio i miei amici, che da sempre mi attribuiscono doti intelltuali di gran lunga più elevate di quelle che realmente possiedo.

Ringrazio il professor Beghini, che mi ha dato preziosi consigli nella stesura di questo lavoro e che è stato una figura guida nel mio percorso universitario.

Ringrazio Fabrizio Raffaelli, per i suggerimenti tecnici che mi ha fornito ma soprattuto per l'immensa quantità di conoscenze che mi ha trasmesso in questi pochi mesi di collaborazione.

Ringrazio il professor Donati, non solo per il sostegno e l'attenzione con cui ha seguito il lavoro della mia tesi ma anche per avermi concesso la scorsa estate l'opportunità di partecipare alla Summer School al Fermilab, ancora oggi la più bella esperienza che abbia mai vissuto.

Ringrazio infine me stesso, che nonostante gli alti ed i bassi della vita non mi sono mai perso.

Introduction

The physics motivation of the Mu2e experiment at Fermilab is the search for the neutrinoless coherent conversion of a muon to an electron in the field of an aluminum nucleus, a physics process which would be the unambiguous evidence of the existence of physics beyond the Standard Model. The experiment is currently in construction and is expected to begin data taking in the year 2021. The experimental technique employed by Mu2e has been designed to improve the sensitivity of the search of four orders of magnitude with respect to previous experiments. Mu2e is a complex experimental apparatus composed of several independent detectors, including a straw-tracker and a crystal-based electromagnetic calorimeter.

The calorimeter has been designed and will be constructed by a collaboration among the Istituto Nazionale di Fisica Nucleare (INFN), the California Institute of Technology and Fermilab. The calorimeter has the fundamental function to measure the electrons energy, time and position of impact. It is a challenging detector, designed to operate in a hostile environment: large magnetic field, harsh radiation level and in vacuum. Moreover, the detector will be accessible for maintenance only for an extremely limited number of weeks in one year. Operation in vacuum has an immediate consequence on the electronics operation: a dedicated cooling system is required. The high radiation level requires radiation hard electronic components, which show an increase of power dissipation with the absorbed dose. All these possible effects have to be taken into account in the design of the cooling system.

I have worked with the INFN Pisa, INFN-Frascati and the Fermilab groups, and I have participated to several meetings, where I have reported the progress of my work. My Master Thesis research project focuses on the design and the thermal analysis of the calorimeter electronics cooling system, in particular the data acquisition electronics, hosted in the DAQ crates. I have followed the manifacturing of the DAQ crate design both at INFN mechanical workshop and VCS S.r.l. I have also performed preliminary pressure loss tests of the cooling system of a 10% reduced-scale mockup calorimeter.

Chapter 1

The Mu2e experimental apparatus

The Standard Model of particle physics provides an excellent interpretation of experimental data which has been tested to high precision and in a wide energy range [1] [2]. According to the model, the fundamental constituents of matter are quarks and leptons. Quarks combine to form composite particles called hadrons, the most stable of which are protons and neutrons, the components of atomic nuclei. Leptons exist in two main classes: charged leptons, also known as the electron-like leptons, and neutral leptons, better known as neutrinos. Charged leptons can combine with other protons and neutrons to form various composite particles such as atoms. Neutrinos rarely interact with anything and are consequently rarely observed. The best known of all charged leptons is the electron. Quarks and leptons are respectively classified in three "families" or "generations", and show completely different interactions and phenomenology. Quarks are subject to strong, as well as weak and electromagnetic interactions, leptons are not subject to strong interactions. Among the three lepton families, the first generation is the electronic leptons, comprising the electron and the electron neutrino, the second is the muonic leptons, comprising the muon and the muon neutrino, and the third is the tauonic leptons, comprising the tau and the tau neutrino. The electron is a stable particle, the muon and the tau are unstable. The muon decays to a muon neutrino, an electron and an electron anti-neutrino ($\mu^- \rightarrow e^- \bar{\nu}_e \nu_\mu$) with a branching fraction of approximately 100 %. In some rarer cases, in addition to these decay products, other particles with zero net charge may be produced (e.g. a photon, or an electronpositron pair). Searches for Charged Lepton Flavor Violating processes, such as the decay $\mu^- \rightarrow e^- \gamma$, have, so far, yielded null results. This is expected within the Standard Model which predicts a probability $< 10^{-50}$ for these phenomena (Fig. 1.1). With the current level of experimental precision, such effects are obviously well beyond our experimental reach. Although the Standard Model has been accurately tested, it is probably and incomplete theory. Several extensions of the model include Charged Lepton Flavor Violating (CLFV) processes and allow for the neutrino-less muon conversion to an electron, in the field of a nucleus with rates within the reach of the next generation experiments, including Mu2e.

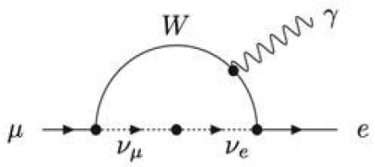

Fig. 1.1: Feynman diagram for the Charged Lepton Flavor Violating muon decay $\mu \rightarrow e\gamma$.

Mu2e has been designed and is now being constructed at Fermi National Accelerator Laboratory to search for the neutrino-less muon conversion to an electron in the field of an aluminum nucleus (Fig. 1.2). The beginning of Mu2e data taking is planned for the year 2021. The experimental signature of this process is a single mono-energetic electron with the energy of approximately the muon rest mass, 104.97 MeV. The simulation shows the Mu2e sensitivity allows to observe this process if it has a probability above 10^{-17}. In case no event is observed the limit on the probability of this process can be set at 10^{-17} which is an improvement of four orders of magnitude over current experimental limits.

Fig. 1.2: Feynman diagrams for the coherent muon conversion to electron in the field of a nucleus, according to Standard Model extensions which include Charged Lepton Flavor Violating processes.

1.1 The Fermilab accelerator complex

Fermilab is located about 50 km west of Chicago, Illinois. It is a US Department of Energy Laboratory and has been operated by the Universities Research Association (URA) since its founding, in 1967 [3]. Since 2007 it is operated by the Fermilab Research Alliance (FRA) a partnership of the University of Chicago and the University Research Association. The name Fermilab was given to the laboratory in 1974 in honor of the Nobel Prize-winning italian physicist Enrico Fermi [4]. Fig. 1.3 shows an aerial view of the laboratory, which has played a major role in the field of high energy physics for the last forty years. Among its scientific achievements, we can mention the discovery of three of the four particles of the third generation of the Standard Model: the bottom quark (May-June 1977), the top quark (February 1995) and the tau neutrino (July 2000) [3].

Fig. 1.3: Aerial view of the Fermi National Accelerator Laboratory. The 3.2 km circumference Main Injector tunnel is visible in the foreground, the Tevatron tunnel is visible in the background. The Mu2e facility is located next to the High Rise. The Tevatron has been the most "powerful" particle accelerator for many years before the turning on of the Large Hadron Collider (LHC) at CERN in Geneva.

1.1.1 The chain of accelerators

The Fermilab accelerator complex is made of several stages. The first stage is a Cockcroft-Walton generator, which turns hydrogen gas into H-ions by flowing it into a container lined with molybdenum electrodes: a matchboxsized, oval-shaped cathode and a surrounding anode, separated by 1 mm and held in place by glass ceramic insulators. A magnetron is used to generate a plasma to form H^- ions near the metal surface. A 750 keV electrostatic field is applied by the Cockcroft-Walton generator, and the ions are accelerated out of the container. The second stage is a Linear Accelerator (or Linac), which accelerates particles to 400 MeV, or about 70% of the speed of light. Right before entering the next accelerator, the H-ions pass through a carbon foil, which strips off the electrons thus producing a H^+ ions (i.e. protons) beam. The third stage is the Booster ring. The Booster ring is a 468 m circumference circular accelerator that uses magnets to bend beams of protons in a circular path. The protons coming from the Linac travel around the Booster about 20,000 times in 33 ms so that they repeatedly experience electric fields. With each revolution the protons pick up more energy, and leave the Booster with the energy of 8 GeV. Protons are injected into the Recycler Ring where they circulate while they are re-bounded by a 2.5 MHz frequency system. The reformatted bunches are transported to the delivery ring where they are slow extracted to the Mu2e detector through a new external beamline Fig. 1.4.

1.2 The Mu2e experimental apparatus

The Mu2e apparatus has been extensively documented in the Conceptual Design Report and Technical Design Report [6],[7]. The layout of the muon beam line and the detector system are based on the MECO design and are sketched in Fig. 1.5. The major feature of

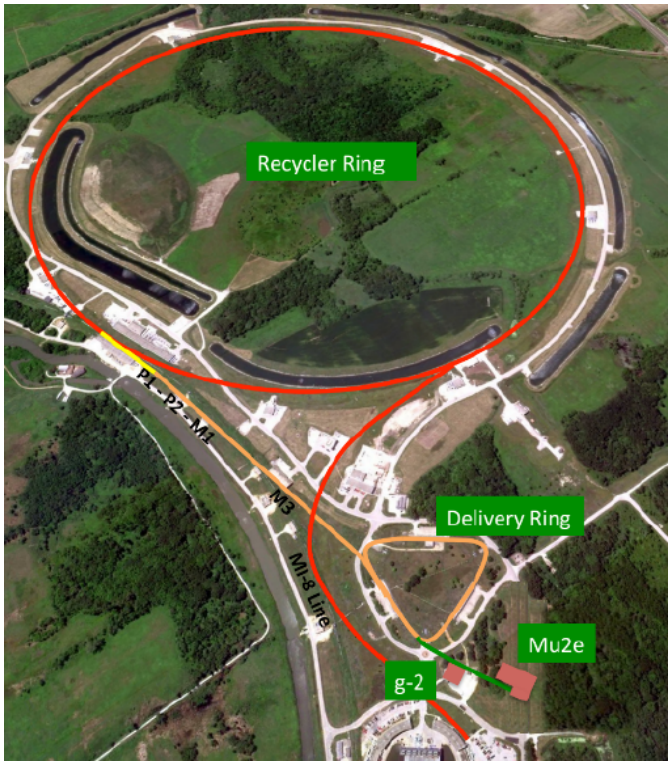

Fig. 1.4: Layout of the Mu2e facility (lower right) relative to the accelerator complex that provides the proton beam to the detector. Protons are transported from the Booster through the MI-8 beamline to the Recycler Ring where they circulate while they are re-bunched by a 2.5 MHz RF system. The reformatted bunches are kicked into the P1 line and transported to the Delivery Ring where they are slow extracted to the Mu2e detector through a new external beamline [5].

the muon beam line is the Superconducting Solenoid Magnet System. The inner bore of the solenoids is evacuated to 10^{-4} Torr in order to limit any background from muons that interact with gas particles. The Solenoid Magnet System can be schematically divided in 3 major sub-systems:

- Production Solenoid (PS);
- Transport Solenoid (TS);
- Detector Solenoid (DS).

We will give a brief description of the three elements of the Solenoid Magnet System in the next sub-sections.

1.2.1 Production Solenoid

The primary 8 GeV proton beam enters the Production Solenoid and strikes the production target located in an axial magnetic field which decreases from 5 T to 2.5 T along the beam line. The target is a radiatively cooled tungsten target, 16 cm long and 12.6 mm in

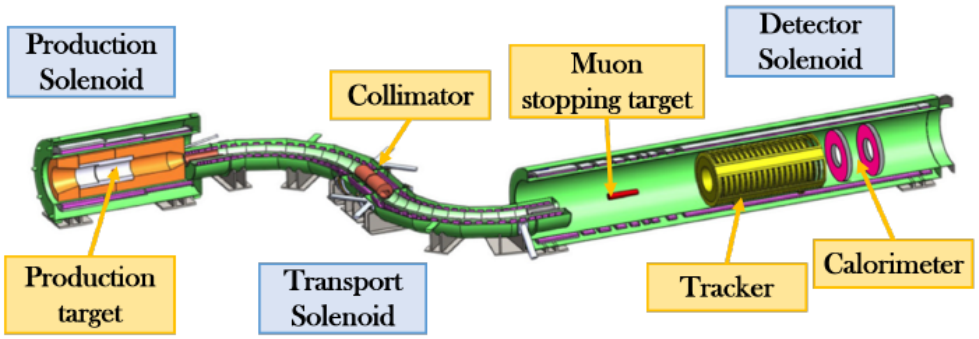

Fig. 1.5: The Mu2e apparatus. The proton beam enters from the right at the junction between the Production Solenoid and the Transport Solenoid and strikes the production target. The cosmic ray veto system, which surrounds the Detector Solenoid, and the muon stopping monitor are not shown in this scheme.

diameter. A massive concrete shield surrounding the Production Solenoid absorbs secondaries from the production target. Backscattered muons are captured by the Production Solenoid and transported through the S-bend Transport Solenoid to the stopping target.

1.2.2 Transport Solenoid

The function of the Transport Solenoid is to transport 10^{11} muons per second to be stopped in the secondary target located in the Detector Solenoid. This beam line includes the collimators and anti-proton stopping window in the Transport Solenoid, proton and neutron absorbers, beam stop, and vacuum system. The Transport Solenoid filters the particle flux producing a momentum (< 0.08 GeV/c) and charge-selected muon beam, with a good reduction of the contamination from $e^{\pm}$; μ^{+}; $\pi^{\pm}$; p and $\bar{p}$ during the detector live-time.

1.2.3 Detector Solenoid

The upstream section of the Detector Solenoid contains the muon stopping target and has a graded magnetic field, which nearly doubles the acceptance for conversion electrons and rejects certain backgrounds. The baseline aluminum target is made of $17 \times 0,02$ cm thick disks (Fig. 1.6). The disks are positioned parallel to each other and at the relative distance of 50 mm. The disks are centered on the Solenoid Magnet axis with each face perpendicular to it. Their radii range from 8.30 cm at the upstream end to 6.53 cm at the downstream end. The target support wires are made as thin as possible to minimize the probability that muons may interact and stop . If muons stop in the wires at a significant distance from the solenoid axis, then low energy electrons produced in the muon decay could fall into the acceptance of the tracker and cause an undesired low energy background.The downstream section of the Detector Solenoid is occupied by the tracker

and the electromagnetic calorimeter. This region has a relatively uniform magnetic field. Conversion electrons, produced in the stopping target are captured by the magnetic field within the Detector Solenoid. Then, they are transported through the tracker, which provides a precision measurement of the momentum. The conversion electrons hit the electromagnetic calorimeter, which performs an independent measurement of the electron energy and time of impact.

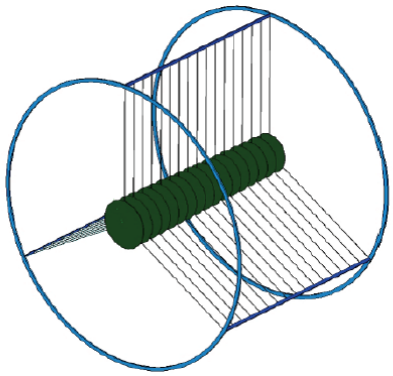

Fig. 1.6: The Mu2e stopping target. It is made of 17 aluminum disks, 0.2 mm thick, spaced 5.0 cm apart along the Detector Solenoid axis. The disks radii decrease from 8.3 cm at the upstream end to 6.53 cm at the downstream end.

1.2.4 Mu2e Detectors

The Mu2e tracker and electromagnetic calorimeter are placed inside the volume of the Detector Solenoid. The Mu2e collaboration has decided to use a tracker design similar to the one developed by the MECO collaboration (Fig. 1.7). The tracker resides in a uniform 1 T solenoidal magnetic field and is kept in a 10^{-4} Torr vacuum to reduce the interaction of particles with gas to a negligible level. This detector reconstructs particle tracks with high efficiency and measures the parameters of the helical trajectories with high resolution. Since multiple scattering in the tracker determines the resolution on the measurement of the helix parameters, the mechanical structure of the detector has to be extremely light. A further source of uncertainty is due to pattern recognition errors. This effect may produce high energy tails in the resolution function. The tracker is made of straw drift tubes and is called T-tracker because the straws are transverse to the axis of the Detector Solenoid. The basic detector element is made of a 20 μm sense wire inside a straw tube filled with gas. The straws are 5 mm diameter tubes made of 15 μm thick metallized Mylar. The tracker has $\sim$ 20000 straws arranged into 18 measurement stations across the $\sim$ 3 m tracker length. Planes consist of two layers of straws, to improve efficiency and help overcome the classic "left-right" ambiguity. A 1 mm gap between straws allows for manufacturing tolerance and expansion due to gas pressure. A ring at large radius, outside the active detector region, supports the straws. Each straw

has one preamplifier and one time to digital converter on both sides, to measure the signal arrival time on both sides, and uses also analog to digital converters for the measurement of the total integrated charge which provides useful information for particle identification. The tracker is designed so that only electrons with energy greater than approximately 53 MeV can be observed. They are approximately only 3% of the total flux of electrons from muon decays-in-orbit. Since momentum resolution is crucial to suppress several critical backgrounds, the tracker is required to have a momentum resolution better than 180 keV. The Mu2e calorimeter provides additional energy, position, and timing information for particles that have been reconstructed by the tracker. The calorimeter and the tracker use different physical processes and technologies to perform their measurements, so the sources of error from the two systems are not correlated. This helps to reduce backgrounds and gives a cross check to verify the quality of signal events. The calorimeter operates in the same solenoidal 1 T magnetic field and 10^{-4} Torr vacuum as the tracker. It handles a large flux of particles, mostly low energy background of protons, neutrons and gamma rays produced by muon captures in the stopping target. It also handles a large flux of electrons from muons decaying in the atomic orbit in the aluminum stopping target and other particles during beam injection. A more detailed description of the calorimeter is reported in Chapter **??**.

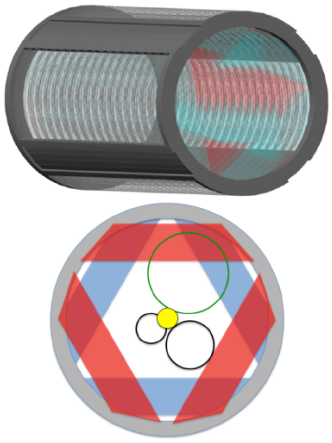

Fig. 1.7: Mu2e tracker layout. The top panel displays the 18 station tracking system. The bottom panel shows a cross-sectional view of the tracker. Only electrons with energies greater than 53 MeV are reconstructed. Electrons with lower energy spiral in the uninstrumented central region.

1.2.5 Trigger and Data Acquisition

The Mu2e detectors include the Trigger and Data Acquisition (TDAQ) subsystems, which provide hardware and software to record the digitized data from the detectors. These data are delivered to online and offline processors for further analysis. The TDAQ also synchronizes and controls the detector operations. In a streaming mode, the off-detector

bandwidth requirement for the DAQ is estimated to be approximately 100 GBytes/sec. The TDAQ combines information from all detector data sources and applies filters (triggers) to reduce this rate by a factor of several thousand before data can be delivered to offline storage.

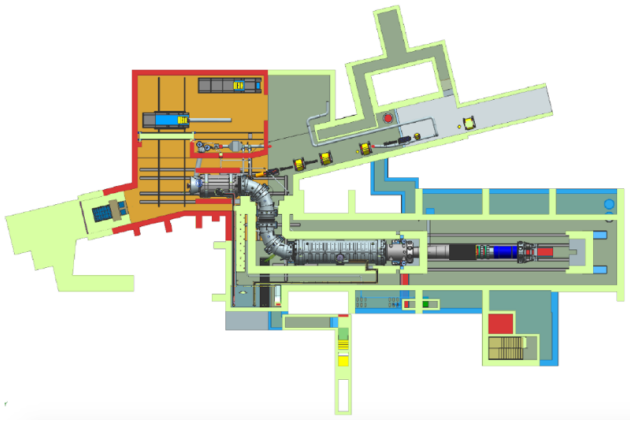

Fig. 1.8: Map view of the Mu2e experimental area.

Chapter 2

Calorimeter overview

The Mu2e detectors have been designed to reject backgrounds to a level consistent with a single event sensitivity for the $\mu \rightarrow e$ conversion of the order of 10^{-17}. The electromagnetic calorimeter is a vital link in the chain of background defenses. A background of particular concern is due to false tracks arising from pattern recognition errors that result from the high rate of hits in the tracker. Accidental hits may combine with hits from lower energy particles and erroneously create a trajectory consistent with a higher energy electron which may mimic the muon conversion signal. Thus the primary function of the Mu2e calorimeter is to provide a redundant set of measurements to complement the tracker information and provide sufficient information to reject backgrounds due to track reconstruction errors.

2.1 Conceptual detector design

Electrons produced in the decay of the muons stopped in the aluminum target follow helical trajectories in the solenoidal magnetic field and hit the front faces of the calorimeter crystals with a maximum energy in the 100 MeV range. In this energy regime a total absorption calorimeter employing a homogeneous continuous medium is required to meet the Mu2e energy and time resolution requirements. The sensitive material could be either a liquid, such as xenon, or a scintillating crystal. The Mu2e collaboration has chosen the scintillating crystal technology. Several types of crystals have been considered, including barium fluoride (BaF2) and cesium iodide (CsI). The baseline design uses an array of less expensive CsI crystals arranged in two annular disks. Fig. 2.1 shows a schematic view of the detector. Photodetectors, front-end electronics and services are mounted on the rear face of the disks and are not visible. Each crystal is read out by two large-area solid-state photo-detectors (SiPM) which are necessarily preferred to standard photomultipliers because the calorimeter operates in a 1 T magnetic field. While front-end electronics is mounted on the rear side of each disk, voltage distribution, slow control and data acquisition boards are hosted in 20 crates placed externally to the disks. A

laser flasher system provides light to each crystal for relative calibration and monitoring purposes. A circulating liquid radioactive source system provides absolute calibration and allows to determine the absolute energy scale. The crystals are supported by an aluminum structure which can be moved along the beam line on horizontal rails. The detector components are described in more detail in the following Sections.

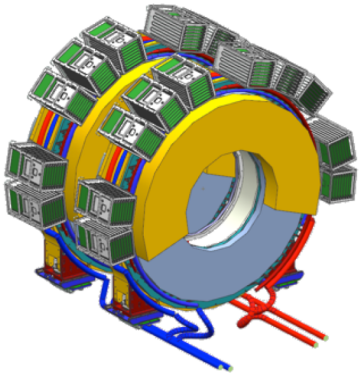

Fig. 2.1: CAD model of the Mu2e electromagnetic calorimeter. The two annular disks of crystals are visible; the 20 custom crates which host the boards for voltage distribution, slow controls and data acquisition are shown in grey and green; the calorimeter can be moved along the beamline on a horizontal rail.

2.2 Technical Specification

The primary function of the electromagnetic calorimeter is to measure electron energy, position and timing to confirm that particle trajectories reconstructed by the tracker are well measured and are not just the result of a spurious combination of hits. Moreover, the calorimeter provides information to the trigger for the online data selection of data. This leads to the following technical specifications [6]:

- Energy resolution of 5% at 100 MeV to confirm the electron momentum measurement performed by the tracker;
- timing resolution better than 0.5 ns to ensure that energy deposits in the calorimeter are in time with hits reconstructed in the tracker;
- position resolution better than 1 cm to allow a comparison of the position of the energy deposits to the extrapolated trajectories of the reconstructed tracks;
- the calorimeter should provide additional information useful for particle identification that can be combined with the information from the tracker to improve the muon/electron separation;

- the calorimeter should provide a trigger, either in hardware, or in software, or in firmware, that could be used to identify and select events with significant energy deposits;

- the calorimeter must operate in the hostile, high-rate, Mu2e environment and must maintain its functionality intact for radiation exposures up to 20 Gy/crystal/year and for a neutron flux equivalent to $10^{11} n_{1MeVeq}/cm^2$.

2.3 Calorimeter mechanics

The two calorimeter disks are placed inside the detector solenoid (Fig. 2.1). Each disk has an inner radius of 374 mm, an outer radius of 660 mm, and is made of 674 staggered trapezoidal crystals. The crystals are 200 mm long with a square base and a side length of 34 mm. Each crystal is wrapped with 8 layers of 25 μm thick HDPE (Tyvek) reflective film to maximize light transport within the crystal and minimize cross-talk among crystals [8]. The mechanical structure of each disk is made of two coaxial cylinders. The inner cylinder is made of carbon fiber in order to minimize the amount of passive material in the region where spiraling electrons are mostly concentrated. The outer cylinder can be as robust as required to support the crystals load and is made of aluminum. Each disk has also two cover plates. The plate facing the beam is made of low radiation length material to minimize the electron energy deposit in order to preserve the electron energy measurement (Fig. 2.2a). It has been designed to accommodate also the calibration source. The back plate supports the photosensors, the front-end electronics, the cooling pipes and is made of plastic material. It has been designed to allow easy access to the front-end electronics and crystals [9]. The electronic boards which provide the power to the photo-sensors, perform digitization of the photo-sensors signals and transmit data to the global Mu2e DAQ (Fig. 2.2b). Each crate houses 9 sets of boards. In order to gain as much space as possible between the disks and allow for an easier access to the front-end electronics, we have chosen to place the crates on the external side of the disks. One crucial function of the mechanical structure is to incorporate also adequate cooling system for the photo-sensors readout electronics and the electronic boards used for data acquisition, power and monitoring. This is a critical function since the calorimeter operates in vacuum and the electronic power has to be dissipated primarily through thermal conduction. To this purpose the electronics is placed in thermal contact with structures where cooling pipes are routed. The calorimeter cooling system has its own cooling station, composed of a vacuum pump and chiller placed externally to the cryostat, designed by INFN engineers.

2.4 Calorimeter electronics

The entire calorimeter electronic system can be divided in two main subsystems, which can be ideally separated for the different functions and locations. The first subsystem is placed on the back side of the crystal disks. It contains the photo-sensors and the front-end electronics. The second subsystem is made of the electronic boards which perform the digitization of the analog signals received from the front-end electronics and provide power and monitoring to the front-end electronics. This subsystem is located on the radial external side of the calorimeter. The boards are placed in the data acquisition (DAQ) crates clearly visible in Fig. 2.2b. The cooling system of the front-end electronics and of the data acquisition, power and monitoring electronics are partially independent and have been designed independently.

2.4.1 Photo-sensors and front-end electronics

The interaction between the electron and the Csl crystal generates photons which diffuse through the crystal towards the photo-sensors. Every crystal has on its back side the photo-sensors which convert light into electrical signals. There are two photo-sensors per crystal electrically connected to one front-end board. The reason for having two photo-sensors per crystal is to provide a more robust measurement and to not lose data if one photo-sensor fails during data taking. The total resulting number of photo-sensors is 1348 per disk. The front-end electronics for the calorimeter readout consists of two discrete and independent chips (Amp-HV) placed on one unique front-end board electrically connected to the back of the photo-sensor pins (Fig. 2.3). The two chips provide both amplification and a local linear regulation to the photo-sensor bias voltage. Groups of 16 Amp-HV chips are controlled by one dedicated ARM controller placed on one interface board placed in the DAQ crate that distributes low voltage and high voltage reference values, and sets and reads back the locally regulated voltages. The Amp-HV is a multilayer double-sided discrete component board that performs out the two tasks of amplifying the signal and providing a locally regulated bias voltage, and significantly reduces the noise loop-area. The two functions are independently executed in a single chip layer, named the Amp and HV sides, respectively. The development of the Amp-HV board has been done by the INFN Laboratori Nazionali di Frascati (LNF) Electronic Design Department. The required characteristics of the preamplifier are:

- high amplification with low noise;
- fast signal rise and fall times for good time resolution and pileup rejection;
- low detection threshold at the MeV level;
- functional in a rate environment of 200 kHz/channel;

- low power consumption.

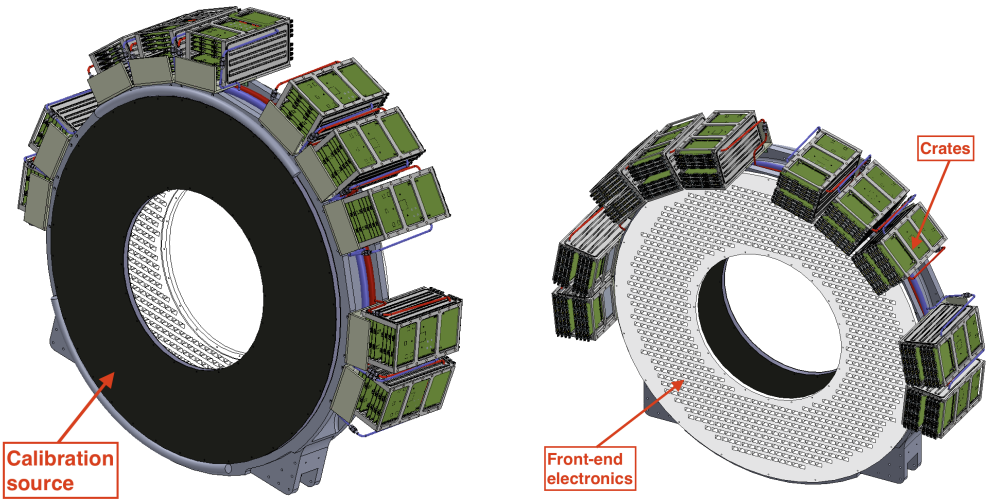

(a) Calorimeter plate facing the beam, made of low radiation length material.

(b) Back plate supporting the photosensors, the front-end electronics, the cooling pipes and made of plastic material.

Fig. 2.2: CAD model of one disk of the calorimeter. All the cables which connect the boards hosted in the crates to the front-end electronics are not shown.

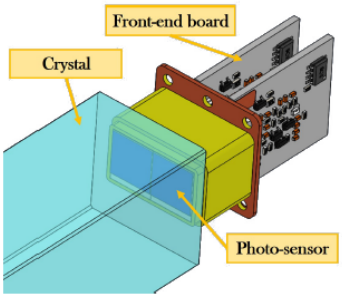

Fig. 2.3: CAD model of one crystal, photo-sensor and front-end board.

2.4.2 Data acquisition, power and monitoring electronics

The analog signals produced by the front-end electronics are transmitted to data acquisition boards hosted in the DAQ crates positioned on the radially external surface of the disks. Since the main function of the data acquisition boards is to digitize and transmit the analog signals to the global Mu2e data acquisition, these boards are named "waveform digitizers". Additional boards are necessary to provide and distribute power to the front-end boards, and to monitor the photo-sensor and front-end electronics performance. These boards are named "interface boards". There is an equal number of waveform digitizers and interface boards. Each DAQ crate hosts 8 waveform digitizers and 8 interface boards placed one next to the other. We will not describe in detail the functions of these

boards, we will only list the electronic components shown in Fig. 2.4 (only the ones of the digitizer, because the ones on the interface board have not been modelled yet).

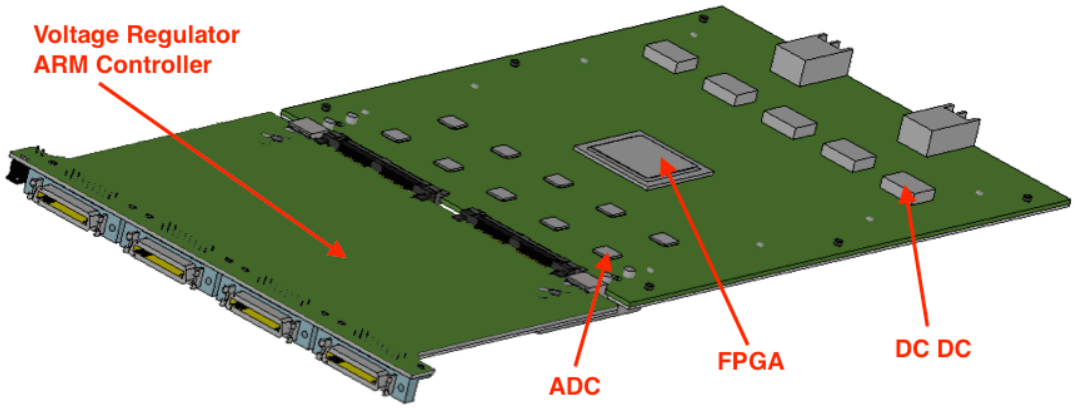

(a)

Fig. 2.4: Components on digitizer and mezzanine.

The waveform digitizer uses:

- 1 Field Programmable Gate Array (FPGA) We have chosen the FPGA FC1152 produced by the Company Microsemi. It is the most complex component of the board and it processes the data received from the photosensors and digitized by the Analog to Digital Converters (ADC). According to the data-sheet, the maximum junction temperature should be below 100°C. Since the exact amount of dissipated power depends on the number of operations the FPGA performs per unit of time, we have taken a conservative upper limit of the power dissipation at 4 W. This estimate will be verified once the firmware has been completed and implemented on the device.

- 5 DC-DC converters. The function of the DC-DC converter is to transform the voltage received from the external power supply to the values required by the components used on the board. We have chosen a nonstandard DC-DC converter with no iron-magnetic nucleus LTM8033 of Linear Technology. This has been a necessary choice, since the calorimeter is placed in a 1 T magnetic field, which would immediately saturate the field inside the iron nucleus of a standard DC-DC converter. Due to the absence of the iron-magnetic nucleus, this converter has a much lower efficiency than a standard device. This requires a larger power dissipation compared to a device equipped with iron-magnetic nucleus. The estimate of the dissipated power by 1 DC-DC converter is 3 W according to the data-sheet. The critical junction temperature is 125°C;

- 10 Analog to Digital Converter (ADC). The ADC converts analog signals received from the front-end boards into digital signals which are further processed by the

FPGA and then transmitted to the DAQ system. We have chosen the AD9230 of Analog Device with a relative power consumption of 470 mW per unit. The critical junction temperature is 150 °C.

We have verified that the resistors and capacitors power dissipation is negligible. The total power dissipated by one waveform digitizer board is $24\,W$. We currently have only a conceptual design of the interface board and the choice of the components has not been finalized yet. With the current design the interface board uses:

- One voltage regulator which transforms the 28 V received from the power supplies placed outside the cryostat to the 8 V used by the front-end electronics board. We expect the voltage regulator to provide a current of approximately 1 A. A conservative estimate of the dissipated power is 10 W.
- One ARM Controller and I2C drivers which monitor the performance of the front-end electronics. We estimate a dissipated power of approximately 0.2 W.

The total power dissipated by one interface board is approximately 10.2 W. The total power dissipated by one complete set of boards (digitizer plus interface board) is approximately 34.2 W. With the conservative assumption that also the clock distribution board dissipates the same power, the total power dissipated by each DAQ is of 310 W. In Table 2.1 reported a summary of the power dissipated by the electronic components.

Component name	**Component number**	**Component power [W]**
FPGA	1	4
DC-DC converter	5	3
ADC	10	0.5
Voltage regulator	1	10
RM controller	1	0.2

Table 2.1: Summary of the power dissipated by the electronic components used on one waveform digitizer and one interface board.

2.5 Calorimeter cooling

Since the calorimeter operates in vacuum, a dedicated cooling system has been designed to exctract the dissipated electronic power. A cooling station external to the cryostat which hosts the Mu2e detectors provides a cooling fluid flow sufficient to keep the temperature of the electronic components below the critical temperature of operation above which the rate of failures increases significantly. The cooling circuits of the front-end and DAQ

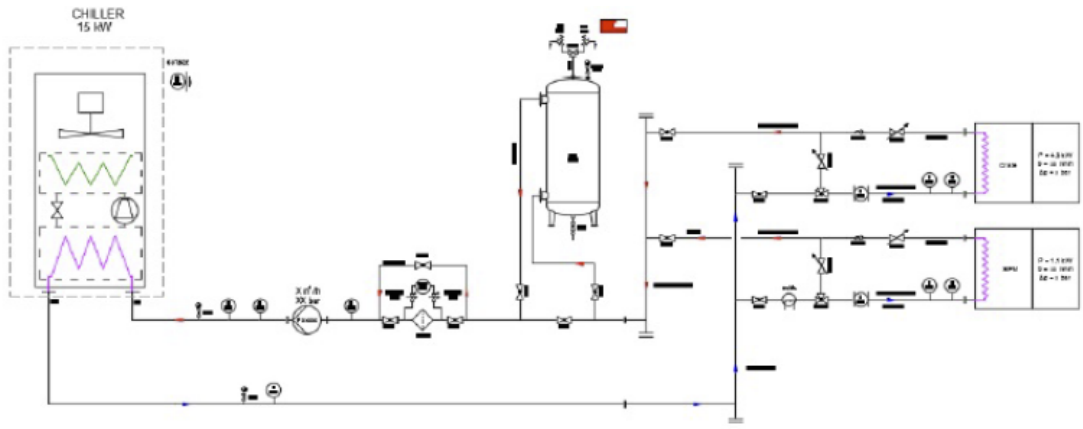

Fig. 2.5: Conceptual design of the calorimeter cooling circuit and station.

electronics and their manifolds are independent, but are connected to the same cooling station outside the cryostat (Fig. 2.5).

The front-end electronics cooling system is integrated in the back-plane made of plastic material (Fig. 2.6). The photo-sensors and front-end electronic boards, assembled in one compact structure, are inserted in the precision holes machined in the back plate. This configuration allows easy access to the electronics and crystals in case maintenance is required. The cooling lines run along the rows of holes. Fig. 2.6 shows the network of cooling lines positioned on the back plate.

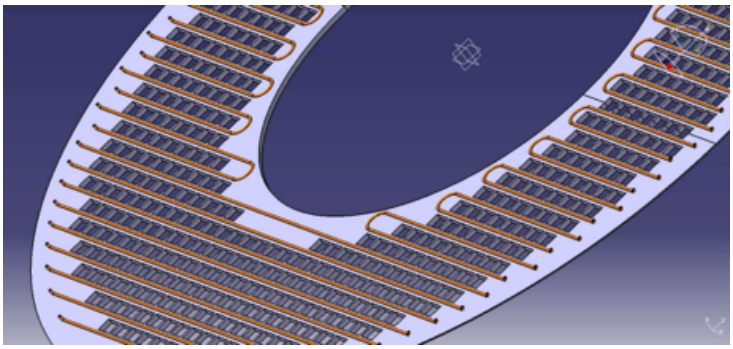

Fig. 2.6: Schematic view of the cooling pipes network as positioned on the back plate.

Fig. 2.7 shows a complete view of the calorimeter back plate with 38 cooling lines: 18 are straight while the other 20 have one 180° curve. The lines are copper pipes with inner diameter $d = 3\,mm$ and outer diameter $D = 4\,mm$, brazed to a properly shaped profile, also made of copper, which allows the connection to the SiPM (Fig. 2.8). Table 2.2 reports the lengths of all cooling lines. Fig. 2.9 shows the connections of the copper pipes to the manifold.

The front-end and the DAQ electronics cooling systems use the same coolant: 35% monopropylene glycol aqueous solution, whose properties are reported in Table 3.1, opertating approximately at $-10\,°C$. The average velocity of the coolant in the front-end cooling system is $3.5\,m/s$ and provides a Reynolds number approximately of 2500 and a

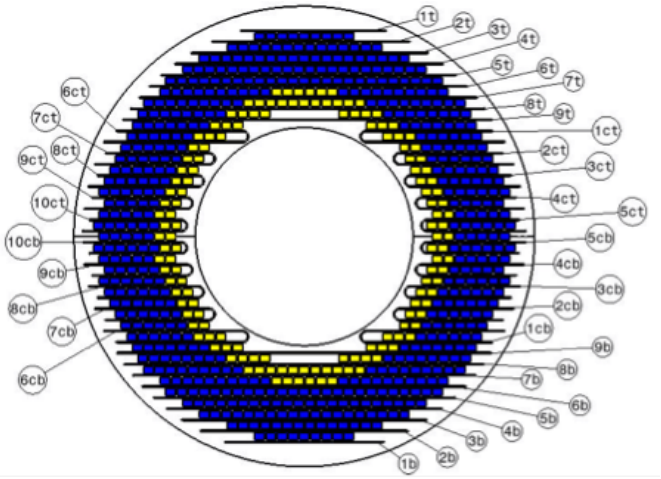

Fig. 2.7: View of the cooling pipes on the back plate with their conventional numbering.

Pipe	Length [mm]
1b 1t	511
2b, 27	658
3b, 3t	771
4b, 4t	863
5b, 5t	941
6b, 6t	1009
7b, 7t	1068
8b, 8t	1120
9b, 9t	1165
1cb, 6cb, 1ct, 6ct	905
2cb, 7cb, 2ct, 7ct	760
3cb, 8cb, 3ct, 8ct	734
4cb, 9cb, 4ct, 9ct	694
5cb, 10cb, 5ct, 10ct	673

Table 2.2: Length of the pipes numbered in Fig.2.7.

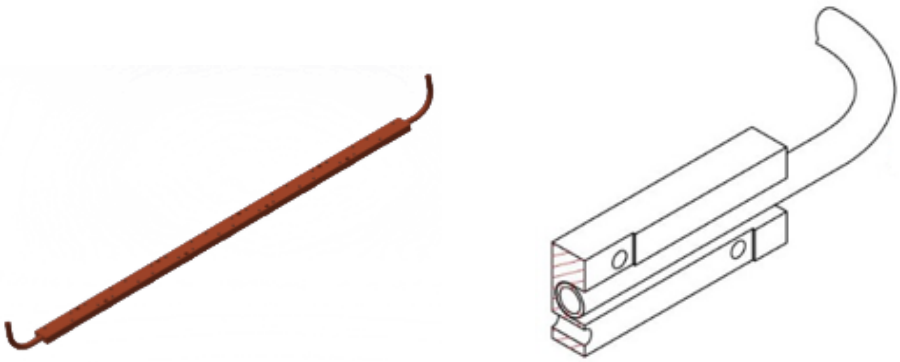

(a) Schematic view. **(b)** Technical drawing.

Fig. 2.8: Copper cooling pipe with brazed shaped profile.

film coefficient approximately of $5100\,W/(m^2K)$. With these values the coolant temperature rises of approximately $0.5\,°C$ along line 7b (Fig. 2.7), which is the line that dissipates the largest power. The total front-end colant flow rate is approximately $1.14\,kg/s$ estimated with the Hardy-Cross method. The front-end unit (Fig. 2.10) is connected to the cooling circuit thanks to four screws, which allows a proper heat exchange in order to keep the temperature of the SiPM at $0\,°C$. The proper design of the copper electronics holder has been made by Federico Mosti [10] in order to fullfil the temperature requirements on the SiPM (Fig. 2.11).

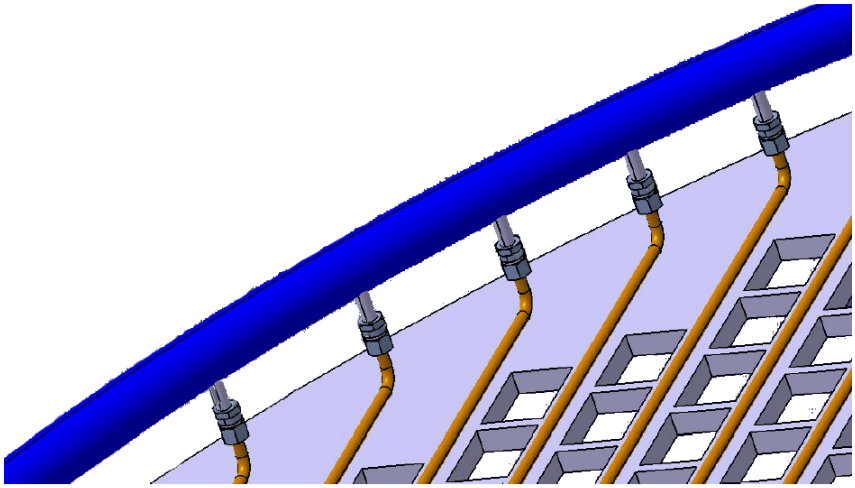

Fig. 2.9: Particular of the connection between pipes and the manifold on the front-end plate.

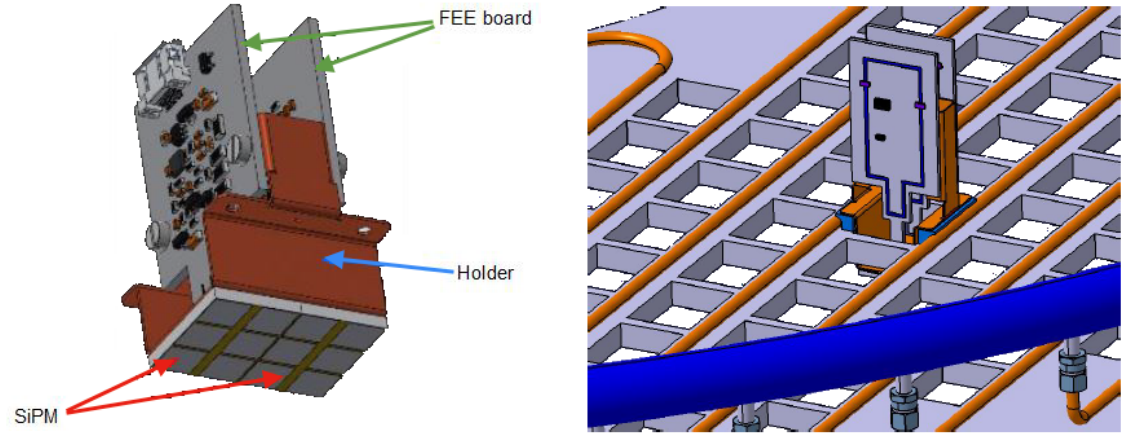

(a) Schematic CAD model of the front-end unit. The two SiPMs are glued on the lower side of the copper support and electrically connected to the two front-end boards which are mechanically connected to the support with two screws.

(b) Schematic CAD view of the front-end plate with the piping system and one front-end unit inserted in the corresponding hole.

Fig. 2.10: Schematic CAD views of the front-end electronics and cooling system

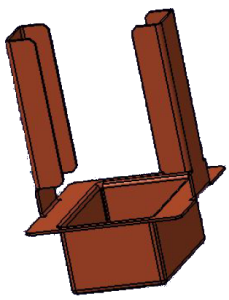

Fig. 2.11: Schematic CAD model of the copper deep-drawn SiPM case.

The DAQ boards cooling system is integrated in the DAQ crates (Fig. 2.2) and has to

keep the temperature of the electronic componens below the critical value. Two supply and two return manifolds (one for each disk of the calorimeter) connect the cooling system of each crate to the chiller. The connection pipes between the crates and the manifolds are one of the critical parts of the project beacuse they have to be easy accessible for the assembly. The DAQ electronics cooling system is the research project I have developed for my Master Thesis. The idea has been to integrate a cooling circuit in the crate walls and extract the power dissipated by the electronic boards with a cooling fluid flux (Fig. 2.12). Its design will be widely described in the following chapters.

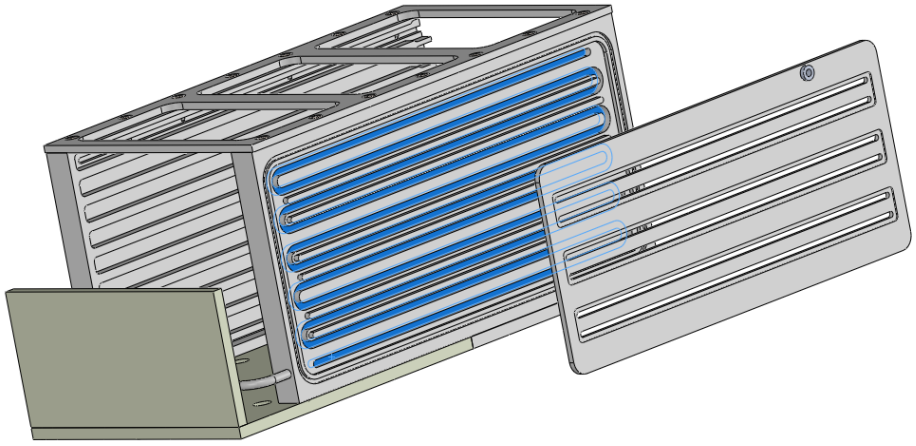

Fig. 2.12: Exploded CAD view of the DAQ crate. The cooling circuiti machined in each lateral wall of the crates is shown in blue in the figure.

Chapter 3

Mechanical and hydraulic design of the DAQ cooling system

The electromagnetic calorimeter cooling system is composed of two main sub-systems running in parallel. One is dedicated to the front-end electronics, one to the DAQ boards and crates. In this Chapter we will describe the hydraulic design of the part of the cooling system dedicated to the DAQ boards which has been the topic of my Master Thesis. Taking into consideration the constraints deriving from the experimental conditions and the required physics performance, I have chosen the cooling fluid and estimated the necessary mass flow rate to keep the electronic components at an acceptable temperature of operation. I have entirely designed the DAQ crate geometry and studied all the involved manufacturing problems. All the adopted solutions will be described. I have also performed a detailed estimate of the pressure losses along all the cooling circuit elements, which is necessary to size the pumps. The design of the entire cooling circuit has not been entirely finalized yet and some parts parts of the system are still at a conceptual level.

3.1 Design constraints

We had to develop a project acceptable to the groups responsible of the integration of the tracker and calorimeter in the Mu2e experimental area. We had thus to verify that all the calorimeter services would fit in the limited space available inside the cryostat. The most stringent constraints were the available space (Fig. 3.1) and the operational conditions of the cooling fluid. The refrigerating system is located inside the cryostat and has to leave sufficient space to the other services, including cables and vacuum pumping. The main function of the cooling system is to keep the temperature of all the electronic components below the critical values since temperatures above these thresholds would cause irreversible damage and reduce the reliability and the expected lifetime of the components. For all the electronic components placed inside the cryostat, at the vacuum level of $10^{-4}\,torr$,

all the dissipated power has to be removed by conduction through a cooling fluid. In all the calculations heat transfer due to thermal irradiation has been neglected with respect to forced convection. This approximation is justified by comparing the temperatures and sizes of the radiating surfaces to the estimated power transferred by conduction through the cooling system.

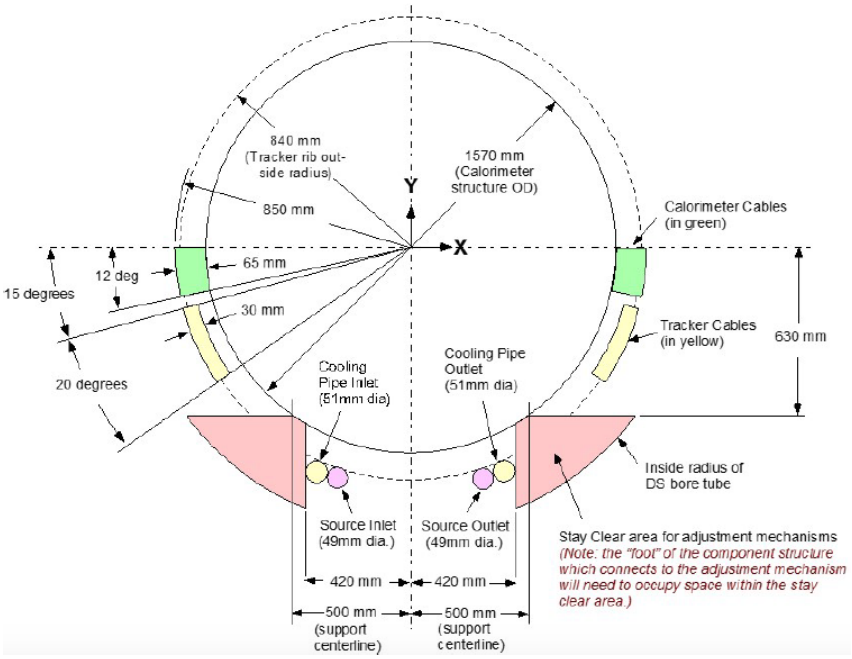

Fig. 3.1: Schematic transverse view of the calorimeter geometry including the volumes reserved to the electric cables and cooling pipes.

3.2 Choice of the cooling fluid

We have performed a detailed study of the properties of several commercially available refrigerant fluids. We have taken into account the following parameters:

- cost;
- corrosion properties;
- required pumping power;
- thermal properties.

We have chosen a 35% monopropylene glycol aqueous solution, which has excellent thermal properties (Table 3.1) and a limited cost.

Property	Value
Density $\rho \left[\frac{kg}{m^3}\right]$	1040
Specific heat $c_p \left[\frac{J}{kgK}\right]$	3759
Dynamic viscosity $\mu [Pa \cdot s]$	$4.331 \cdot 10^{-3}$
Thermal conducivity $k \left[\frac{W}{mK}\right]$	0.429
Freezing point $T_{freezing} [^\circ C]$	-17

Table 3.1: Thermal properties of a 35% monopropylene glycol aqueous solution.

3.3 Design of the DAQ crate

This section describes the mechanical and hydraulic design of the DAQ crate and the lateral walls which host the cooling circuit (Fig. 3.2). We have first estimated the required flow rate of the cooling fluid and the resulting transverse size of the cooling pipe.

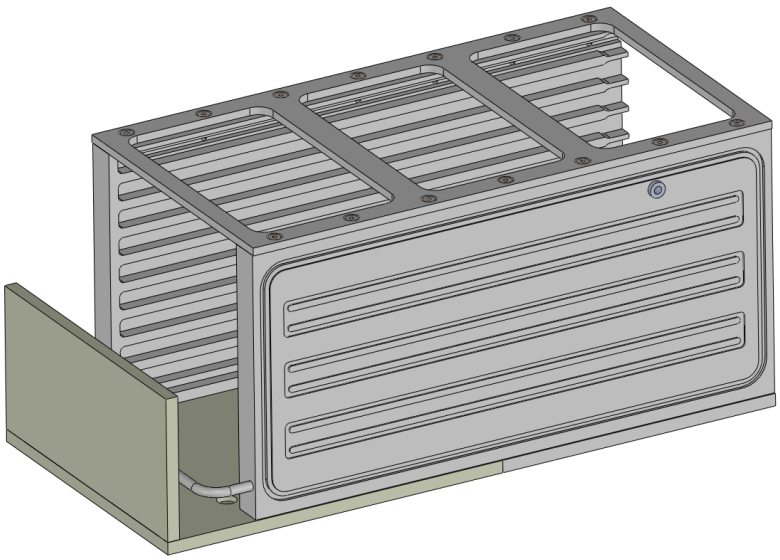

Fig. 3.2: CAD model of the designed DAQ crate.

3.3.1 Mass flow rate and cooling pipe transverse section

Extracting the dissipated power from the crate with a cooling fluid is an example of forced convection problem in pipes. The required mass flow rate and the internal diameter of the pipe are the unknown variables of the problem. We have used an iterative approach, in order to optimize pipe dimensions and pressure losses. If $\dot{m}$ is the mass flow rate and ΔT the temperature difference between the fluid output from the crate and the fluid input to the crate, the following equation provides the correlation with the amount of power we want to extract from the crate:

$$W_{TOT} = \dot{m} c_p \Delta T \tag{3.3.1}$$

In order to determine the necessary flow rate, the standard procedure is to fix the thermal drop between the output and input cooling fluid at a desired value. We have chosen to fix the upper limit of the thermal drop ΔT at $2\,°C$ so that the properties of the fluid can be considered approximately constant along the circuit and approximately equal to the data reported in Table 3.1. After an iterative process we have chosen a temperature rise $\Delta T \approx 1\,°C$ between the output and the input to the entire circuit relative to one DAQ crate, which corresponds to temperature rise of approximately $0.5\,°C$ on each of the two lateral walls of the crate. For the total power of 310 W dissipated in one crate and $\Delta T = 0.5°C$, the resulting required mass flow rate is:

$$\dot{m} = \frac{W_{TOT}}{c_p \Delta T} \approx 0.08\,\frac{kg}{s} \tag{3.3.2}$$

Once we have determined the mass flow rate, we have chosen the pipe shape and determined the size, with the specific goal to keep the average velocity v_f of the fluid under control, since the pressure losses have a quadratic dependence on v_f, and to have the increase the Reynolds number at a level of 3000, that allows to have a fully developed turbulent flow and consequently a larger convective heat exchange coefficient. We have decided to keep the average velocity of the fluid below $v_f \leqslant 3.5\,m/s$. Several space and technological problems, better explained in section 3.3.2, suggested to choose a square section. The hydraulic diameter D_H of a pipe with square section is given by the following equation:

$$D_H = \frac{4A}{p} = L_{sq} \tag{3.3.3}$$

where A and p are respectively the area and the perimeter of the square section of the pipe and L_{sq} the length of the square section edge.

The average velocity v_f of the fluid and the Reynolds number are respectively:

$$v_f = \frac{\dot{m}}{\rho A_{section}} \tag{3.3.4}$$

$$Re = \frac{\rho v_f D_H}{\mu} \tag{3.3.5}$$

Fig. 3.3 shows the graph relative to Equation 3.3.4, with $A_{section} = D_H^2$ since in our case the pipe section is a square. The green area shows that the condition $v_f \leqslant 3.5\,m/s$ is satisfied for $D_H > 4.75\,mm$ Fig.3.4 shows the graph relative to Equation 3.3.5. The green area shows that the condition $Re > 3000$ is reached for $D_H < 6.3\,mm$

We have chosen $L_{sq} = D_H = 5\,mm$ which gives: $v_f \approx 3.15\,m/s$ and $Re \approx 3800$.

The resulting Prandtl number is:

$$Pr = \frac{\mu c_p}{k} \approx 38$$

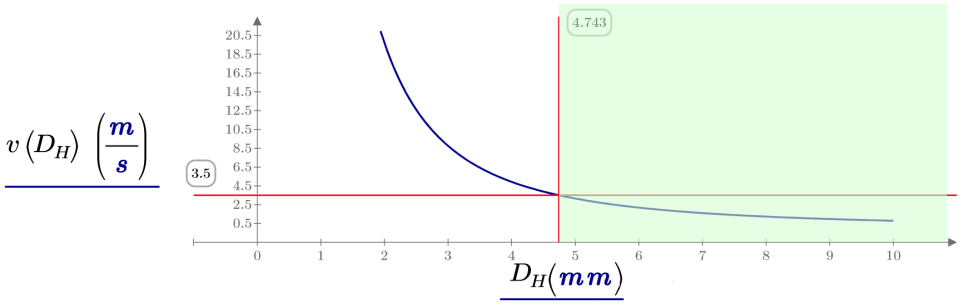

Fig. 3.3: Graph $D_H - v(D_H)$, D_H is determined from Equation 3.3.3 and $v(D_H)$ is the fluid velocity in the pipe determined from Equation 3.3.4.

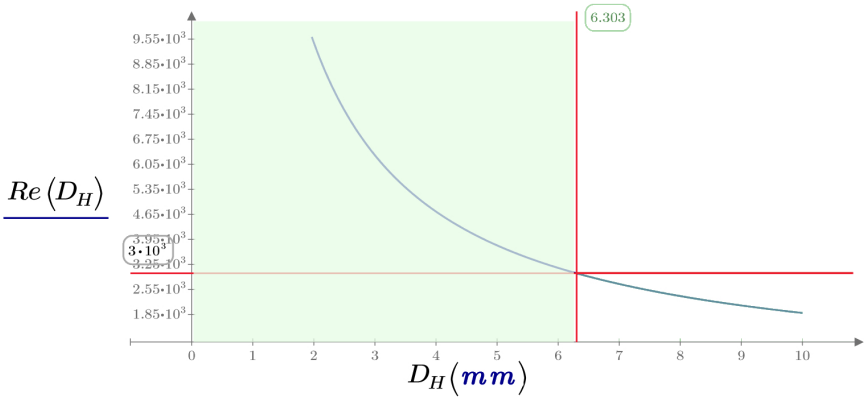

Fig. 3.4: Graph $D_H - Re(D_H)$, D_H is determined from Equation 3.3.3 and $Re(D_H)$ is the fluid velocity in the pipe determined from Equation 3.3.5.

Using the Dittus-Bolter equation for a turbolent flow we have obtained the Nusselt number:

$$Nu = 0.023 Re^{0.8} Pr^{0.3} \approx 50$$

and the convective heat transfer coefficient:

$$h = \frac{Nu\,k}{D_H} \approx 4.3 \cdot 10^3 \frac{W}{m^2 K} \tag{3.3.6}$$

The h coefficient obtained and the effective heat transfer area allow the acceptable temeprature gradient between the cooling fluid and the walls of the square cooling pipe, like shown in Section 3.3.3.

3.3.2 Design of the DAQ crate walls

The design of the DAQ crate walls where the cooling fluid flows needs to find a compromise between two opposite requirements:

- minimize the temperature gradient between the fluid and the aluminum crate wall;
- minimize the pressure losses along the cooling circuit.

Once the section and the velocity of the fluid have been fixed, the only parameter still to be determined is the heat exchange area between the fluid and the aluminum crate wall, which is proportional to the length of the cooling circuit and also depends on the pressure loss of the fluid along the circuit. We have designed the crate walls in order to maximize the heat exchange area and we have verified that the pressure loss due to the chosen geometry is compatible with the performance of the pumping system. We already had a preliminary design of the DAQ crate which used a cooling copper pipe brazed to the crate wall [9]. We have abandoned this solution not only for the larger required thickness of the wall, but also because more accurate studies have shown that the power dissipated by electronics is larger than previously estimated. In fact, in order to increase the heat exchange, we have to enhance the contact area between the fluid and the crate, to make a cooling circuit with a smaller step. Unfortunately it is not possible to curve the copper pipe of the original preliminary design with such a small inner radius of the bend (minimum bend radius usually $\approx 2 \times d_{in\,pipe}$). We have developed a new crate design which implements a cooling circuit based on a cooling circuit directly milled in the aluminum wall and closed on the top with a shaped cover. A simplified view of the CAD model is shown in Fig. 3.5 while Fig. 3.6 shows the wall and the crate machined by VCS S.r.l. The details and dimensions are available in Appendix **??**.

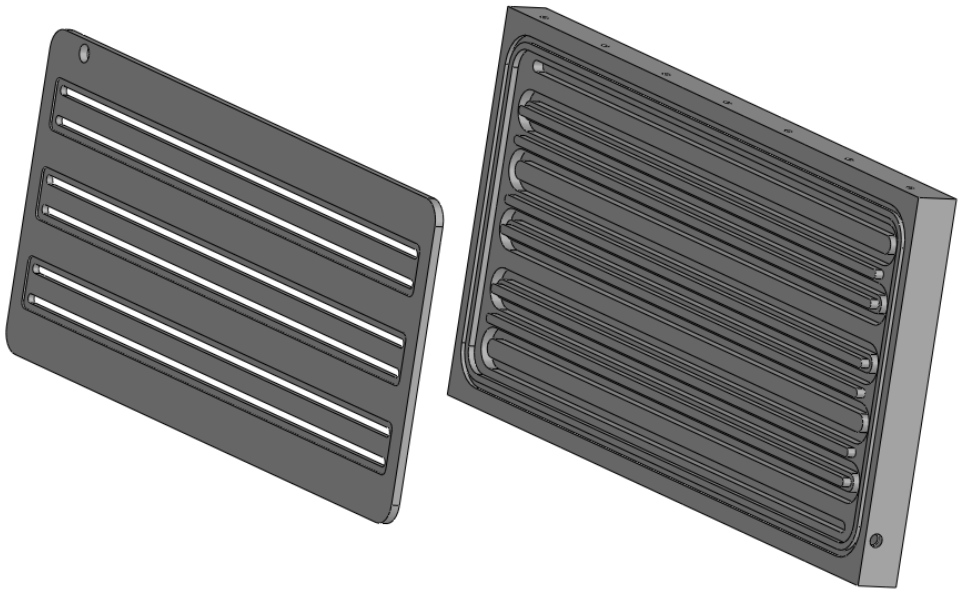

Fig. 3.5: Schematic representation of the DAQ crate aluminum walls with the cooling circuit directly milled in the volume of the wall.

We have added six extrusions (Fig. 3.8a) which match the grooves made on the cover (Fig. 3.8b), in order to increase the stiffness of the structure and to reduce the possible deformation of the cover due to any internal pressure of the cooling fluid. Fig. 3.7b shows the estimated deformations of the only cover, loaded with a pressure of 2 MPa (conservative assumption) in the area approximately occupied by the cooling circuit (Fig. 3.7b)

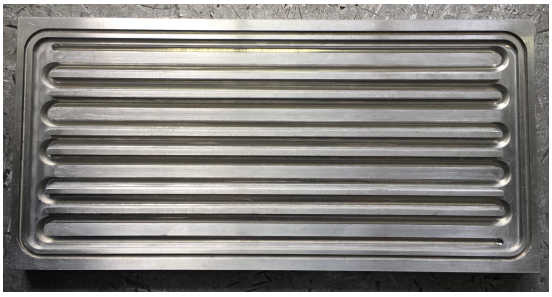

(a) Wall with the milled cooling circuit.

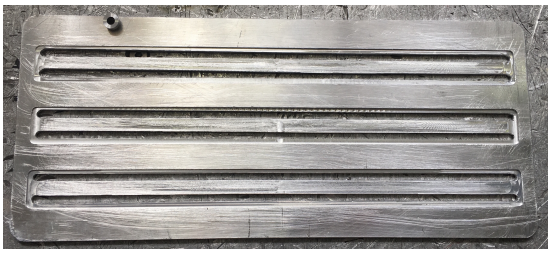

(b) Cover of the crate wall with the input/output nozzle not welded yet.

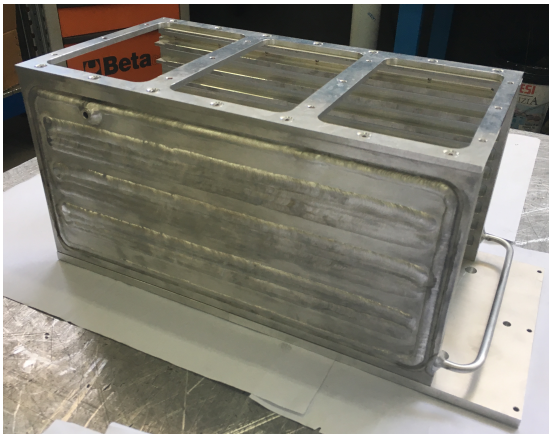

(c) Assembled DAQ crate: side view showing the weldings which connects the laterla wall with the cover.

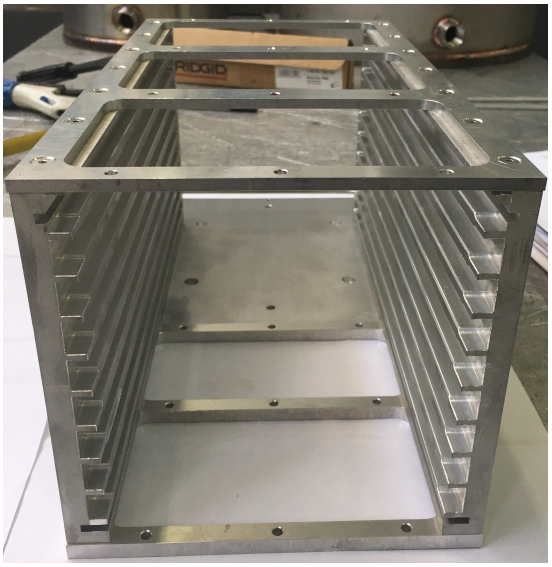

(d) Assembled DAQ crate: frontal view showing the grooves for the boards.

Fig. 3.6: DAQ crate prototype assembled at VCS S.r.l.

and constrained with a fixed support in coincidence of the positions edges of the perimeter and the grooves.

The cover and wall will be welded by TIG welding technology (Tungsten Inert Gas) along the perimeter and all around the edges of all the extrusions.

This design has been developed in collaboration with the VCS S.r.l. personnel responsible of the crate fabrication. In one of our meetings we have been suggested to add the groove around the matching edges of the perimeter of the wall and the cover (Fig. 3.9). This allows to reduce the stiffness of the wall in the region close to the welding and to mitigate the risk of welding stress. In fact, after the welding, which heats the metal, the aluminum of the cover and the wall shrink as a consequence of the temperature drop. Unless we put the groove on the perimeter, the tensions would be very large and they would probably cause a crack of the welded connection, which is the weakest one. Fig. 3.10 shows the step added between the cover and the wall, to allow the welder to make an angular welding instead of a top one. We have also been suggested to implement a similar

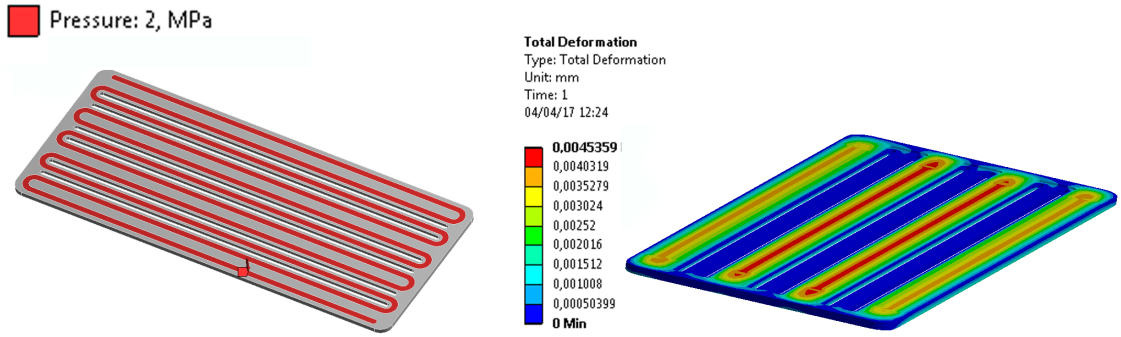

(a) Pressure of 2 MPa (20 bar) applied on the red area, which is the one in contact with the fluid. A fixed constraint has been inserted on each edge of the inner face of the cover.

(b) Total deformation of the cover under the pressure of the cooling fluid.

Fig. 3.7: FEM simulation of the deformation of each cover of the crate. The areas marked with red show the maximum values of the deformation.

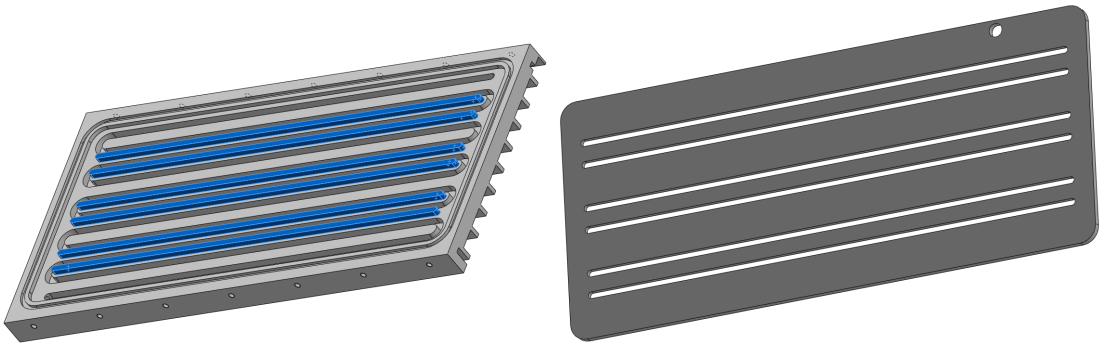

(a) Extrusions.

(b) Grooves.

Fig. 3.8: Matching extrusions and grooves between the wall and the cover of the crate.

solution for each extrusion, so that the connection between the two parts can be made again by angular weldings (Fig. 3.10).

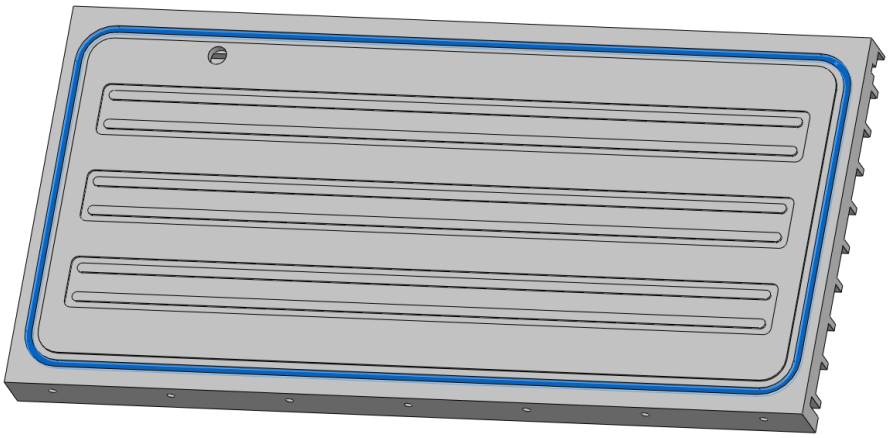

Fig. 3.9: Groove around the perimeter made to allow a higher compliance of the region close to the perimeter of the wall and to reduce the tension near the welded zone.

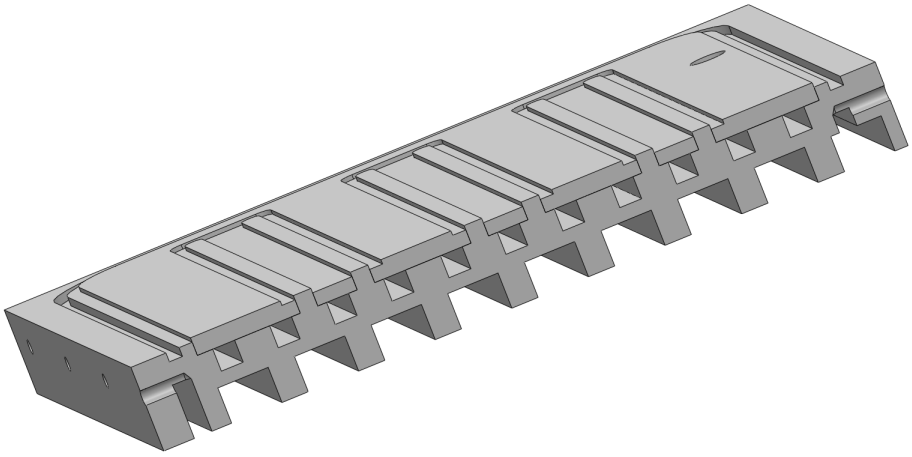

Fig. 3.10: The section view shows the lower thickness of the cover with respect to the height of the teeth. This allows to have the presence of the step clearly shown, whereby it is possible an angular welding. In this figure also the perimetral groove is shown again.

The openings for the connections between the two manifolds (supply and return) and the connection between the two walls of each crate are critical. In both cases the available space is very limited and it is not possible to use thread fittings. Fig. 3.11a shows the solution designed for the first connection. A bushing of aluminum (the same of the cover and the crate) is welded to the cover. With reference to the detailed section of Fig. 3.11b, the part is welded all around the perimeter on the inner edge **1**, while there are only few points of welding on the outer edge **2**. This is done because the first welding guarantees that the cooling fluid does not exit from the circuit, the second is made to increase the stiffness of the connection, but only in few points to reduce the interference with the welding on the perimeter between the cover and the wall. The design and choice of the pipes that link the manifold to each crate will be discussed in the following section 3.4.

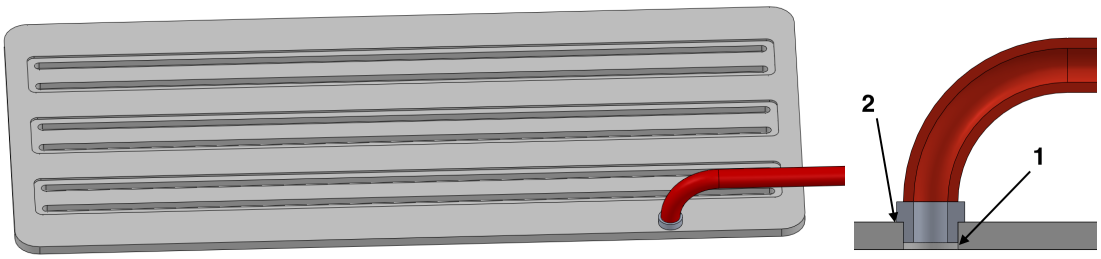

(a) Overview. **(b)** Detail.

Fig. 3.11: Connection between the crate and the manifold: the step between the nozzle bottom and the bottom face of the cover allows the angular welding which seal the fluid in the circuit.

For the connection between the two walls we have chosen a curved aluminum pipe, partially embedded in the crate and TIG welded around its perimeter (Fig. 3.12). The welding of this pipe can be done only after linking and fixing the two walls with the top and bottom layer.

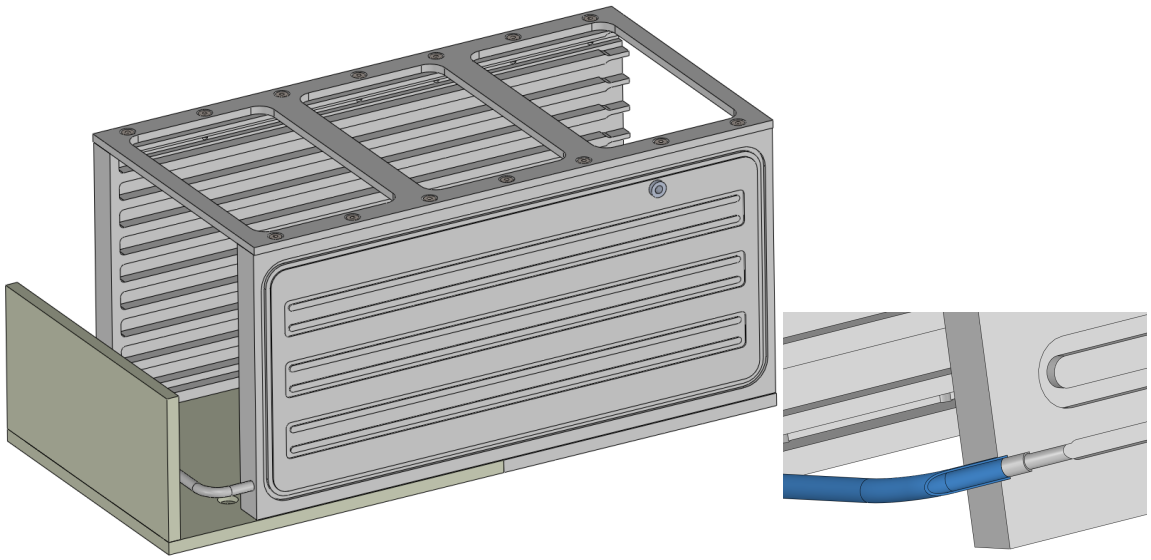

(a) (b)

Fig. 3.12: Connection between the two walls: the curved pipe partially enters inside the holes of the two crate walls which allows a better centering operation and also an easier and safer welding.

The technical drawings of each part of the crate are reported in Appendix **??**.

3.3.3 Estimate of average thermal resistance of the cooling circuit in crate wall

We have used the geometrical dimensions of the cooling channel shown in Fig. 3.5 to estimate the area of contact between the cooling fluid and the crate wall. We have estimated $A \approx 17520\,mm^2$ in the conservative assumption to have thermal transfer only through the side of the channel parallel to the crate wall (Fig. 3.13).

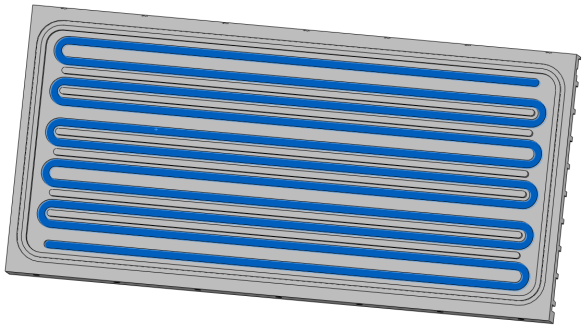

Fig. 3.13: Schematic representation of the heat transfer area estimated as the surface of the cooling channel milled in the crate wall parallel to the crate wall.

We have determined the resistance R_{th} using the heat transfer area A and the heat

transfer coefficient h as determined from Equation 3.3.6:

$$R_{th} = \frac{1}{Ah} \tag{3.3.7}$$

The resulting temperature gradient ΔT has been determined assuming that the total power $W_{TOT} = 310\,W$ is equally distributed and exctracted through the two symmetrical crate walls

$$\Delta T_{convection} = R_{th}\frac{W_{TOT}}{2} \approx 2\,K \tag{3.3.8}$$

ΔT is the thermal drop between the average temperature of the cooling fluid along the circuit ($-9.5\,°C$) and the average temperature of the crate wall.

3.4 Supply and return manifolds design

Using the flow rate of each crate estimated with Equation 3.3.2 the average velocity of the fluid in the manifold is given by the following equation:

$$v_{manifold}(D_{manifold}) = n_{crates}\frac{G}{\rho\left(\frac{\pi D_{manifold}^2}{4}\right)}$$

with:

- $D_{manifold}$: inner diameter of the manifold;
- n_{crates}: number of crates in one calorimeter disk;
- ρ: cooling fluid density (Table 3.1);
- G: mass flow rate in one crate.

Fig. 3.14 shows the dependence of the fluid velocity in the manifold on the manifold inner diameter.

Since we want the average velocity of the cooling fluid inside the manifold below $2\,m/s$ we have chosen $D_{manifold} = 25\,mm$ and we have obtained $v_{manifold} \approx 1.6\,m/s$. We have designed the manifold as a curved pipe with this inner diameter and the outer diameter $D_{out} = 28\,mm$. The radius of the medium circumference is $695\,mm$. The smaller pipes which connect the manifold to each crate are welded radially with an angular offset of $16\,°$, as shown in Fig. 3.15.

Fig. 3.16 shows the solution that we have adopted to connect the manifolds to the crates. Because of the limited volume available between two consecutive crates, we have moved the connections, made with VCR bimetallic fittings by ATLAS, closer to the tracker. This requires longer pipes and consequently produces larger pressure losses but

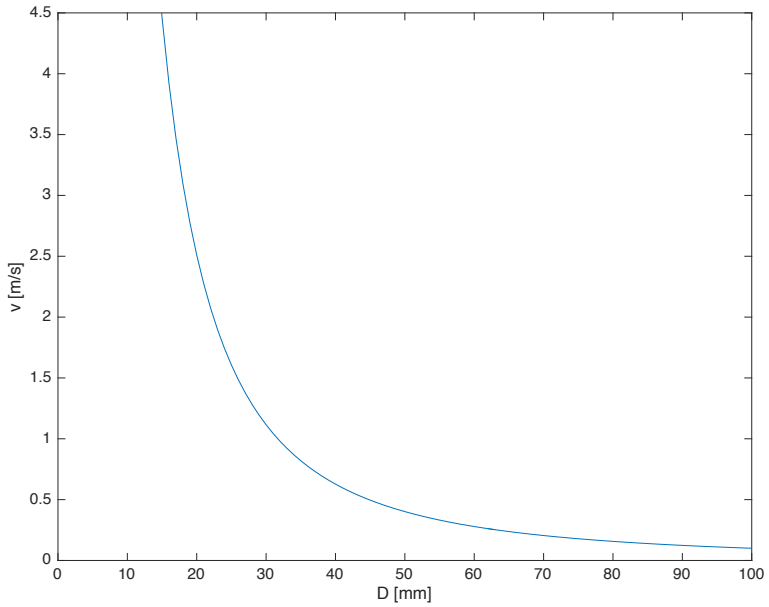

Fig. 3.14: Graph of the average velocity of the cooling fluid in the manifold as a function of the inner manifold diameter.

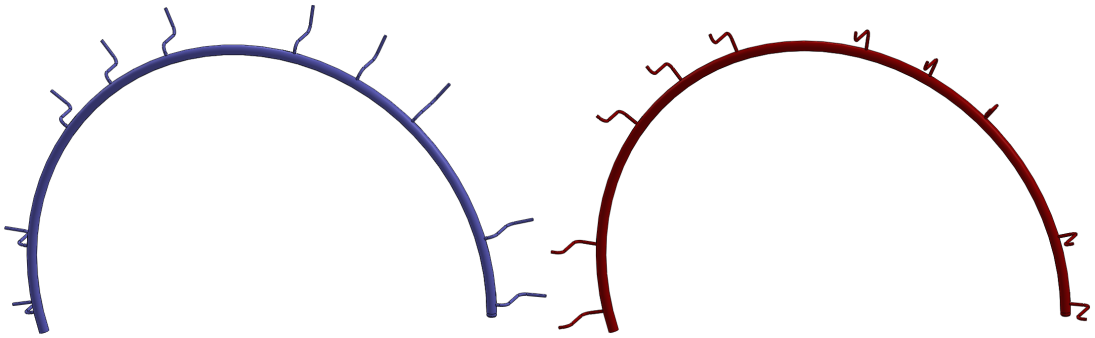

(a) Supply manifold. **(b)** Return manifold.

Fig. 3.15: Manifolds design: the S-shaped pipes which connect the manifold to the crates are welded to the main curved pipes previously drilled. The main body of both manifolds is the same, while the connecting pipes are different between the supply and the return.

on the other hand it allows an easier way to lock the connection for the operator who has got more space. A longer and curved pipe allows also a larger compliance of the connection and so an easier mounting operation, with lower risks of weldings stress. Appendix **??** reports the drawings of the supply and return manifolds while Appendix **??** reports the data of the VCR fittings by ATLAS.

3.5 Estimate of the pressure losses

We have estimated the pressure losses along the manifold and each crate; we will verify that the pressure losses are compatible with the pumping station already available at Fermilab or we will determine the prevalence required to buy the proper pump. These

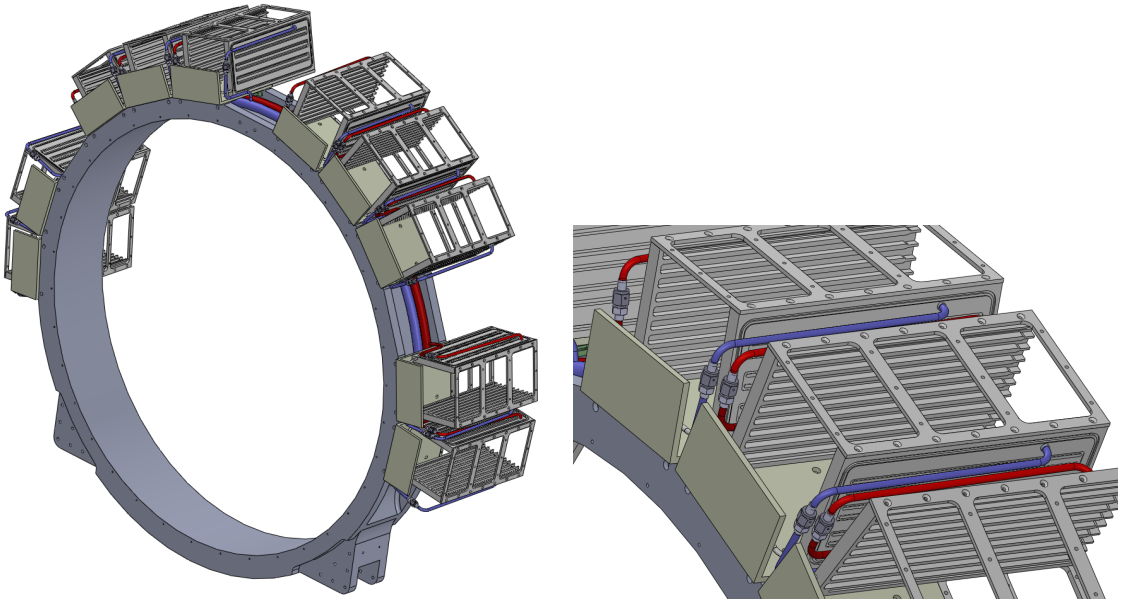

(a) Overview. **(b)** Detailed view.

Fig. 3.16: Connection between the manifolds and the crates; we have chosen a position of the VCR fitting which requires longer pipes and produces a larger pressure loss but allows an easier mounting to the operator.

estimates are preliminary and will be validated with experimental tests. However they are important to understand if the design is reasonable before building a mockup of the circuit.

3.5.1 Estimate of the friction coefficient

The equation which allows to estimate the pressure loss ΔP along a rectilinear pipe is:

$$\Delta P = f \frac{\rho L v^2}{2 D_H} \tag{3.5.1}$$

where f is the friction coefficient and depends on the roughness ε of the internal surface of the pipe and on its diameter and L is the total length of the straight pipe. In literature many relations and graphs relative the friction factor can be found; we have determined the friction coefficient through the Haaland equation 3.5.2, which is the only explicit and consequently the easiest equation to use. Assuming a roughness $\varepsilon = 1.6\,\mu m$ of the internal surface of the pipes and milled circuit:

$$f_{Haaland} = \left[-0.782 ln \left(\frac{6.9}{Re} + \left(\frac{\varepsilon}{3.7 D_H} \right)^{1.11} \right) \right]^{-2} = 0.04 \tag{3.5.2}$$

This is the value of the friction factor we have used to estimate the pressure losses reported in the following Sections.

3.5.2 Distributed pressure losses in the DAQ crate

There are 11 straight lines in each lateral wall of the crate, each one is $300\,mm$ long (Fig. 3.17).

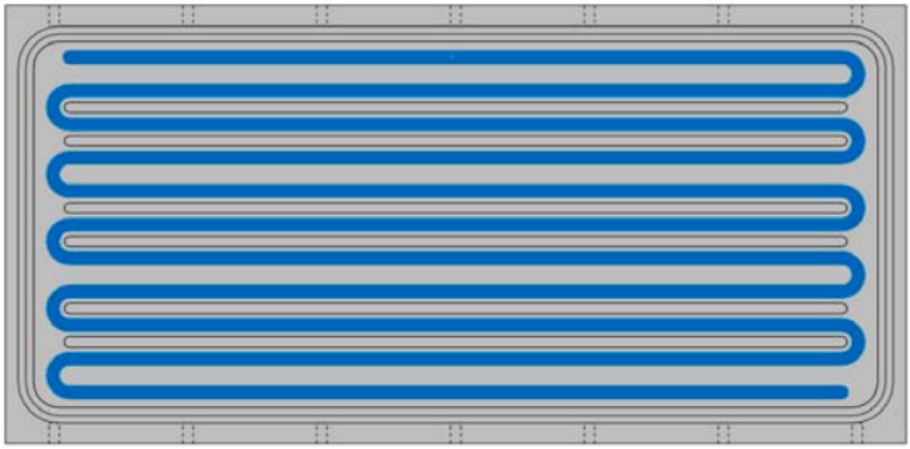

Fig. 3.17: Cooling circuit milled in the lateral wall of the crate.

Using equation 3.5.1 and the friction coefficient estimated in 3.5.2, we have estimated a total pressure loss of $\Delta P_{linear} = 1.4\,bar$.

3.5.3 Localized pressure losses in the DAQ crate

Pressure losses in the curves of the cooling circuit

For the pressure losses along the 10 curves that connect the eleven straight parts of the cooling circuit (Fig. 3.17) we have:

$$K_{bend} = 0.71 \qquad \text{and} \qquad \Delta P = n_{bends}\left[\frac{K_{bend}\rho v^2}{2}\right] = 0.38\,bar$$

The parameter K_{bend} has been determined as reported in Appendix **??** (please notice that in the Appendix ζ replaces K_{bend}, following the notation of the reference [17]).

Pressure losses in the changes of sections

Before the cooling fluid exits from the first lateral wall of the crate and enters the frontal pipes which connect to the entrance of the second wall, the cross section of the pipe changes: first a reduction with also a difference between the square shape of the milled circuit and the following round shape with inner diameter $d_{in} = 4\,mm$ and then a bigger round section of connection with the frontal aluminum pipe (Fig. 3.18a and Fig. 3.18b). Since we will use a connecting pipe with the inner diameter $d = 4\,mm$ the pressure loss in the opening is negligible.

Referring to Fig. 3.18 and using the coefficient $K_{reduction} = 0.4$ calculated in Appendix **??** we have estimated:

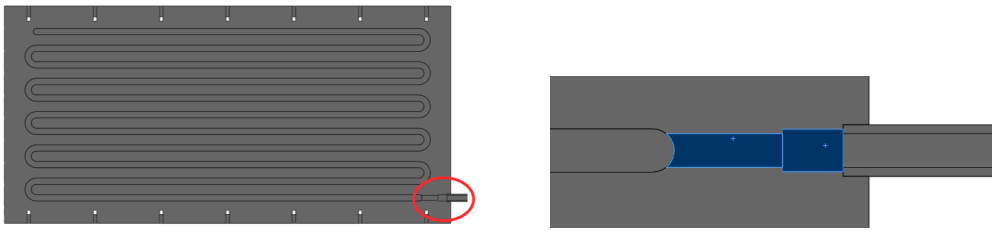

(a) Section reduction. **(b)** Section opening.

Fig. 3.18: Changes of section: this change of section is necessary to avoid a too small thickness of the wall of the crate in that position, because of the perimetral groove of Fig. 3.9.

$$\Delta P_{reduction} = K_{reduction} \frac{\rho v^2}{2} = 0.08\, bar$$

In the short part with $d = 4\, mm$ and length $L_1 \approx 22\, mm$ we have, given of the continuity of the flow rate:

$$v_{reduction} = \frac{G}{\rho \left(\frac{\pi d^2}{4}\right)} = 6.1\, \frac{m}{s}$$

Assuming the roughness equal to $1.6 \mu m$ and the the friction coefficient estimated with equation 3.5.2, the distributed pressure loss in that short part calculated with equation 3.5.1 is:

$$\Delta P = 0.04\, bar$$

Downstream the connecting pipe between the two walls, whose pressure losses will be reported in the following section, we have again a reduction and the opening but, using the same way used before, we can consider only the loss due to the opening. With $K_{expansion} = 0.25$ [17], it determines the following pressure loss:

$$\Delta P_{reduction} = 0.05\, bar$$

Pressure losses in the pipe connecting the two lateral walls of each crate

We have chosen to use a aluminum pipe (Fig. 3.19), welded to the two lateral walls in coincidence of the frontal holes, to allow the cooling fluid to pass from the circuit milled in the first wall to the second wall of each crate.

Using K_{90° from Appendix **??** and relation 3.5.1 we have:

$$\Delta P_{distributed} = 0.63\, bar \qquad \Delta P_{bends} = 0.11\, bar$$

These pressure losses are relative to a curved pipe with an inner diameter of $4\, mm$ and an outer diameter of $6\, mm$, which is the pipe we will use for the crate prototype tests.

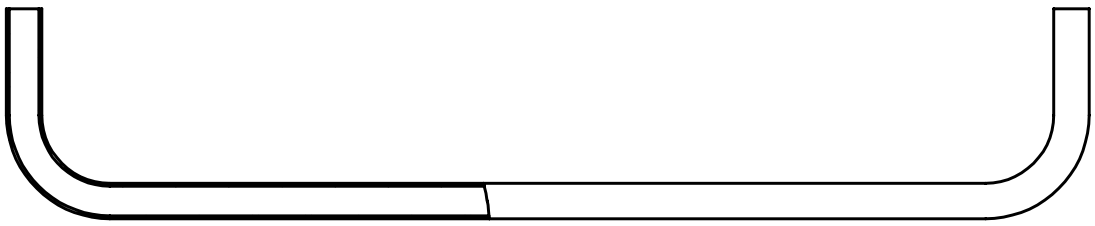

Fig. 3.19: Connection pipe between the two walls of the crate.

We can also take into account the solution of a pipe with an inner diameter of $5\,mm$, which has to be brazed instead of welded to the wall because of its small thickness. This solution would reduce the pressure losses in this part of the circuit:

$$\Delta P_{distributed} = 0.2\,bar \qquad \Delta P_{bends} = 0.04\,bar$$

Pressure loss in the input/output nozzle

Considering the input and the output nozzle as a 90° curve with a change, we have $K_{in/out} \approx 0.84$ [17] and:

$$\Delta P_{in/out} = K\frac{v^2\rho}{2} = 0,05\,bar$$

3.5.4 Manifolds and connections

Pressure loss in the manifold

Using the geometry of the manifold we have:

$$L_{manifold} = R_{manifold}\alpha_{manifold} \approx 2.41\,m$$

and assuming again the same roughness $\varepsilon = 1.6\mu m$, using 3.5.1 we have estimated the pressure loss:

$$\Delta P_{manifold} \approx 0.05\,bar$$

On both the manifolds we have 10 smaller connection pipes with the crates. Considering them as a "T" and using the coefficient K=0.5, we have estimated:

$$\Delta P_{Tmanifold} = 20\left(0.5\frac{\rho v^2_{manifold}}{2}\right) = 0.13\,bar$$

Pressure loss in the connection pipes between manifolds and crates

With reference to Fig. 3.20, the total length of the straight parts of the pipes are $L_{supply} = 0,412\,m$ and $L_{return} = 0,413\,m$. The curves have $R_0/D_H = 4$ (with R_0 middle radius of the curve and D_H the hydraulic diameter), an angle $\delta \approx 90°$, the coefficient is $K_{bend} = 0.5$

[17]. We have assumed a coefficient $K_{VCR} = 1$, since we have not chosen the VCR fittings yet. The connection with the manifold is T shaped (Fig. **??**). With $v_f = 2.7\,m/s$ (internal diameter of the connecting pipe $d_{in} = 6\,mm$) we have obtained:

$$\Delta P_{pipe} = \frac{\rho v_f^2}{2}\left(8K_{bend} + 2K_{VCR} + 1 + 1.5 + \frac{f_{Haaland}(L_{supply} + L_{return})}{d_{pipe}}\right) = 0.6\,bar$$

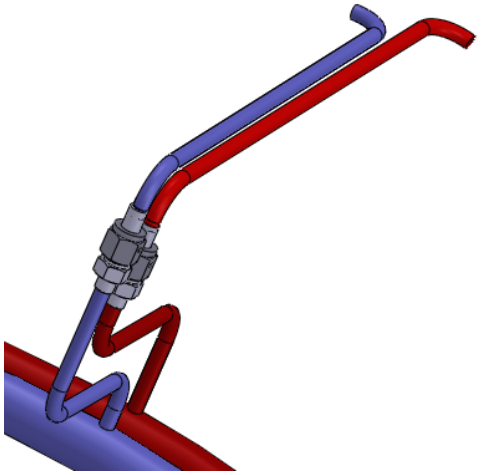

Fig. 3.20: Supply and return connection pipes.

3.5.5 Summary

Table 3.2 summarizes the pressure losses estimated for all the circuit elements of one crate.

Type of losses	**Value [bar]**
Distributed in wall	2.8
180° curves	0.76
Change of sections	0.21
90° curves	0.11
Distributed in connection pipes	0.63
Inning and outing nozzles	0.1
Total	**4.61**

Table 3.2: Overview of all the contributions to the pressure losses in the cooling circuit of one crate.

Table 3.3 summarizes the pressure losses in the supply and return manifold and the total losses in the 10 DAQ crates present in one calorimeter disk. The estimate of 5.3 *bar* is the total pressure loss in one calorimeter disk and the reference value necessary to size the pump.

Type of losses	**Value [bar]**
Distributed in both manifolds	0.1
Connecting pipes from manifold to crate	0.6
Crate	4.6
Total	**5.3**

Table 3.3: Summary of the contributions to the total pressure losses in one calorimeter disk.

Chapter 4

Thermal simulation of the DAQ boards and crate

In this Chapter we analyze the thermal simulation of the DAQ boards and crate and we estimate the temperatures of the electronic components placed on the boards. Since the components on the interface board have not been chosen yet, the thermal analysis will be limited to the waveform digitizer board performing FEM thermal simulation. We will first summarize the dimension and the thermal properties of the components used on the digitizer (some of this information have already been given in section 2.4.2). After the description of the waveform digitizer board we will describe the design of the inner part of the lateral walls of each crate, which is in mechanical and thermal contact with the boards, and we discuss the choice that we have made and showing, for the designed solution, the mounting sequence of each set of boards. After we report the models and the assumption that we have made to analyze the heat transfer problem, in order to perform an estimate of the maximum temperature reached on the top of the electronic components for the different solutions we have studied. In this chapter we will also discuss the problem of the thermal interface in vacuum, with a brief report of the equations and formulas used to model these interfaces.

4.1 Thermal properties of the waveform digitizer electronic components

In this Section we will report the mechanical and thermal properties of the electronic components used on the waveform digitizer with a special focus on the components which have the maximum power density.

Property	Value
T_{JMAX}	125°
θ_{JA}	$15.4°C/W$
$\theta_{JCbottom}$	$5.2°C/W$
θ_{JB}	$9.8°C/W$
θ_{JCtop}	$16.7°C/W$

Table 4.1: Thermal properties of the DC-DC converter LTM8033 LGA.

DC-DC converter

We have selected the DC-DC converter LTM8033 LGA (Fig. 4.1a); Fig. 4.1b shows the tolerance on the thickness of this component.

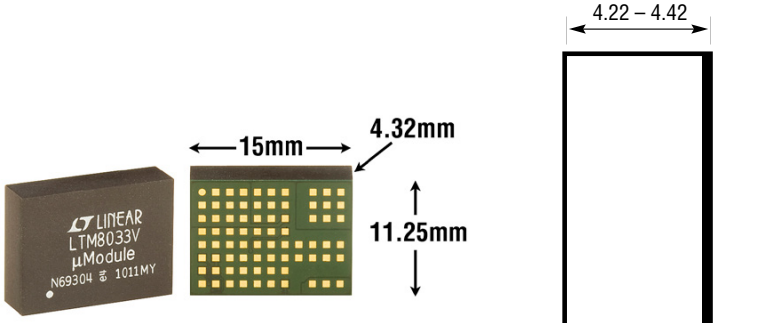

(a) Main dimensions. **(b)** Thickness tollerance.

Fig. 4.1: DC-DC converter LTM8033 LGA.

Table 4.1 reports the several contributions to the total thermal resistance of the DC-DC converter LTM8033:

- $\theta_{JCbottom}$ is the resistance between the junction and the bottom of the component;
- θ_{JCtop} is the resistance between the junction and the top of the package cover;
- θ_{JB} is the total resistance between the junction and the board, so it includes $\theta_{JCbottom}$ and the resistance between the bottom and the board, which is not given;
- θ_{JA} is the total resistance between the DCDC and the air

The graphical representation of thermal circuit internal to the DC-DC converter is shown in Fig. 4.2.

For more detailed information relative to the DC-DC converter see Appendix **??**. For the complete datasheet refer to [11]

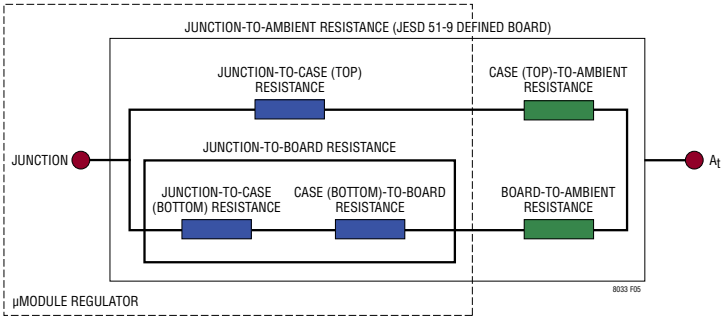

Fig. 4.2: Graphical representation of the thermal circuit associated to the DC-DC converter.

Microsemi FC1152 FPGA

Fig. 4.3 and Table 4.2 respectively report the design and the dimensions of the Microsemi FC1152 FPGA package. The data sheet reports that the thermal resitance θ_{jc} between the central juction and the case of the component is approximately $0.38\,°/W$.

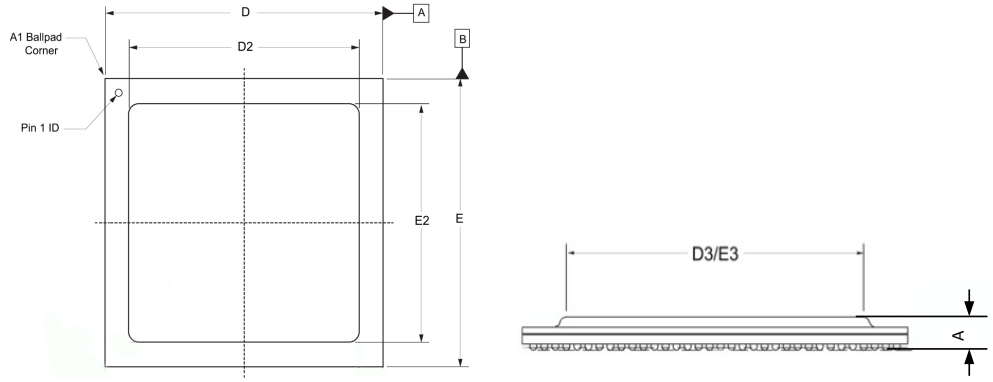

(a) Top view. **(b)** Side view.

Fig. 4.3: Mechanical drawings of the Microsemi FC1152 FPGA.

Dimension	Min. [mm]	Nom. [mm]	Max. [mm]
A	2.34	2.62	2.90
D	34.85	35.00	35.15
E	34.85	35.00	35.15

Table 4.2: Dimensions of the Microsemi FC1152 FPGA.

According to the data sheets the maximum temperature allowed at the junction of this component is approximately $100°C$. Conservatively we do not want the maximum temperature of the juction to exceed half of this value. The maximum expected power dissipated by the component is approximately $4W$. This implies that the maximum temperature allowed on the case of the FPGA T_{MAX} is:

$$T_{MAX} = \frac{T_{FPGA}^{max}}{2} - \Delta T = T_{FPGA}^{max} - W_{FPGA}\theta_{jc} = 48.5\,°C$$

in order to have $50\,°C$ at the juction. For more detailed information relative to the Microsemi FC1152 FPGA see Appendix **??**. For the complete datasheet refer to [12] and [13]

Analog to Digital Converter AD9230

We have chosen the ADC AD9230 (Fig. 4.4). The thermal properties are reported in Table 4.3.

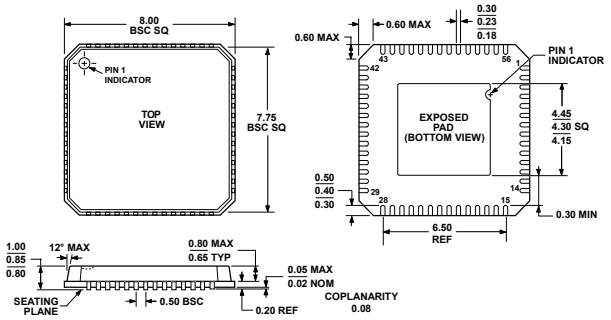

Fig. 4.4: AD9230 dimensions and mechanical tolerance.

Property	**Value**
Storage Temperature Range	$-65°$ to $+125°$
Operating Temperature Range	$-40°$ to $+85°$
Lead Temperature(Soldering 10 sec)	$300°$
Junction Temperature	$150°$
θ_{JA}	$30.4°C/W$
θ_{JC}	$2.9°C/W$

Table 4.3: AD9230 thermal properties.

Table 4.3 shows that the thermal resistance between the junction and the top of the cover of the package is $\theta_{JC} = 2.9°C/W$. Since the maximum juction temperature has to be below $75\,°C$, which is half of the maximum temperature reported in the datasheet, and the ADC maximum dissipated power is $W_{ADC} \approx 0.5W$, the maximum temperature allowed on the top of the component is:

$$T_{top}^{max} = \frac{T_J^{max}}{2} - \theta_{JA} W_{ADC} \approx 73°C$$

For more detailed information about the ADC see Appendix **??**. For the complete datasheet refer to [14].

4.1.1 The waveform digitizer printed circuit board

The electronic components mounted on the board are frequently cooled using a copper thick layer inside or at the bottom of the printed circuit board. This copper layer is

in thermal contact with the components placed on the upper face through thermal vias (Fig. 4.5). In some cases, the electronic components have also dedicated pins to heat dissipation soldered to this layer. At the sides of the board the thermal layer emerges and is placed in thermal contact with the board lockers which transfer the power to a dedicated cooling system.

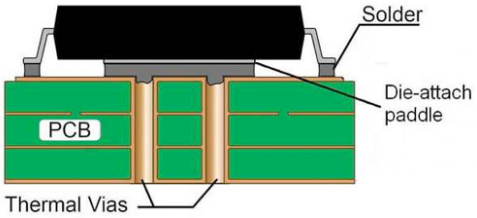

Fig. 4.5: The thermal vias made in a PCB to dissipate the heat produced by the electronic component.

4.2 Mechanical design of the internal side of the DAQ crate walls

In order to accommodate nine electronic boards, the inner parts of both lateral walls of the crate are milled as shown in Fig. 4.6a. Each groove is sufficiently deep to provide enough space for the card lock which fixes the board to the crate (Fig. 4.7). The two additional grooves, one on the top and one on the bottom, allow to open the blind holes of the screws which connect each lateral wall to the bottom and top walls of the crate (Fig. 4.6b). The same picture shows that each groove has a sort of opening on the frontal side; this feature has been added to allow an easier mounting of the boards.

4.2.1 The card lock

We have to choose two different card locks, the longer one to block the waveform digitizer board, the shorter one to block the interface board. We have chosen the card locks from the Calmark catalogue and we have checked they do not use any magnetic material. In order to do that we have chosen the card locks MVEN265-3.80ETM2.5 and MVEN265-8.30ETM2.5. The only difference between the two card locks is the dimension: the shorter one is 3.80 inches long, the longer one is 8.30 inches.

According to the data sheet (Appendix **??**), the choosen card locks are made of aluminum alloy 6061-T6 and 7075-T6, stainless steel per ASTM-A582 and 400 series stainless steel. While the first three metals are non magnetic materials, the last one is a magnetic material and has to be replaced. After asking information directly to the producer, we have been told that the roll pin, which is the only part made out of 400 series stainlees

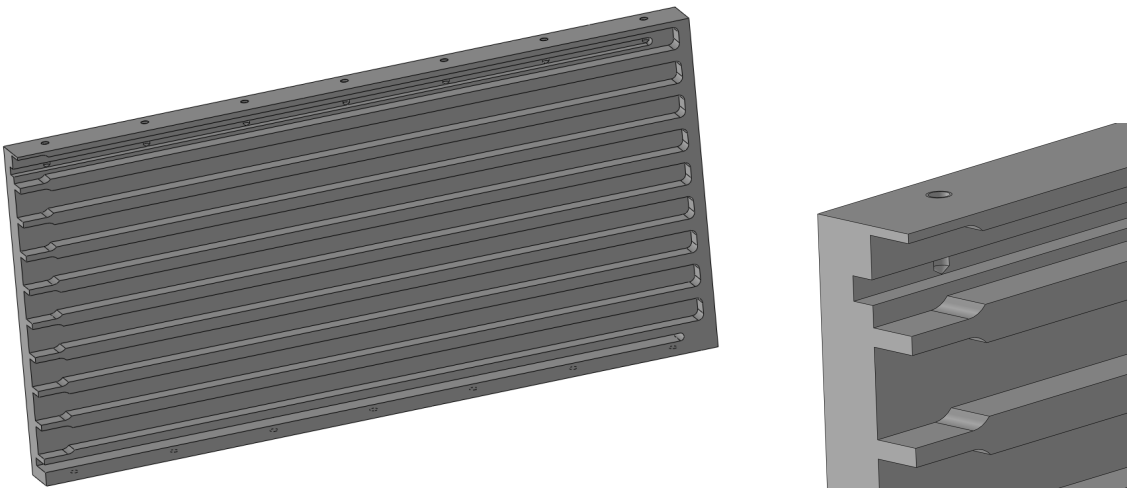

(a) View of the nine grooves milled in the lateral wall of the crate.

(b) Detail of one of the additional grooves used to avoid the blind holes.

Fig. 4.6: Schematic view of the internal side of the lateral wall of the DAQ crate.

Fig. 4.7: Photograph of the Card lock series 265 produced by Calmark.

steel, can be made with the 300 series, which is not magnetic. One of the most important parameter reported in the data sheet is the recommended thickness of the groove that houses the board and the card lock which has to be equal to the board module assembly thickness plus 6.35 mm. According to the data sheet, the setting torque of each card-lock, which is not connected to its length but only to the series and the finishing, is of 68 $N \cdot cm$, with a corresponding clamping force between the board and the lateral wall of the crate of approximately 2100 N. A further important remark is the thermal resistance of the card lock. We can find a minimum and maximum value looking at the curves reported in Fig. 4.8. The length on axis of the abscissas is the total length of the pair of card-locks mounted, it is approximately equal to 7.60 inches for the ones of the interface board and to 16.60 inches for the ones of the waveform digitizer board. In the data sheet there are two important notes which are relevant for our application:

- When the card locks are used in vacuum the thermal resistance reported in the graph can be significantly affected and the values reported in the graph should be increased by a factor between 10% and 40%;

- For the card locks of series 265, which are made of five pieces, with their greater and more distributed clamping force, these potential gradients are greatly reduced. Furthermore, according to the mail conversation with a Calmark technician, using

the black anodize to electroless nickel finishing, the thermal resistance is reduced by a factor of the order 9%.

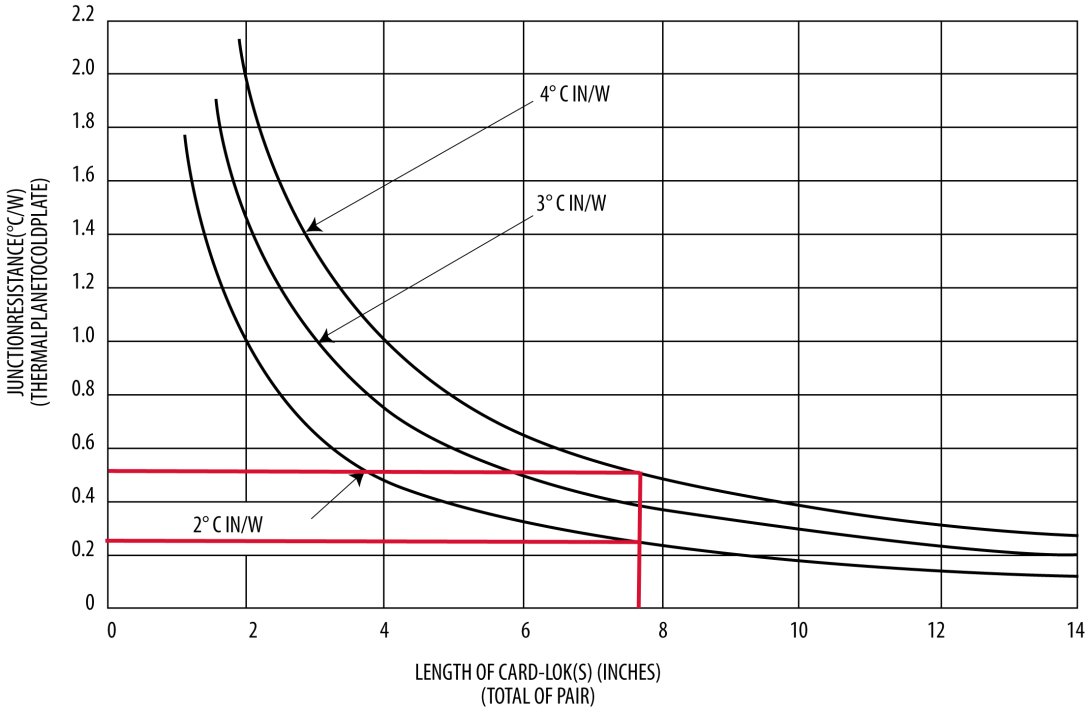

Fig. 4.8: Thermal resistance of the card lock as function of the length of the pair of card locks.

The equivalent thermal resistance of the shortest pair of card lock is between $0.3°C/W$ and $0.5°C/W$, while for the longest one, since it is longer than 14 inches which is the maximum value on the graph, we can estimate a value between $0.1°C/W$ and $0.3°C/W$. Because of the two comments previously reported, this value may result increased by a factor 30% in vacuum. In the most conservative scenario the shorter pair could have a thermal resistance of $0.7°C/W$ and the longer one a thermal resistance of $0.4°C/W$. For the data sheet of all the card locks series (including our choice) refer to [15].

4.2.2 Stacking sequence and position

The chosen mounting position of each board with its card lock is shown in Fig. 4.9a. The top of the board, which is the side of the board on which the compotents are mounted, is directed to the center of the calorimeter. This choice is connected to the requirement that it should be possible to remove each single board independently of the other boards during the maintenance. We have also decided to put the card locks on the upper face of the board because this allows an easier mounting. During the assembly the screw of the card lock is not screwed and so the wedges can move; if the card lock is mounted on the lower face, these wedges go down during the mounting, making the operation more complicated, with the risk of interference between the card lock and the groove milled

in the crate. Fig. 4.9b shows that with the designed solution the head of each screw of each card lock is accessible and allows to remove the boards one by one (there are only 8 of the 9 boards, because the board placed in the middle which is the "clock distributor" board has not been designed yet). In order to remove one digitizer board, we need first to unplug the cables connected to the interface and waveform digitizer boards and then to unscrew the pair of card locks of the mezzanine and gently remove this one; only after having done that we have the access to the screws of the card locks of the digitizer board (Fig. 4.9c).

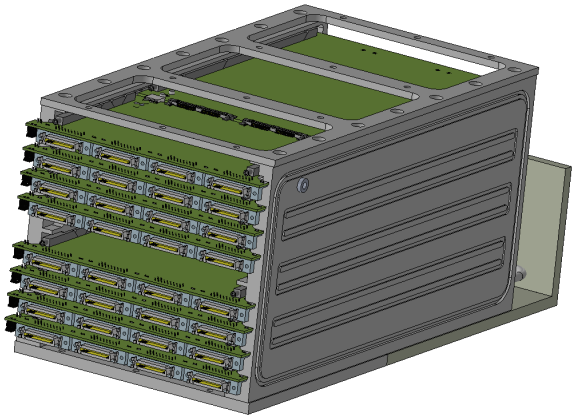

(a) Schematic view of the crate with the 8 pair of interface and waveform digitizer boards mounted: the electronic components of the waveform digitizer are placed on the surface facing the axis of the calorimeter disc.

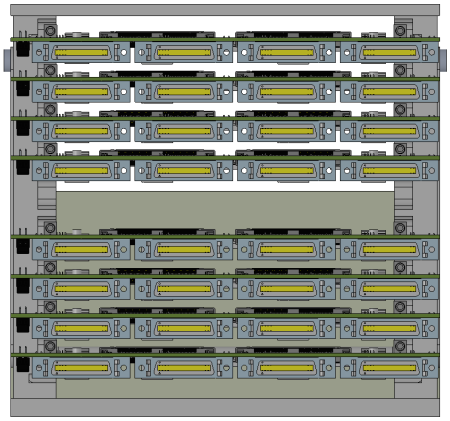

(b) Front view of the crate: the screws of each pair of card lock are accessible for the single card removal.

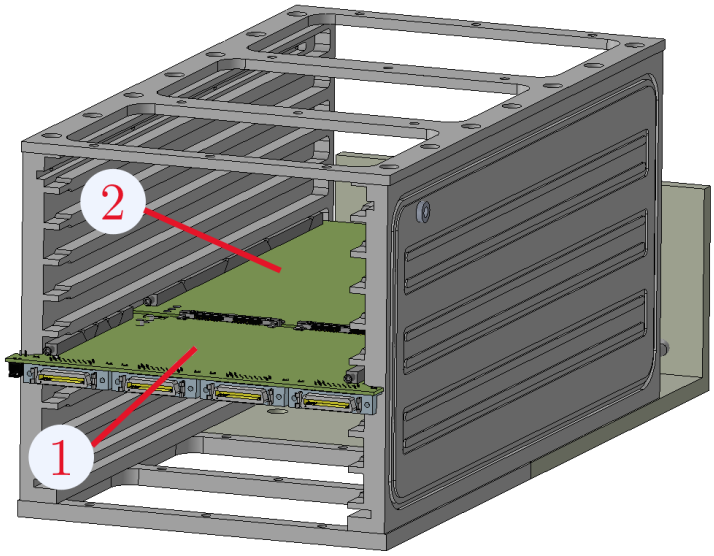

(c) Boards removal order: first unscrew the card locks of the interface board **1** and extract that, after unscrew the card locks of the interface board and extract.

Fig. 4.9: Schematic views of the crate showing the stacking sequence of the boards and the accessibility of the card locks screws.

4.3 Thermal simulation of the waveform digitizer board

In the following sections we will estimate the thermal resistances of each part of the thermal circuits which connect each component of the board to the cooling fluid. Instead of developing one single complex simulation of all the model of the crates with the 9 boards inside, which would be subjected to errors and problems for choice of contacts between parts, we have split the thermal analysis making the simulation of each part of the thermal chain from the cooling fluid to the components. Under conservative assumptions, we have estimated the thermal resistance of each component of the thermal circuit. This has allowed to identify and carefully study all the critical parts.

4.3.1 Simulation of the crate wall

Using the results reported in Section 3.3, we know that the face of the crate wall placed in contact with the fluid has a temperature of approximately $2°C$ higher than the average temperature of the cooling fluid itself. Assuming that the fluid is supplied at the temperature of approximately $-10°C$, we can use an average temperature of the fluid flowing in the crate wall circuit of $-9.5°C$ (remembering that we have imposed a temperature drop of the cooling fluid of $1°C$ along the cooling circuit) and an average temperature for the part of the lateral wall in contact with the fluid of approximately $-7.5°C$. At this point we have identified a "module" of the lateral wall, a repetitive geometrical shape that we find many times in each wall and shown in Fig. 4.10.

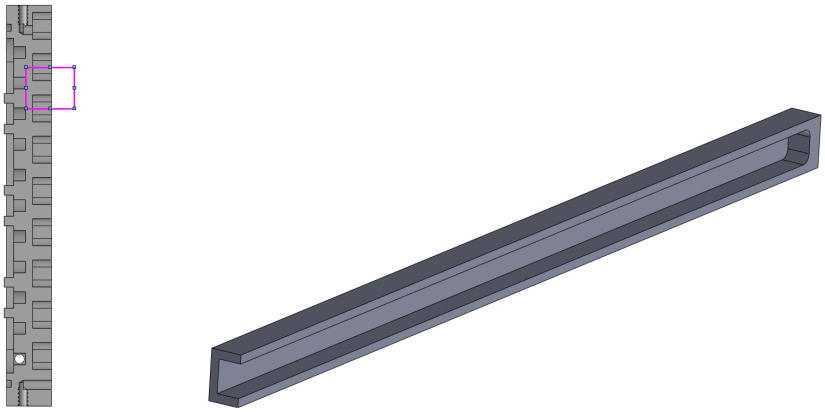

(a) Crate wall overview.

(b) Crate wall module.

Fig. 4.10: The entire crate wall can be obtained from the replica of the elementary structure named "module".

The power dissipated by each pair of interface and waveform digitizer boards is extracted through two identical modules placed on the two lateral walls. Given the symmetry of the boards, each module transfers 50 % of the power which is approximately 17.1 W.

Applying on the module this power and imposing the wall temperature as a boundary condition we have obtained the results shown in Fig. 4.11.

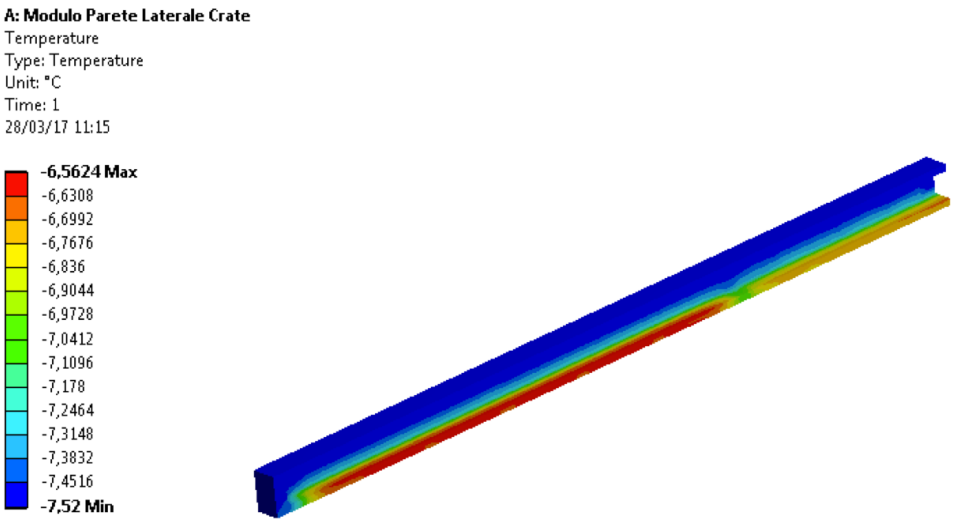

Fig. 4.11: Thermal simulation of one module of the crate wall.

We have obtained a maximum temperature of $-6.5°C$. At this point we have used the conservative assumption to use this maximum value of the temperature to determine the equivalent thermal resistance of the module:

$$R_{wall} = \frac{\Delta T}{W} \approx 0.06 \frac{°C}{W}$$

4.3.2 Optimization of the waveform digitizer layout

Before performing a detailed thermal simulation, we have optimized the board layout. Our goal has been optimizing the position of the components on the board in order to reduce the maximum temperature reached by each of them. This has been checked to be compatible with the design of the PCB. First of all we report the results of the thermal simulation of the digitizer before this optimization, corresponding to the layout we have received from the Electronics Engineers of our group. We have modelled the board with a shell type element and we have used the default material of ANSYS, which is the structural steel. In this study we are not interested in the real temperature of each point of the board but we want just to reduce the gradient between the coldest and the hottest point. We have split the face of the board in order to apply the maximum power of each component in the correct position (Fig. 4.12a). At the lateral edges of the board we have applied a constant temperature. The temperatures obtained are shown in Fig. 4.12b.

In this configuration the central DC-DC converter is the critical component. We need to relocate the components in order to create a "thermal way" between the central DC-DC and the lateral sides of the board. Every configuration has to be symmetrical like

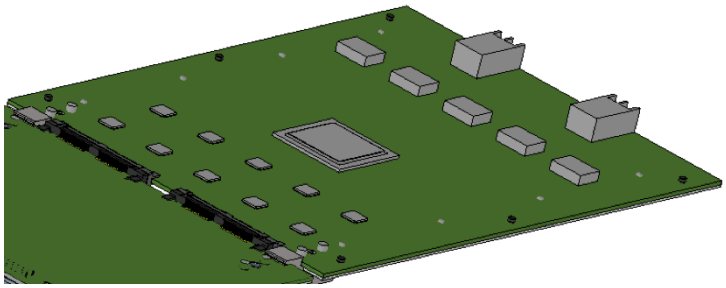

(a) Overview of the position of each component of the not optimized board.

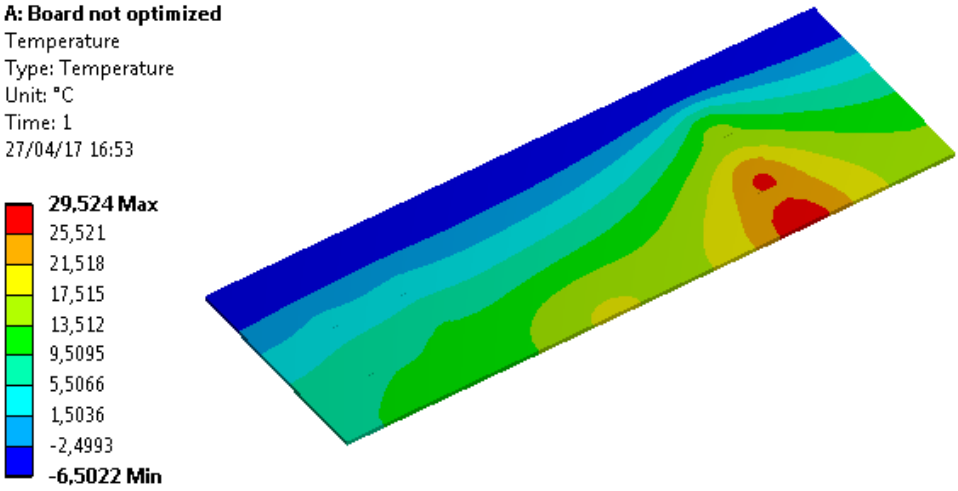

(b) Temperature of the not optimized board.

Fig. 4.12: Thermal simulation of the waveform digitizer with non-optimized positions of the electronic components.

the first one to allow a symmetrical dissipation of power. We have made a preliminary optimization study with the FEM tools of Solidworks, which allows to set the parameters that we want to change (the coordinates of the center of each component in our case) and the variable that we want to optimize (in our case minimizing the maximum temperature reached one the board). The now optimized board layout of the components is shown in Fig. 4.13a. In order to make a comparison with the previous result, we have chosen the same material of the board (structural steel), the same power on each section and the same temperature on the edges. During the running process of this optimization the software does not update the mesh of the board every step. Even if the obtained configuration is the best one for our goal, the temperatures shown could be affected by this. At the end we have performed another single simulation with the components in their final position (Fig. 4.13b).

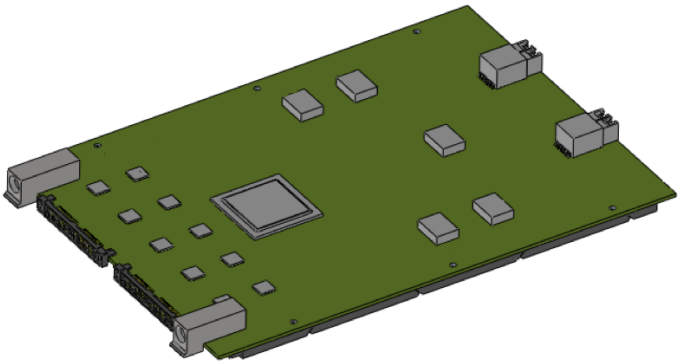

(a) Overview of the position of each component of the optimized board.

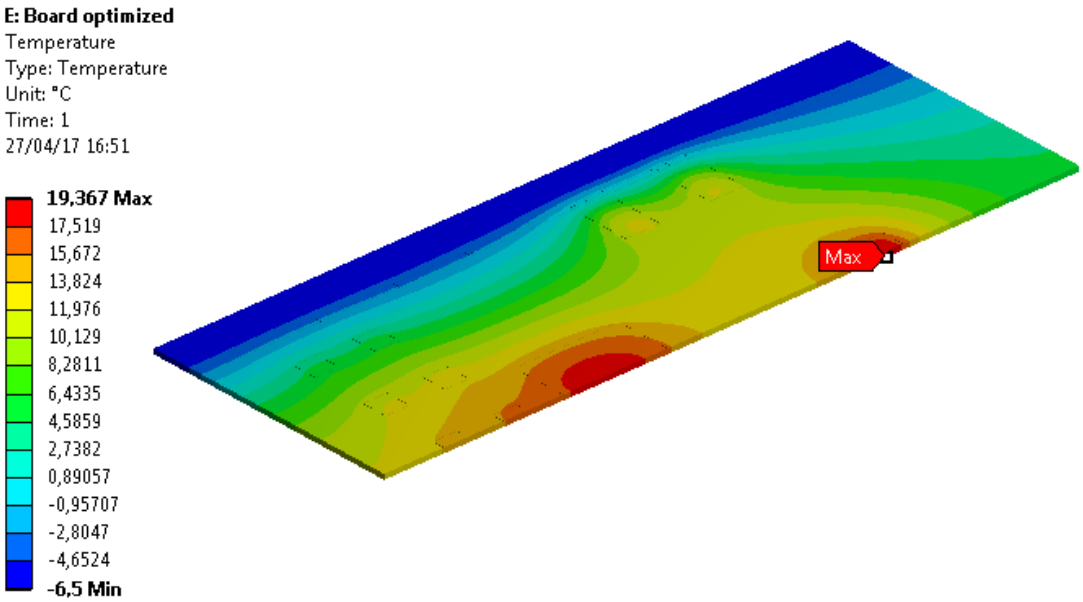

(b) Temperature of the optimized board.

Fig. 4.13: Thermal simulation of the waveform digitizer with the optimized positions of the components.

4.3.3 Thermal resistance of the board with the copper film

Once we have chosen the optimized position of each component, we have determined the thermal resistance of the board viewed from each component. Because of the low thermal conductivity of the epoxy fiberglass we use the $75\mu m$ layer of copper, which is the thickest layer which can be added to the board (4.1.1). Since the components on the board have to be electrically insulated from the crate, we have to stop the copper layer near the edges of the board and to put an electrically insulator but thermal conductor material as thermal bridge between the copper and the crate wall itself.

The idea is to use bridge resistors which are blocks of Beryllium oxide (BeO). The mechanical characteristics of the bridge resistor are reported in Fig. 4.15. The total thermal resistance of the component is $13°C/W$. Assuming only axial conduction along

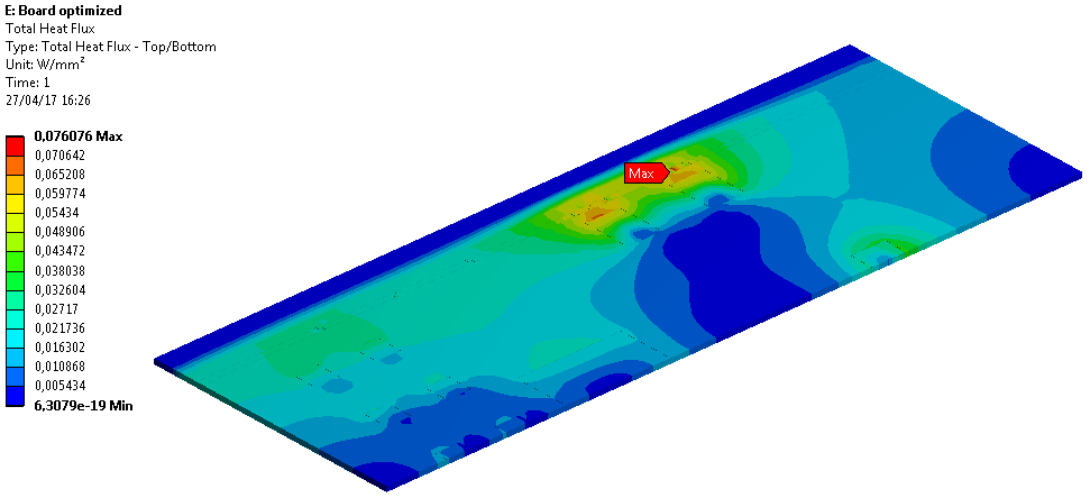

Fig. 4.14: Total heat flux on the waveform digitizer with the optimized positions of the components.

Dimensions

Size (EIA)	Length (L)	Width (W)	Standard Thickness (T, mils) A	Standard Thickness (T, mils) B	Termination (t)
0402	0.040 ±.002 (1.02 ±0.051)	0.020 ±.002 (0.51 ±0.051)	20	15	0.010 ±.002 (0.25 ±0.051)
0603	0.060 ±.002 (1.52 ±0.051)	0.030 ±.002 (0.76 ±0.051)	25	20	0.015 ±.002 (0.38 ±0.051)
0805	0.080 ±.002 (2.03 ±0.051)	0.050 ±.002 (1.27 ±0.051)	40	25	0.020 ±.002 (0.51 ±0.051)

inches (mm)

Mechanical Configurations

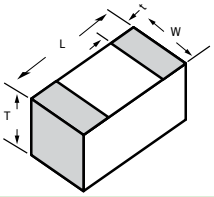

Fig. 4.15: Bridge resistor main dimensions.

the longest length the equivalent thermal conductive coefficient is:

$$k_{BR} = \frac{L}{WTR} \approx 220 \frac{W}{m°C}$$

For the complete bridge resistor data sheet refer to Appendix **??**. We have placed a total of 18 bridge resistors on the waveform digitizer, located symmetrically, in the regions where the thermal gradient is maximum (Fig. 4.14[1]). We have made a FEM simulation using shell elements. In order to simplify the model, we have modelled a material with a thermal conductivity equivalent to the one of the layers in parallel. Even if the real model is much more complex, we have developed a simplified simulation assuming that only one layer of copper and 1 mm layer of epoxy fiberglass contributes to the thermal dissipation. We have 3 types of package parallel layers:

- Epoxy fiberglass + copper layer;
- Epoxy fiberglass + bridge resistor berillyum oxide layer;
- Only epoxy fiber glasse layer.

[1]Actually figure shows the total heat flux, which is proportional to the gradient according to $\vec{q''} = -\lambda \nabla T$

Using the thickness of each material and its thermal conductivity and remembering that:

$$R_{//} = \left(\frac{1}{R_1} + \frac{1}{R_2}\right)^{-1}$$

We have that:

$$k_{BR+Epoxy} = 110\frac{W}{mK} \qquad R_{Copper+Epoxy} = 26.6\frac{W}{mK}$$

We have used this equivalent conductivities for the material used on each part of the board. For a quicker simulation we have also used the symmetry and we have simulated only half of the board, applying again the maximum on the area of each component and a constant temperature on the lateral edge equal to the one of the wall module ($-6.5°C$). Fig. 4.16 shows the result.

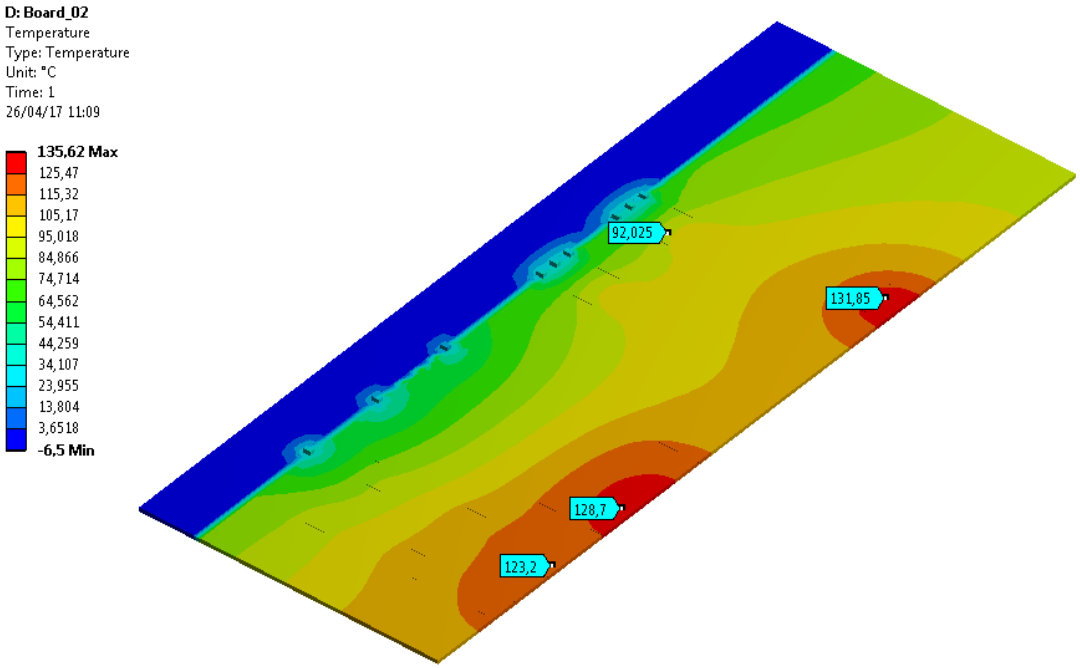

Fig. 4.16: Temperatures on waveform digitizer board with single bridge resistors brazed near the edge.

We have assumed that $R_i = (T_i - T_{edge})/W_i^{max}$ and we have estimated:

$$R_{DC-DC} \approx 47\frac{K}{W} \quad R_{FPGA} =\approx 34\frac{K}{W} \quad R_{ADC} \approx 258\frac{K}{W}$$

Even assuming a contact resistance equal to 0 between the crate and the board, the temperature reached on the components is higher than the one requested in 4.1. Also for the DC-DC converter, according to the maximum chosen temperature, equal to the half of the maximum given in the data sheet and so equal to $62.5°C$, considering that in this configuration all the heat is removed from the bottom we have that the maximum allowed

temperature on the board in the region occupied by each DC-DC is:

$$T = \frac{T_{DC-DC}^{MAX}}{2} - (\theta_{JCbottom} + \theta_{JB})\, W_{DC-DC}^{MAX} = 17.5°C$$

A second simulation has been performed assuming to leave the use of commercial bridge resistors and adopting a beam made out of Beryllium oxide with the same leght as the board, properly prepared to be brazed on the copper film. In that case the thermal resistance viewed from each components is reduced, as shown in Fig. 4.17.

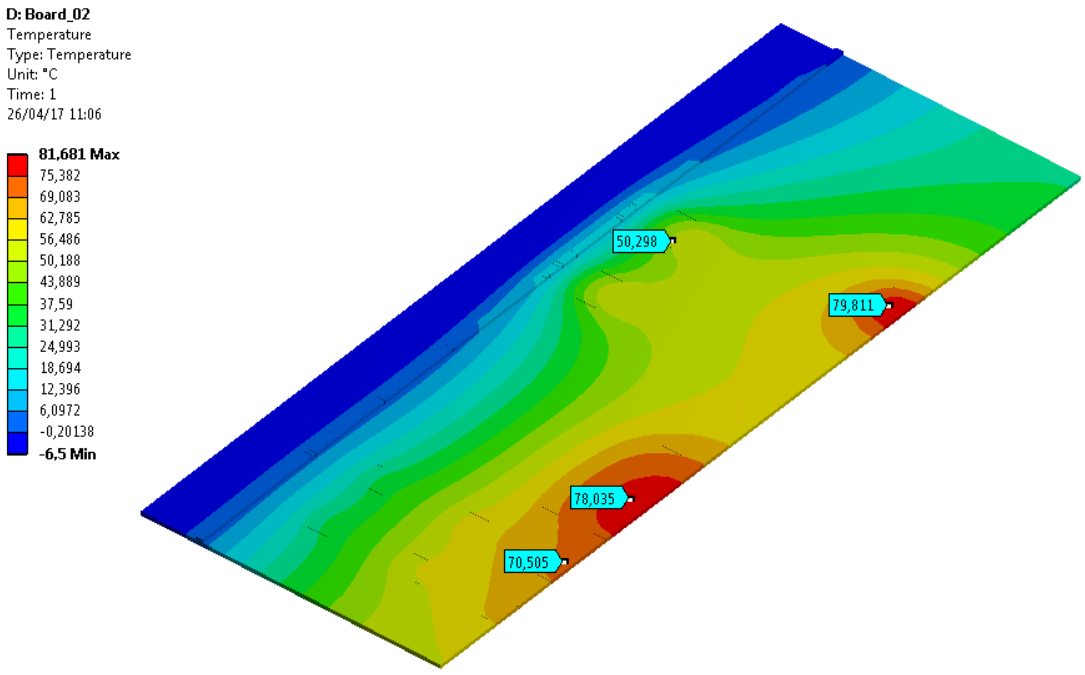

Fig. 4.17: Temperatures on waveform digitizer board with a single beam of Beryllium oxide brazed near the edge.

Even with this solution the temperatures of the FPGA and the DC-DC converters exceed the maximum allowed values. Therefore we need to improve the heat dissipation mechanism.

4.3.4 Thermal resistance of the additional aluminum plate

If we can't change the main board material, the epoxy fiberglass, which has the lowest thermal conduction coefficient, we need to remove the heat also from the top of each component. In the next simulation we will make the conservative assumption that all the power is removed from the top and we will neglect the small contribution due to the copper layer on the board which have been already simulated. The easiest way to connect thermally the top of the components with the cooled wall of the crate is a shaped plate made out of aluminum, connected to the board using the same screws used to fix the card

lock. For the thickness t of this part, also called in the following section "thermal plate", we have to find a compromise between two opposite requirements:

- A thicker plate has a lower thermal resistance; in fact we know that $R = l/(kA)$ and so $R \propto 1/t$;
- A thicker plate can be harder to be made by plastic deformation with a comparable bending radius and it would be necessary to obtain that by milling, which is more expensive; furthermore a thicker plate would not allow to remove the boards from the crate one by one, as we have explained in Section 4.2.2.

We have added a properly shaped 3 mm thick aluminum plate to the thermal model (Fig. 4.18).

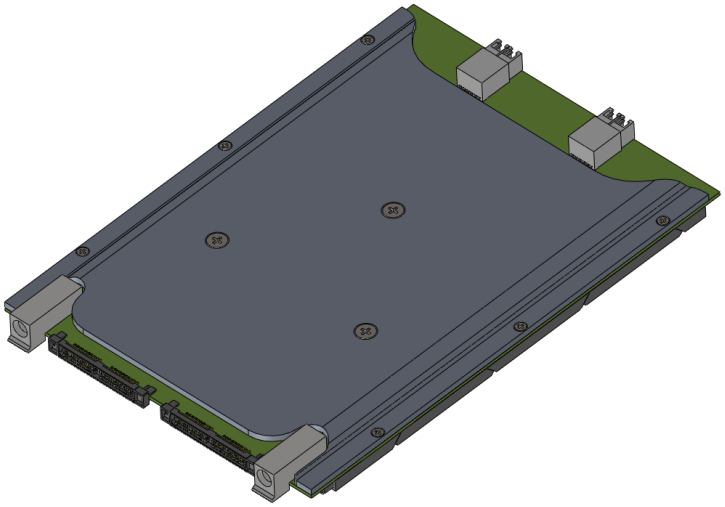

(a) Overview.

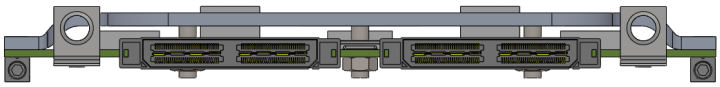

(b) Front view.

Fig. 4.18: Views of the board of the digitizer with the aluminum thermal plate on it.

At this point we have made a thermal simulation to view the effectiveness of this solution. The maximum power of each component has been applied on a cut area on the 3D model of the plate equivalent to the projection of the component itself on the plate. This model is based on the assumption that the contact area between the components and the thermal plate is the whole top surface of each one. The ways that can be used to guarantee this contact will be discussed in 4.6. Fig. 4.19 shows the result of the simulation.

We have estimated the thermal resistances viewed from the FPGA, the hottest ADC and DC-DC converter:

$$R_{FPGA} = 2.2\frac{K}{W} \qquad R_{ADC} = 16.2\frac{K}{W} \qquad R_{DC-DC} = 2.8\frac{K}{W}$$

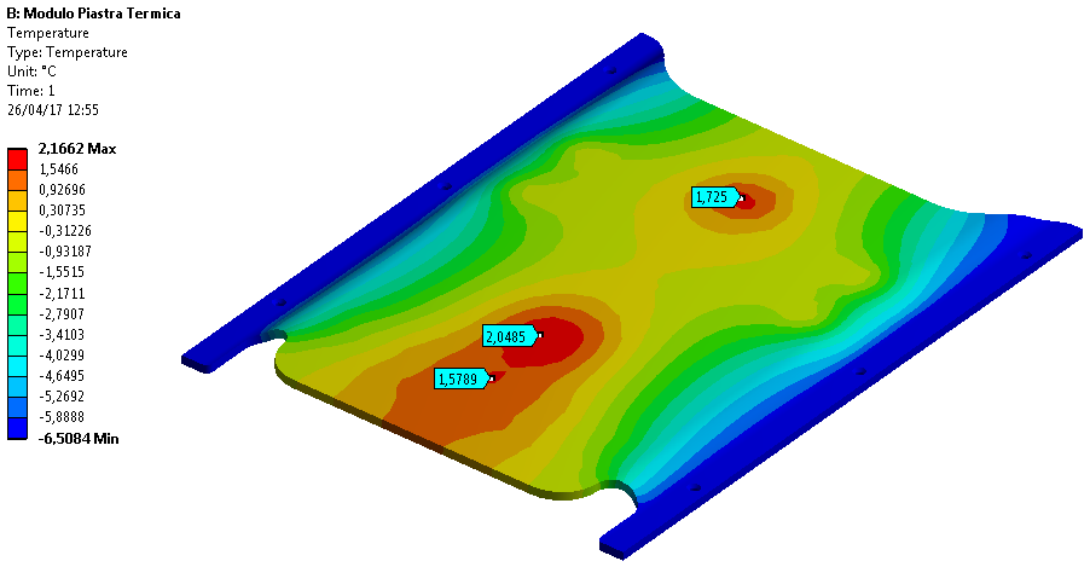

Fig. 4.19: Temperatures on waveform digitizer thermal plate added to improve the heat exchange.

These results show that, even if the highest resistance is the one of the ADC, the critical components are the central DC-DC and the FPGA. In fact the FPGA, following the information reported in 4.1, must have a temperature on the top of its case below $34.8°C$, against the over $70°C$ that we can have on the top of the ADC. For the DC-DC converter the situation is worse: assuming that all the heat is removed from the top and using information given in 4.1, we have that:

$$T = \frac{T^{MAX}_{DC-DC}}{2} - \theta_{JCtop} W^{MAX}_{DC-DC} \approx 12°C$$

At this point the critical and important component is the one chosen to connect the head of each component with the thermal plate, largely discussed in 4.6.

4.4 The problem of the contact thermal resistance

In the thermal simulation described in the previous Section we have assumed that the contact between each component is perfect and the resulting contact thermal resistance is 0. In reality, given the roughness of each surface, the actual contact area between the two surfaces is lower than the geometric area. Because of that there is a temperature drop between the two surfaces (Fig. 4.20). In the following sections we will briefly report on the theory and the main equations which describe this phenomenon. For a more detailed description see [16].

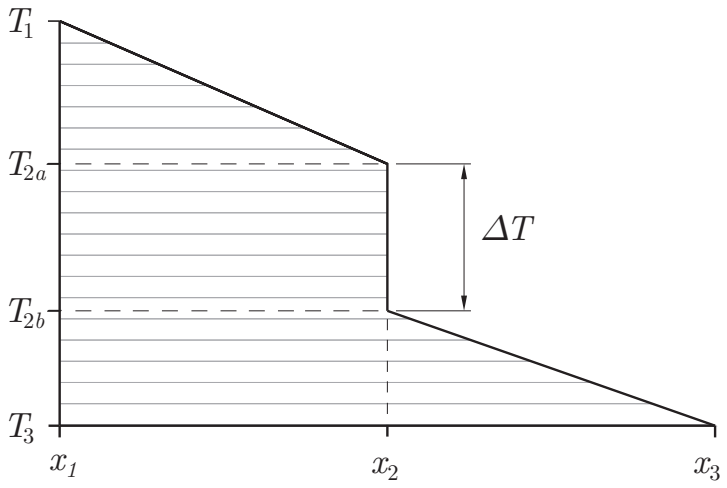

Fig. 4.20: Graphical representation of the temperature drop ΔT at $x = x_2$.

4.4.1 Theory of thermal contact conductance

Heat flux through an interface between two surfaces in contact is subject to a thermal contact resistance, defined as:

$$R_j = \frac{\Delta T}{Q} = \frac{\Delta T}{qA}$$

The main physical reason for the contact resistance is that the actual contact area is lower than the purely geometric one, so $A_r/A_a < 1$ and the value of this fraction depends on several parameters such as surface roughness, surface hardness, contact pressure and temperature itself. The conductance of the contact is defined as the inverse of the resistance, given by:

$$h_j = \frac{1}{R_j A} = \frac{q}{\Delta T}$$

There are three contributions to this conductance which act in parallel:

$$h_j = h_c + h_g + h_r$$

where:

- h_c: the thermal conductance between the contacting surfaces of the two interface materials;
- h_g: the conductance through the small, gas-filled gaps between the two materials; since our problem is in vacuum this term is approximately 0;
- h_r: thermal conductance due to radiation emission from the surfaces; If the temperature of the surface is below $600°C$ also this term is approximately 0.

Within reasonable assumptions, we have: $h_c = h_j$.

4.4.2 Formulas and correlations

The equations reported below define parameters that will be used in thermal contact conductance models. An illustration of two surfaces placed in contact is shown in Fig. 4.21, with graphical representations of the main parameters.

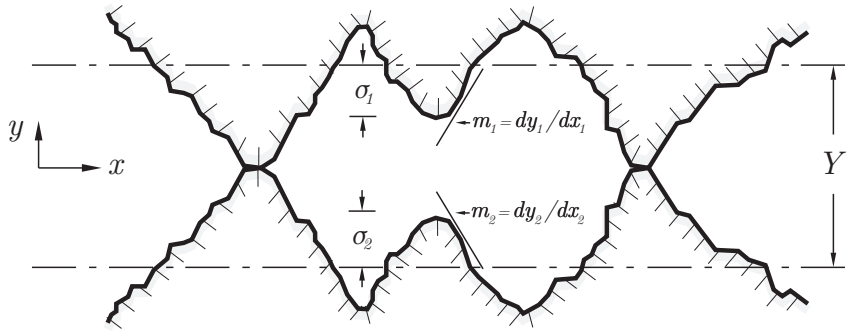

Fig. 4.21: Graphical representation of two contacting surfaces, showing asperities and the absolute surface slope m and the RMS surface roughness σ.

Effective thermal conductivity

$$k_s = \frac{2k_1k_2}{k_1 + k_2}$$

where the subscripts 1 and 2 correpsond to the two materials of the joint.

Roughness

The level of roughness of a surface is commonly quantified with the arithmetic average roughness, R_a, and the RMS roughness (Root Mean Square), σ:

$$R_a = \frac{1}{L}\int_0^L |y(x)|\, dx \qquad \sigma = \sqrt{\frac{1}{L}\int_0^L y^2(x)dx}$$

If we assume that the surface has a Gaussian distribution of the asperities we have:

$$\sigma = \sqrt{\frac{\pi}{2}}R_a \approx 1.25R_a$$

The effective RMS surface roughness is given by:

$$\sigma_s = \left(\sigma_1^2 + \sigma_2^2\right)^{\frac{1}{2}}$$

Slope

Another common surface parameter is the absolute average asperity slope, m. Similarly, the absolute average asperity slope, m, and the RMS asperity slope, m' are relating:

$$m' = \sqrt{\frac{\pi}{2}} m \approx 1.25m$$

The effective absolute mean asperity slope is given by:

$$m_s = \left(m_1^2 + m_2^2\right)^{\frac{1}{2}}$$

4.4.3 Elastic and plastic models

Assuming elastic deformation generally gives a model that depends on the modulus of elasticity of the contacting materials while assuming plastic deformation generally gives a model that depends on the surface hardness of the contacting materials. Let Ψ be the index of plasticity defined by Mikic (1974) as follows:

$$\Psi = \left(\frac{E'}{H_c}\right) m$$

Where H_c in MPa is the micro-hardness of the softer material of the couple and E' is equivalent Young Modulus of the couple of materials[2]. Mikic demonstrated that plastic deformation occurs when $\Psi > 1$. Assuming elastic deformation, the proposed thermal contact conductance model is given by:

$$h_c^{Mikic} = 1.55 \frac{k_s m_s}{\sigma_s} \left(\frac{P\sqrt{2}}{E' m_s}\right)^{0.94}$$

Where P is the pressure of contact between the components. Assuming plastic deformation, the proposed thermal contact conductance model is given by:

$$h_c^{Tien} = 0.55 \frac{k_s m_s}{\sigma_s} \left(\frac{P}{H_c}\right)^{0.85}$$

For both elastic and plastic model there are many other relations of the chosen ones. We have decided to use the easiest ones to obtain a first value of the resistance of contact to compare that with the other resistencas. If the contact joint will be the critical part, we are going to use more complex and exact relations, otherwise we will mantein this first step values.

[2] $E' = \left(\frac{1-\nu_1^2}{E_1} + \frac{1-\nu_2^2}{E_2}\right)^{-1}$

4.4.4 Our case

Fig. 4.22 shows that in our specific case there are 2 interfaces:

- aluminum thermal plate - aluminum crate wall;
- aluminum thermal plate - copper film on the board.

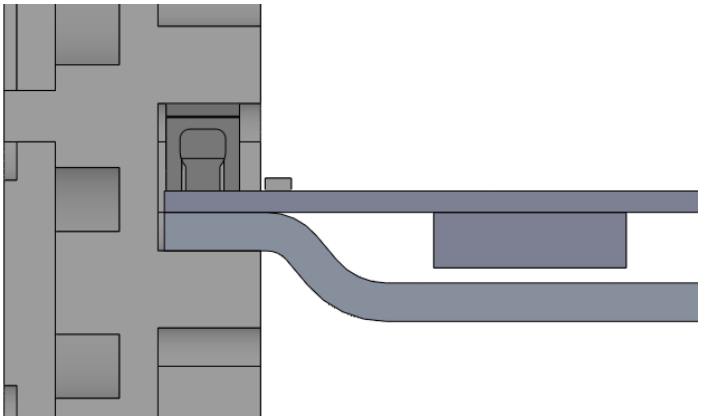

Fig. 4.22: Cut view of the main interfaces.

We have not considered the thermal interface between the copper film and the epoxy fiberglass of the board. Both the thermal plate and the crate are made out of the same 5083 aluminum. Table 4.4 reports the properties of the Al 5083 and the Copper.

Property	**5083**	**Cu**
$k\,[W/mK]$	121	400
$H\,[MPa]$	850	350
$E\,[GPa]$	70.3	115
ν	0.33	0.36
$R_a\,[\mu m]$	1.6	1.6
m	0.03	0.03

Table 4.4: Properties of the contact materials.

Using the values given in Table 4.4 we see that $\Psi > 1$ for both the couples aluminum-aluminum and aluminum-copper, so we can use Tien realtion for plastic situation. With the clamping force $F = 2113N$ given by the card-lock we find:

$$h_{Al-Al} \approx 3700\,\frac{W}{m^2K} \quad R_{Al-Al} \approx 0.15\,\frac{K}{W}$$

$$h_{Cu-Al} \approx 12000\,\frac{W}{m^2K} \quad R_{Cu-Al} \approx 0.05\,\frac{K}{W}$$

4.5 Thermal simulation results

Fig. 4.23 shows the thermal resistances of the cooling fluid and of the components between the fluid and the aluminum plate while Fig. 4.24 shows the resistances between the edge of the thermal plate, the edge of the board and the inner thermal resistance of each electronic component.

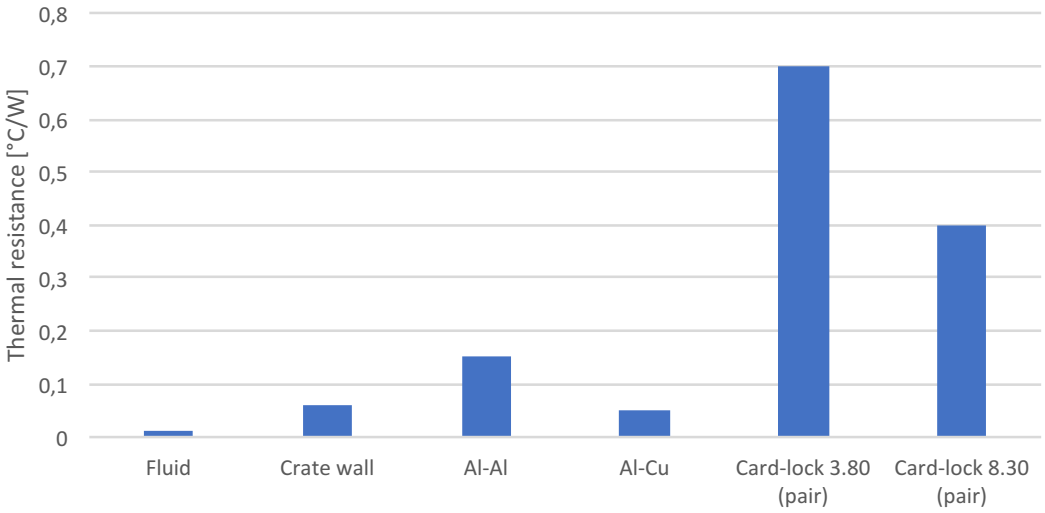

Fig. 4.23: Estimate of the resistance of the elements of the thermal circuit between the fluid and the aluminum thermal plate, including the card-lock and the copper-aluminum contact resistance

Fig. 4.25 shows the graph of the edges temperatures of each module considered and (Fig. 4.26) shows the temperatures reached on the thermal plate, at the position occupied by each electronic component.

4.6 Thermal gap filler solution

Fig. 4.18b shows there is a gap between the aluminum thermal plate and the components mounted on the digitizer. In order to allow the heat flux, there has to be a contact and the empty space has to be filled with the proer material. Fig. 4.26 shows that the central DC-DC converter is the most critical component since it reaches a temperature close to the critical temperature. The choice of the gap filler will be done referring to this component and will be validated also for the other ones. Considering the maximum power dissipated of $3\,W$ of the DC-DC converter and the values obtained in the graph, we have:

$$R^{MAX}_{Gap\,filler} = \frac{\Delta T^{MAX}_{Gap}}{W^{MAX}_{DC-DC}} \approx 2.8\,\frac{^\circ C}{W}$$

The material has to be soft enough to cover a wide field of tolerances of the components

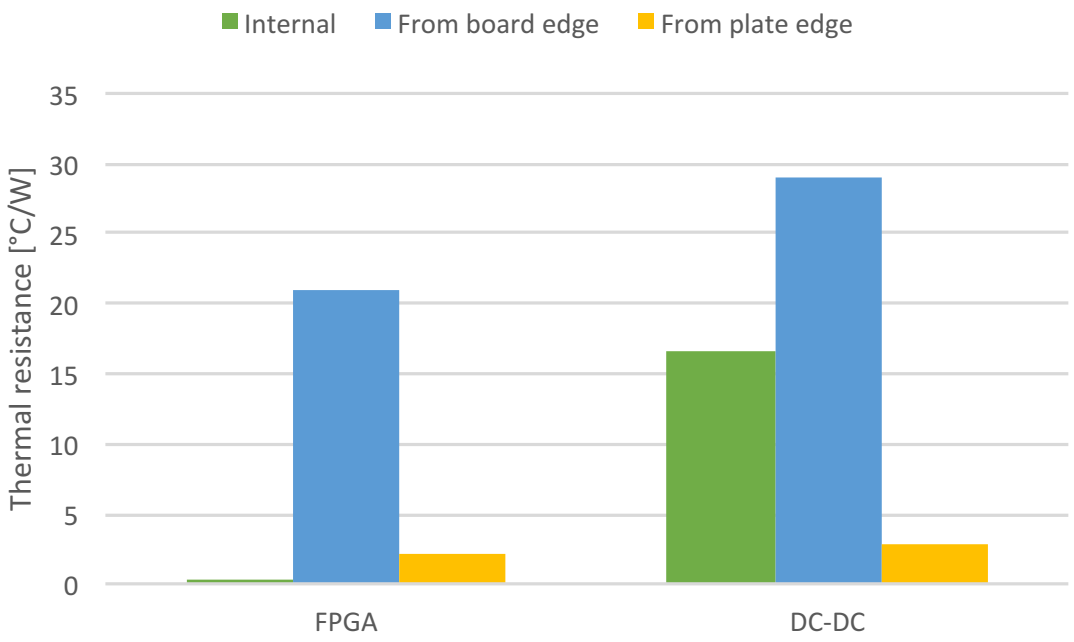

Fig. 4.24: Estimate of the thermal resistance between the electronic components and the DAQ crate wall. The green one is the component internal resistance; the light blue one is the thermal resistance between the edge of the fiberglass+copper board and the component (estimated in Section 4.3.4); the yellow one is the resistance between the lateral edges of the aluminum plate and the electronic component. The resistances of the ADC have not been shown because they are too large, even if the temperature of this component is the lowest because of its low power. The DC-DC resistance reported is relative to the most critical component which is placed in the central position on the board.

thickness. Significant stresses of components which will deform the board and probably break the components have to be avoided. Looking at the dimensions of the components and in particular to the ones of the FPGA Table 4.2, we see that for this component we have the highest field of tolerance equal to $0.56\,mm$. Assuming also to add a tolerance relative to the components brazing on the board, we can assume a maximum value of $0.8\,mm$. We notice that there are two different requests which go in opposite direction:

- the fact that the strain of the gap filler is $\varepsilon = \frac{\Delta s}{s_0}$, where s_0 is the initial thickness of the gap filler, and $F \propto \varepsilon^n$, we have to increase s_0 in order to reduce ε and the maximum force F applied to the components;
- since the thermal resistance $R_{Gap} \propto (s_0 + \Delta s)$, we need to reduce s_0 in order to optimize the heat transfer.

At the end we will use the following information for the choice of the gap filler:

- $R_{Gap} \leq 2.8\,°C/W$;
- $\Delta s^{MAX} = 0.8\,mm$;

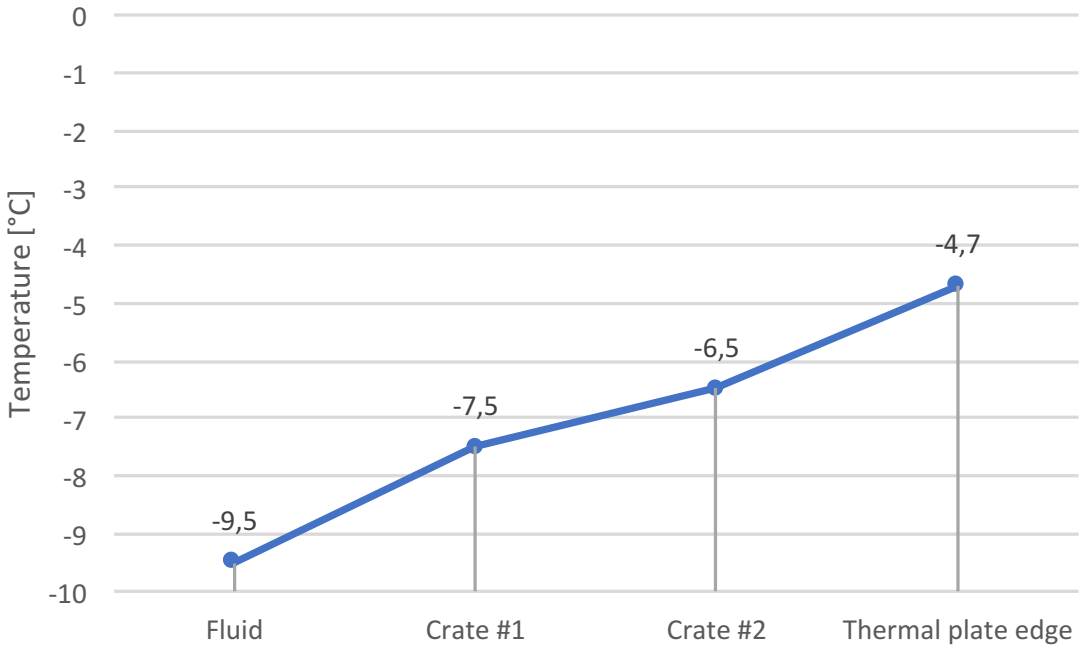

Fig. 4.25: Temperatures at the edges of each module. With "Crate #1" we have identified the surface of the crate in direct contact with the cooling fluid, while with "Crate #2" the surface in contact with the thermal plate.

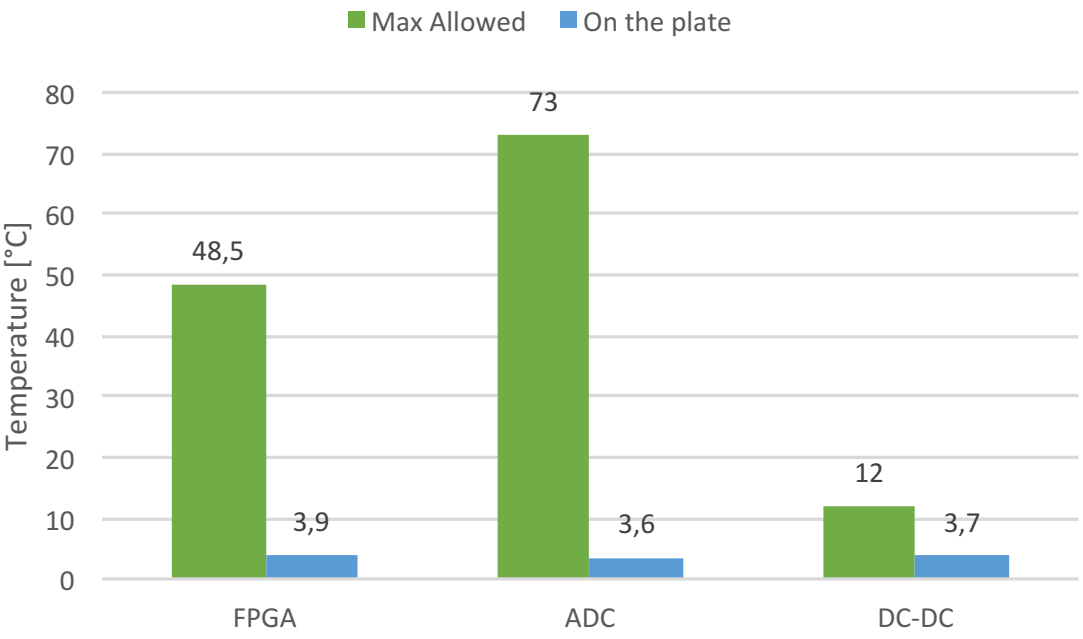

Fig. 4.26: Temparature reached on the thermal plate at the position of each electronic component (light blue). We have reported also the maximum temperature allowed (green) on the top of the case of each component, calculated in the conservative assumption that the component dissipates its maximum power and that all the heat flux is removed from the top. The DC-DC and ADC temperatures reported are the ones relative to the most critical components.

- $F^{MAX} = 2\,N$.

Item	CPSS	Test Method
Thickness $[mm]$	1 ± 0.1, 2 ± 0.2, 3 ± 0.3, 4 ± 0.4	-
Standard sheet size $[mm]$	$210 \times 510 \pm 2.5$	-
Color	Dark green	
Thermal conductivity $[W/mK]$	2	Hot wire method
Hardness	8	Asker C
Volume resistivity $[\Omega\, cm]$	10^{12}	MCC method
Dielectric breakdown voltage	$1.0\, mm = 1\, kV$, $3.0\, mm = 3\, kV$	
Operating temperature	$-20\,°C \div +100\,°C$	ASTM D 2240
Flame resistance	UL94 V2	UL94
Outgassing	TBA	ASTM E 595

Table 4.5: Silicon-free thermal pad properties.

4.6.1 Thermal pad

The first solution is a thermal pad, such as the CPSS series produced by the company KGS, shown in Fig. 4.27 and whose properties are reported in 4.5.

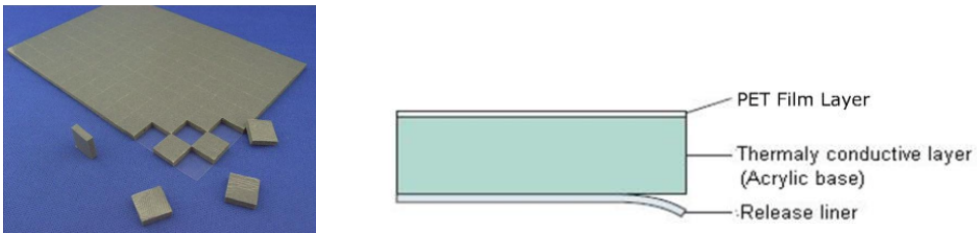

(a) 3D view. **(b)** Composition of the thermal pad.

Fig. 4.27: Silicon-free thermal pad produced by the company KGS.

According to the data sheet, considering the whole surface A of the DC-DC converter of $15\, mm \times 11.25\, mm$ and a maximum thickness $s = 1\, mm$, we have:

$$R = \frac{s}{\lambda A} \approx 3\,°C/W \qquad T_{DC-DC\,top} \approx 13\,°C$$

The temperature rise is slightly larger than allowed. We have also too add that even if the producer says that the material of these pads is lower outgassing and compatible with vacuum, we should test some samples to see how the pad really behaves in vacuum, especially to be sure that it does not shrink and it keeps a physical contact with the electrical. For the complete data sheet of this component see **??**.

4.6.2 Liquid Thermal Interface Material (Liquid TIM)

Liquid TIMs are thixotropic materials that hold their shape until displaced by an external force (Fig. 4.28). They are an alternative to the elastomeric gap fillers shown before. According to the article reported in Appedix **??** they have a thermal conductivity of about $1.8\, W/mK$, corresponding to a thermal resistance approximately of $2.05\,°C/W$.

They have a viscosity of $\approx 10\,Pa\,s$, between two and five orders of magnitude lower than the pads. This provides a larger surface area for heat conduction and supports a wide variety of assembly tolerances. Furthermore liquid gap fillers' moduli are of the order of 102 Pa and they can thin out to about 0.1 mm, the size of the filler material, with minimal stress on the components. Depending on the volume of the required gap filler these liquid TIMs can be applied with a manual or pneumatic dispensing gun or with a partially or fully automated dispenser.

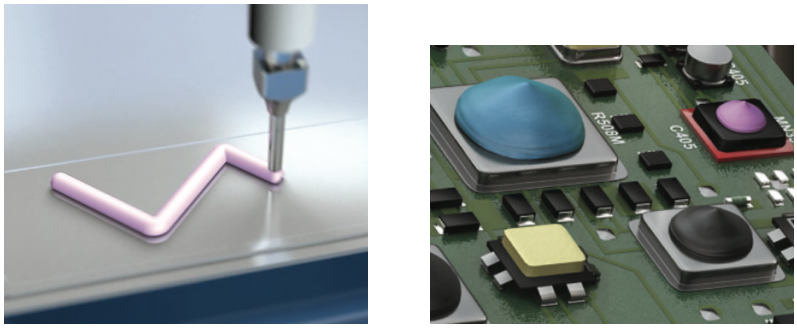

(a) **(b)**

Fig. 4.28: Liquid TIMs application examples.

We notice that the thermal and mechanical properties seem be promising for our use. However no information is provided about the outgassing and radiation hardening parameters and so we should test some samples to check how they really behave in vacuum and if exposed to radiation.

4.6.3 Copper-beryllium spring

We have tried to design a set of springs made of copper-beryllium, to optimize them in order to respect the requests of Section 4.6. We have design a 0.1 mm thick copper spring (Fig. 4.29a). Because of the its length and width (chosen to maximize the heat exchange), we need 3 springs for each DC-DC converter. We have performed a thermal simulation appling 1/3 of the total power dissipated by one DC-DC converter and we have obtained the result shown in Fig. 4.29b, which gives a thermal resistance $R_{Cu\,spring} \approx 20\,\circ C/W$. The mechanical simulation of the reaction force of the spring under the maximum displacement (0.8 mm) gives $F_{reaction} \approx 2\,N$, for a total of $6\,N$ for three springs.

We notice that, even if the copper-beryllium is for sure radiation tolerant and it does not outgas, its thermal and mechanical properties are not compatible with our constraints. We underline also that an improvement of its thermal behaviour (increasing the thickness) is followed by a higher reaction force.

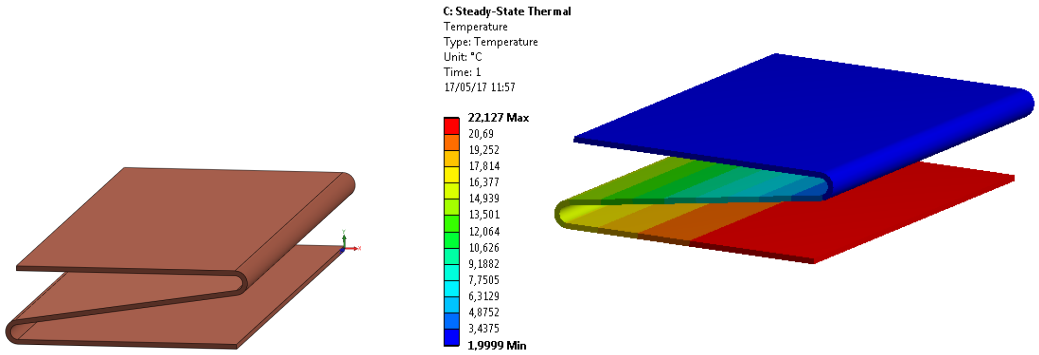

(a) CAD model of the designed copper-beryllium spring.

(b) Temperature from the thermal simulation of the copper beryllium spring.

Fig. 4.29: Model and thermal simulation of the copper-beryllium spring.

4.6.4 Copper wool

A reasonable compromise between a soft, not outgassing and good thermal conductor material is the copper wool, shown in Fig. 4.30. We have contacted one of the producers of this kind of wool, Coppower by Green Steel Group (GSG) and we have requested a sample of each of the three kind of wool they distribute (fine, medium and big). This kind of product is sold per meters. Table 4.6 reports the main properties of the coil, given by the producer by mail.

(a) Round copper wool pad.

(b) Square copper wool pad.

Fig. 4.30: Samples of copper wool pads.

Property	**Value**	**Symbol**
Coil width $[mm]$	≈ 150	w
Weight $[g/m]$	≈ 200	λ

Table 4.6: Properties of the copper wool coil.

In order to have a preliminary estimate of the resistance of the wool, we have assumed that the relative density $\bar{\rho}$ of the wool is function of its thickness s:

$$\bar{\rho}(s) = \frac{\lambda}{w\, s}$$

Since the density can not be higher than the copper density, we have that:

$$s_{min} = \frac{\lambda}{w\,\rho_{Cu}} = \approx 0.15mm$$

At this point we can make the assumption that:

$$\frac{\bar{\rho}}{\rho_{Cu}} = \frac{\bar{k}}{k_{Cu}} \Longrightarrow \bar{k} = \frac{\bar{\rho}}{\rho_{Cu}} k_{Cu} = \left(\frac{\lambda\, k_{Cu}}{w\,\rho_{Cu}}\right)\frac{1}{s}$$

At the end we have obtained a parabolic curve given by the equation:

$$R(s) = \frac{\rho_{Cu}\, w}{k_{Cu}\, A\, \lambda} s^2$$

Using the value given in Table4.6, $\rho_{Cu} = 8920\,kg/m^3$, $k_{Cu} = 350\,W/(m\,K)$ and $A = 15\,mm \times 11.25\,mm$ of the DC-DC converter, we have the graphs shown in Fig. 4.31.

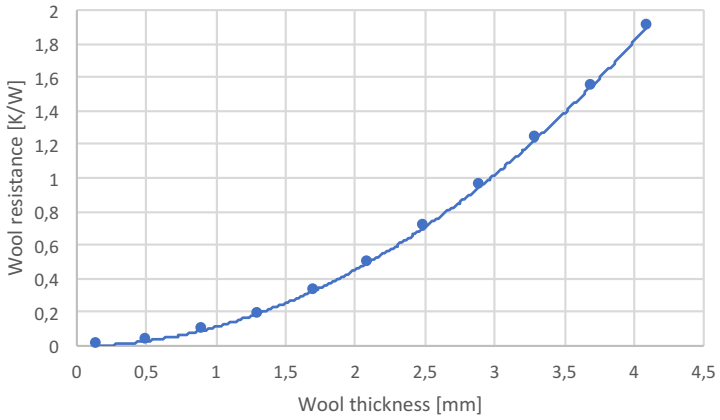

(a) Dependence of the copper wool thermal resistance on thickness.

(b) Graph of the temperature drop caused by the copper wool gap filler.

Fig. 4.31: Graphs relative to the thermal properties of the gap filler made out of copper wool.

In reality, since we stack up a number n of layers of copper wool in the gap of thickness s, assuming that each layer has the same deformation we have that:

$$R_i = \frac{\rho_{Cu}\, w}{k_{Cu}\, A\, \lambda} \left(\frac{s}{n}\right)^2$$

$$R_{TOT} = \sum_{i=1}^{n} R_i = \frac{\rho_{Cu}\, w}{k_{Cu}\, A\, \lambda} \frac{s^2}{n}$$

With a number n of layers the real graphs of the total resistance in the gap and the temperature drop are n times lower than the ones shown in Fig. 4.31. The solution of the copper wool has been presented and one of the main problem which has been pointed is that, since that the copper wool is made out of little wires tangled, there is the risk that some little pieces leave the wool and go around on the board, causing short circuit between the components mounted on the digitizer. In order to avoid that we can design a "double-glasses" case, shown in Fig. 4.32, which allows the deformation in the direction of the thickness of the gap but seals the wool and prevents the dispersion of pieces of wire.

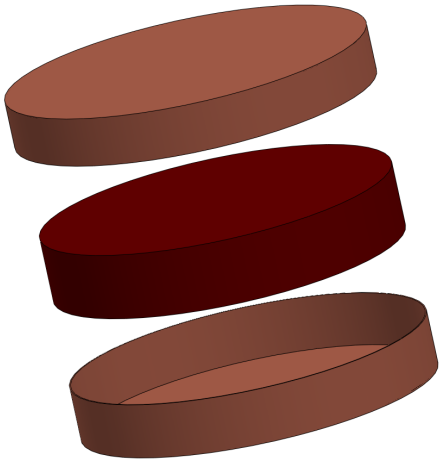

(a) Exploded view of the two copper glasses with the copper wool in the middle.

(b) Detailed section view of the two glasses with the copper wool sealed in the middle.

Fig. 4.32: Copper wool case designed to prevent the dispersion of pieces of copper wire on the board.

4.6.5 Conclusions

Analyzing the solutions reported we notice that the only three that we can take in account are: the thermal pad, the liquid TIMs and the copper wool. While the first two are available on the market and can be bought, the last one needs the production of the "copper glasses". On the other hand the wool is for sure low outgassing and radiation hardening. Tests will be done on samples of copper wool, thermal pads and liquid TIMs to verify their real thermal conductivity, to report their values of outgassing and radiation tolerant. At the end the chosen solution will be the cheapest one among the ones which satisfy all the mentioned constraints.

Chapter 5

Experimental tests of DAQ crate and Module 0 prototypes

In this chapter we report the preliminary tests that we have performed on the DAQ crate prototype that I have designed and on the Module 0 prototype, a 10 % reduced-scale prototype of the calorimeter fully equipped with CsI crystals, prototype photo-sensors and readout electronics. We have performed the leak test and the pressure loss test on both the components. The leak test has been performed at VCS S.r.l. for the DAQ crate prototype and at Cinel S.r.l. for the Module 0. The leak test is made by closing the exit of the circuit under test and connecting the input to the vacuum pump. Then helium is dispensed around each junction and fitting with a nozzle (Fig.5.1). If the mass spectrometer, placed downstream the circuit, reveals helium, it means that somewhere there is a leak which allows the helium to get absorbed inside the pipes. In order to avoid the liquid leak, the sensitivity of the leak test result must be below $5 \times 10^{-5}\, mbar \times l/s$.

I have personally performed the pressure loss tests at the laboratory of INFN of Pisa. Fig. 5.2 shows the scheme of the experimental apparatus used to make the tests. The components we want to test (the DAQ crate or the back plate in our case) is placed in the position of the resistance rounded by the green circle.

Both pressure loss tests have been performed in two parts:

1 First we have determined the instrumental offset of the pressure loss measurement by replacing the component that we want to test with a smooth pipe, which introduce a negligible pressure loss.

2 Then we have performed the measurements with the component (DAQ crate or Module 0) connected to the apparatus.

We have then subtracted the measurements obtained in (1) from (2) and we have obtained the final curve which connects the mass flow rate to the tested component pressure loss, without the other instrumental losses due to the external measurement apparatus.

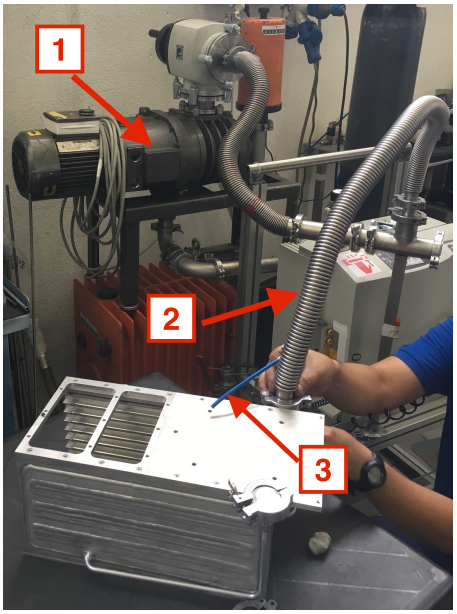

Fig. 5.1: Apparatus used for the leak test with the mass spectometer for elium: **1** Vacuum pump, **2** Mass spectometer for elium, **3** elium nozzle

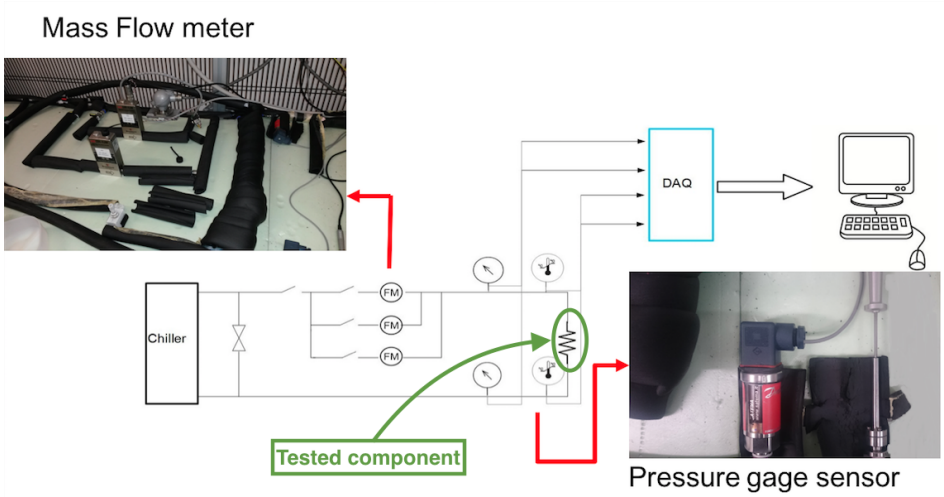

Fig. 5.2: Scheme of the apparatus used for the pressure loss test measurement. The mass flow rate is measured with a flow meter based on the Coriolis effect.

5.1 DAQ crate prototype experimental tests

We have performed the DAQ crate prototype leak test at VCS S.r.l. reaching the sensitivity of apporximately $5 \times 10^{-9}\, mbar \times l/s$, value which is under the liquid leak threshold. After we have performed the pressure loss tests at he laboratory of INFN of Pisa. Fig. 5.3 shows the crate connected to the apparatus used to estimate the pressure loss.

The graphs in Fig. 5.4 and Fig. 5.5 reports the results of the two parts of the crate pressure loss test: the measurements of the only instrumental offset and the measurements with crate connected to the apparatus. We have then subtracted the measurements obtained from the two tests and we have obtained the final curve which connects the mass

Fig. 5.3: Pressure loss test apparatus at INFN of Pisa. On the right the crate prototype conncted to the two pressure gauges.

flow rate to the actual Module 0 pressure loss, without the other instrumental losses due to the external measurement apparatus (Fig. 5.6).

In Fig. 5.4 and 5.5 the points are the measured values; the curves are quadratic polynomial fits in agreement with the general relation $\Delta P \propto Q^2$. In the top left corner of the graphs there is the equation of the fitted curve: it should be in the form $y = ax^2+bx+c$ with $c = 0$; the presence of $c \neq 0$ in Fig. 5.4 and 5.5 is due to the offset of the pressure gauge sensors. The difference between the two fitted equations gives the equation of the crate pressure loss: $y = 0.2425x^2 + 0.2463x - 0.0415$, where y is the pressure loss ΔP and x the mass flow rate Q. Since the nominal mass flow rate is $Q \approx 4.8 kg/min$ the corresponding pressure loss is $\Delta P \approx 6,73\, bar$. Appendix **??** reports the tables with the measured values.

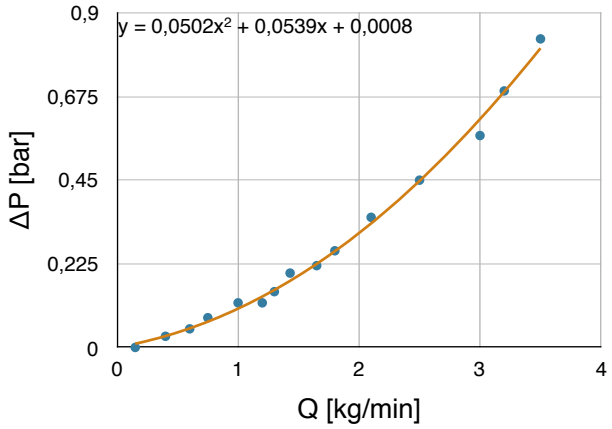

Fig. 5.4: Test with the smooth pipes mounted between the two pressure gauge sensors. The mass flow rate and the pressure drop along the circuit are respectively reported on the x and y axis.

We need to subctract the pressure losses due to the aluminum and plastic tubes which connect the crate with the two pressure gauges. They are pipes with internal diameter

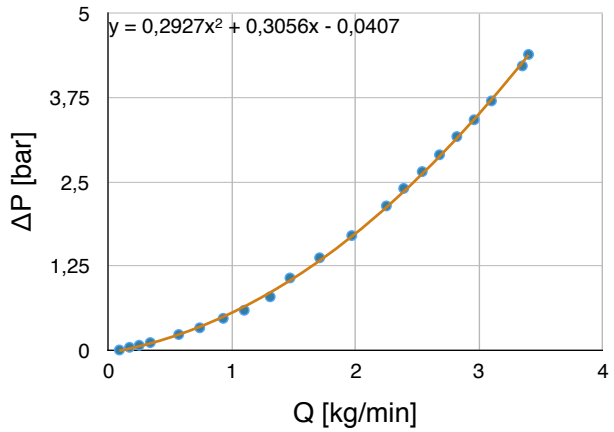

Fig. 5.5: Test with the crate prototype mounted between the two pressure gage sensors. The mass flow rate and the pressure drop along the circuit are respectively reported on the x and y axis.

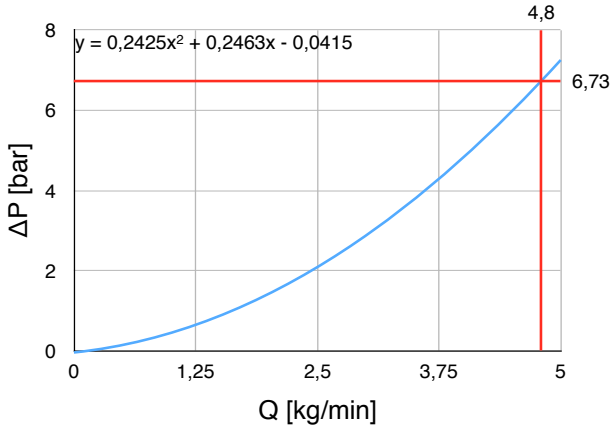

Fig. 5.6: Graph of the pressure loss of the crate prototype as a function of the mass flow rate Q, as determined from the subtraction of the fitting curves determined in Fig. 5.5 and Fig. 5.4.

$D_{in} = 4\,mm$ and their leght is approximately $1.70\,m$. The estimate pressure loss is:

$$\Delta P_{tubes} = f\frac{\rho v_f^2 L}{2D_H} \approx 3,31$$

The test has been performed with the cooling fluid at the mean temperature of $15\,°C$ instead of the approximately $-10\,°C$ of the project. At this temperature the fluid viscosity is approximately $0.0016\,Pa\,s$ instead of $0.00433\,Pa\,s$. This causes a friction factor of approximately 0.03 instead of 0.04 estimated in Chapter 3. Taking in account all this factors we obtain a pressure loss in the crate approximately of $5.1\,bar$, with a difference of approximately 10% from the $4.6\,bar$ estimated analytically in Chapter 3.

5.2 Module 0 experimental tests

5.2.1 Module 0 technical specifications and design

Module 0 is a 10 % scale prototype of the calorimeter and employs the same CsI crystals, electronics, mechanical design, including the backplane with the integrated cooling system(Fig. 5.7). Module 0 is composed of:

- the shaped aluminum ring mechanical structure;
- 51 CsI crystals;
- 102 photo-sensors and front-end electronic boards;
- the backplate which supports photo-sensors, electronics and cooling system;
- the data acquisition system.

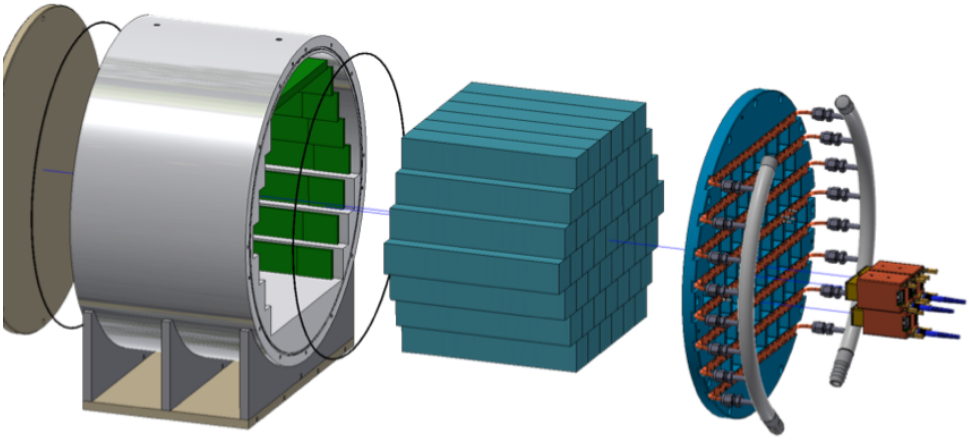

Fig. 5.7: Schematic view of Module 0.

5.2.2 Measuremnts of Module 0 leak rate and pressure loss

Module 0 has been extremely precious for my Thesis, since it has allowed to perform the pressure and thermal tests required to verify the design of the full scale detector. Given its reduced size, it does not have the central hole and the curved cooling lines. We have built Module 0 back plate as much as possible as a copy of the full scale component to validate the employed material and technology. Fig. 5.8 shows the back plate and the two extra copper lines produced to make additional thermal tests, produced by Cinel S.r.l.

Before performing the pressure loss tests with the cooling fluid, the back plate has been tested at a pressure of 20 bar to verify the leaking level using a mass spectrometer for He (helium) with helium sensitivity of $1.5 \times 10^{-10}\, mbar \times l/s$ (Fig. 5.9).

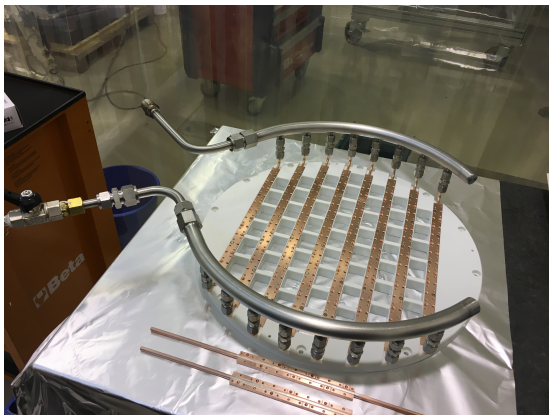

(a) Module 0 back plate.

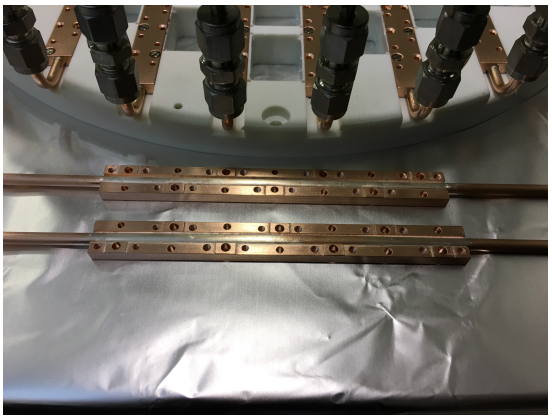

(b) The two additional copper lines with the brazed shaped profile.

Fig. 5.8: Module 0 machined by Cinel S.r.l.

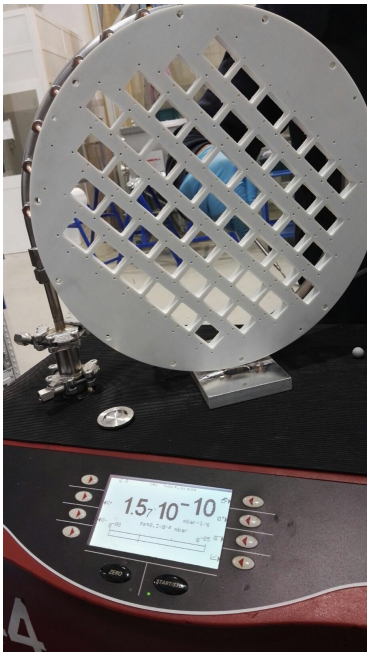

Fig. 5.9: Leak test result, made with a mass spectrometer for helium.

The graphs in Fig. 5.10 and Fig. 5.11 reports the results of the two parts of the Module 0 pressure loss test: the measurements of the only instrumental offset and the measurements with Module 0 connected to the apparatus.

We have then subtracted the measurements obtained from the two tests and we have obtained the final curve which connects the mass flow rate to the actual Module 0 pressure loss, without the other instrumental losses due to the external measurement apparatus (Fig. 5.12).

In Fig. 5.10 and 5.11 the points are the measured values; the curves are quadratic polynomial fits in agreement with the general relation $\Delta P \propto Q^2$. In the top left corner of the graphs there is the equation of the fitted curve: it should be in the form $y = ax^2+bx+c$

with $c = 0$; the presence of $c \neq 0$ in Fig. 5.10 and 5.11 is due to the offset of the pressure gauge sensors. The difference between the two fitted equations gives the equation of the Module 0 pressure loss: $y = 0.002x^2 + 0.0365x$, where y is the pressure loss ΔP and x the mass flow rate Q. Since the nominal mass flow rate is $Q \approx 12.5 kg/min$ the corresponding pressure loss is $\Delta P \approx 0.8\, bar$. Appendix **??** reports the tables with the measured values.

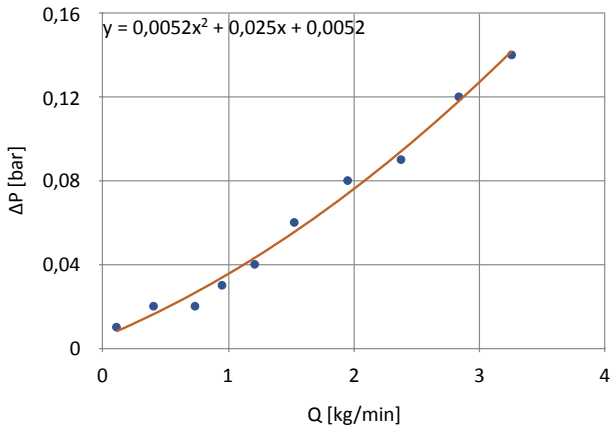

Fig. 5.10: Test with the smooth pipes mounted between the two pressure gauge sensors. OThe mass flow rate and the pressure drop along the circuit are respectively reported on the x and y axis.

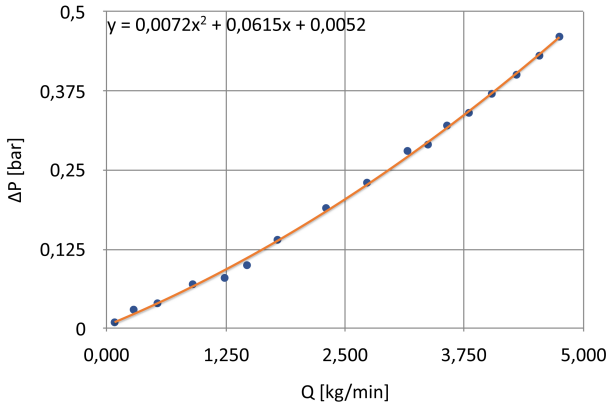

Fig. 5.11: Test with the Module 0 back plate mounted between the two pressure gage sensors. The mass flow rate and the pressure drop along the circuit are respectively reported on the x and y axis.

Once the tests have been completed, the back plate has been shipped to the INFN National Laboratories at Frascati and used to assemble Module 0 (Fig. 5.13). The detector performance has then been tested with a beam of electrons at the Frascati Beam Test Facility.

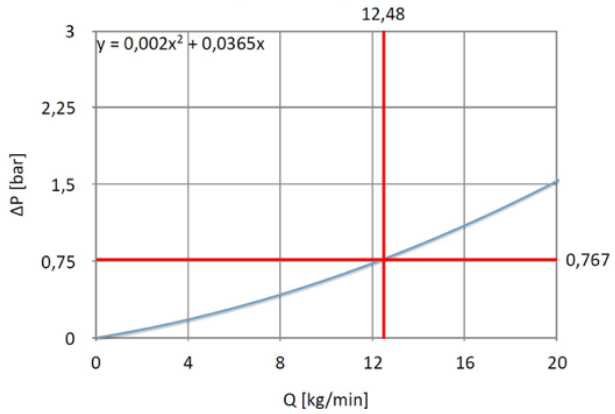

Fig. 5.12: Graph of the pressure loss of the Module 0 cooling line as a function of the mass flow rate Q, as determined from the subtraction of the fitting curves determined in Fig. 5.11 and Fig. 5.10.

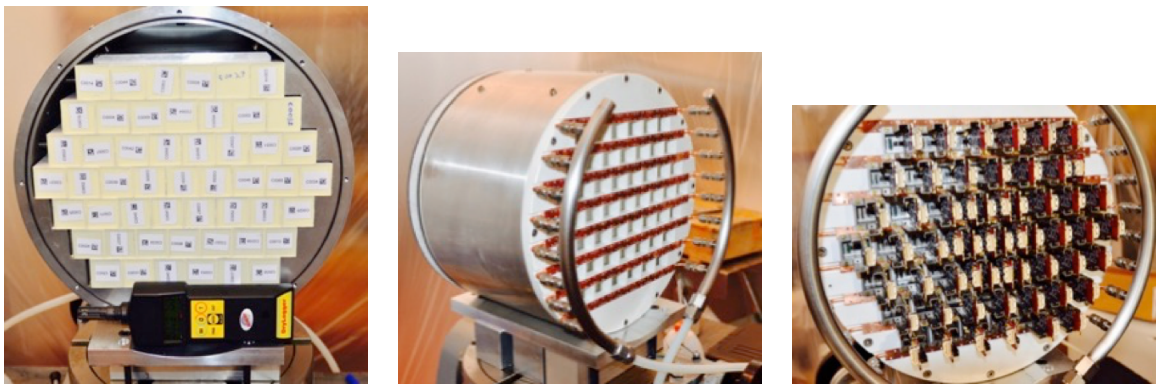

(a) 51 crystals positioned. **(b)** Back plane mounted. **(c)** 102 sensors mounted.

Fig. 5.13: Module 0 assembly at INFN Laboratory of Frascati.

Chapter 6

Conclusions and future development

The physics motivation of the Mu2e experiment at Fermilab is the search for the neutrinoless coherent conversion of a muon to an electron in the electric field of an aluminum nucleus, a physics process which would be the unambiguous evidence of the existence of physics beyond the Standard Model. The experiment is currently in construction and is expected to begin data taking in the year 2021.

The electromagnetic calorimeter has been designed and is going to be constructed by a collaboration among the Italian Istituto Nazionale di Fisica Nucleare, the California Institute of Technology, and Fermilab. It is a wide collaboration which involves many groups of physicists and engineers. I have worked with the INFN Pisa, INFN Frascati and the Fermilab groups, and I have presented the progress of my work at international meetings in Italy and at Fermilab.

My research project has been the design of the cooling system of the Mu2e electromagnetic calorimeter and the development of the integration procedures of the system in the experimental area. One of the challenges of the calorimeter cooling is that the detector is installed inside the Mu2e cryostat which is evacuated at the pressure of $10^{-4}\,torr$. This is required to reduce the interactions of beam particles and muon decay products with gas, since this may produce undesired signals in the Mu2e detectors, which may mimic the conversion electron signal searched by the experiment. In the conditions of vacuum, the power generated by the electronic components can only be dissipated through conduction.

The entire calorimeter electronics is divided in two main subsystems, with different functions and locations; the first subsystem is placed on the back side of the crystal disks and is composed of the photo-sensors and the front-end electronics; the second subsystem is located on the radially external side of the calorimeter and is composed of the data acquisition (DAQ), power and monitor boards hosted in crates. The main function of the data acquisition boards is to digitize the analog signals received from the crystals front-end electronics and transfer these data to the Mu2e data acquisition for permanent storage. The main function of the power and monitor boards is to provide the power to the front-end electronics and monitor the system performance. For this reason they are

called "interface boards".

I have mainly worked on the design and thermal analysis of the DAQ boards and crate. This is a crucial project, since the reliability and performance of all electronic components depend critically on the internal temperature. There is a total of 80 waveform digitizers and 80 interface boards per calorimeter disk, hosted in 10 DAQ crates per disk. The DAQ crates are placed externally to the disk in the radial direction. The crate function is to provide mechanical support to the boards, but also a thermal path to extract the power dissipated by the electronic components with a cooling fluid flowing in pipes brazed to the DAQ crate walls. The calorimeter cooling system is independent from the rest of the experimental apparatus and is being designed by INFN engineers as well as the cooling station. The cooling fluid is a 35 % monopropylene glycol aqueous solution. Starting from an existing conceptual layout, my research project has been the design of the architecture of the DAQ crates cooling in order to meet the temperature requirements on all the employed electronic components. The goal of the first part of my Thesis has been to develop the mechanical drawings of the DAQ crate which is made entirely in aluminum. Thanks to the strong collaboration between the INFN mechanical workshop and VCS S.r.l., we have built the first prototype of the aluminum crate. The INFN mechanical workshop has built the roof, the floor and the two aluminum plates which simulate the tungsten shield (Fig. 6.1). VCS has built the milled walls and covers of the crate (Fig. 6.2) and has been responsible of their weldings 6.3.

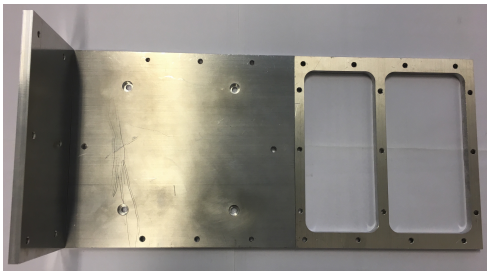

(a) DAQ crate floor.

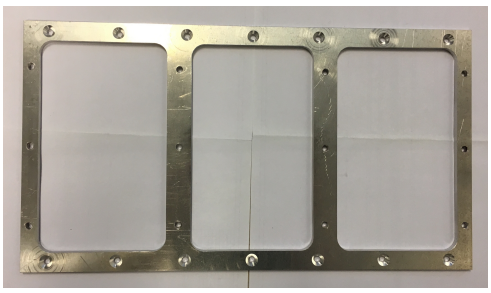

(b) DAQ crate roof.

Fig. 6.1: DAQ walls machined at the INFN mechanical workshop in Pisa.

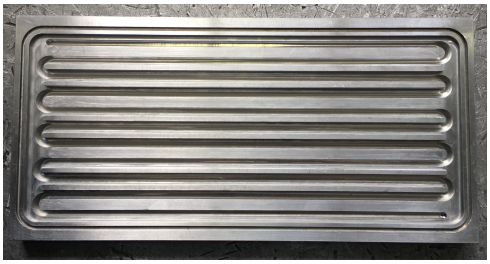

(a) Lateral wall with the milled cooling circuit.

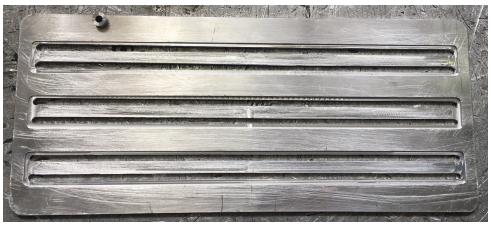

(b) Laterla wall cover.

Fig. 6.2: DAQ walls machined by VCS S.r.l.

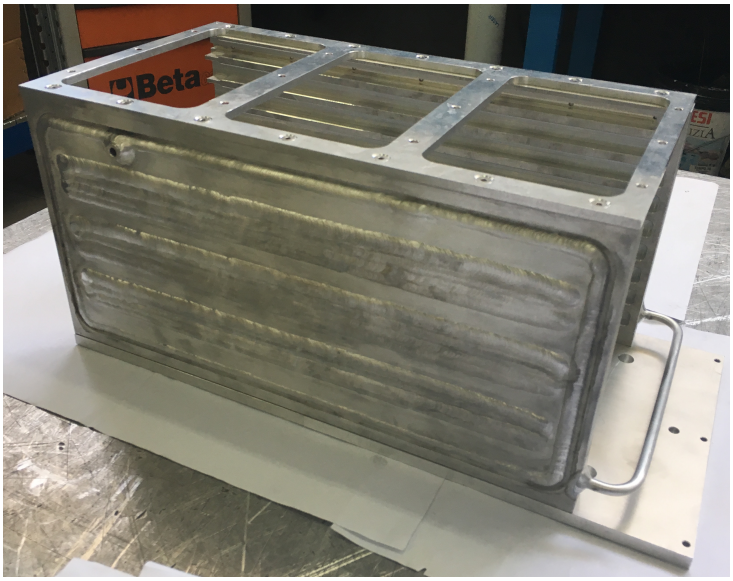

Fig. 6.3: DAQ crate assembly.

I have made the drawings of the manifolds and designed the connections between the supply and return manifold and the cooling circuit of the crates.

I have also performed the thermal analysis of the DAQ boards and of all the employed electric components. I have developed the aluminum plate which will dissipate most of the heat from the components and I have suggested three solution for the filler of the gap between the top of the components and the plate.

Future thermal, outgassing and radiation resistance tests will show the proper choice. I have also contributed to the design of the thermal-vacuum and outgassing experimental tests planned to verify the results of the simulation.To this purpose, we have recently assembled a vacuum chamber at INFN Pisa (Fig. 6.4).

The goal of the second part of my Thesis has been to perform pressure drop tests on the cooling circuiti of Module 0, the 10% reduced-scale prototype of the calorimeter; the experimental measurements have confirmed the results of my simulations.

Future tests will be made on the crate and the electronics. Thermal tests will be necessary to verify the convective coefficient of the milled cooling circuit of the crate prototype. Thermal, outgassing and radiation hardening tests will be done on samples of the three suggested solution for the gap filler. The choice of the proper filler will affect the final geometry of the aluminum plate. Also the mechanical connection between the crates and the calorimeter disks has to be designed, in order to allow the electrical connection to the ground and to avoid thermal dissipation between the crates and the disks.

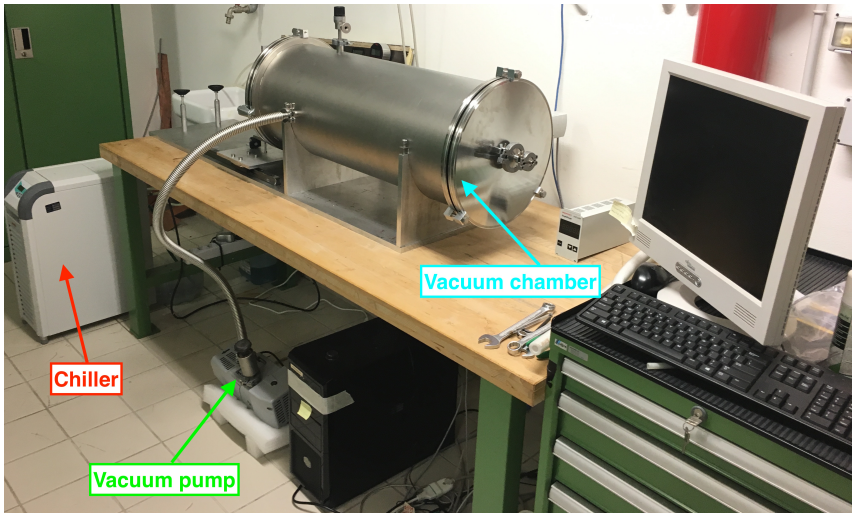

(a) Overview.

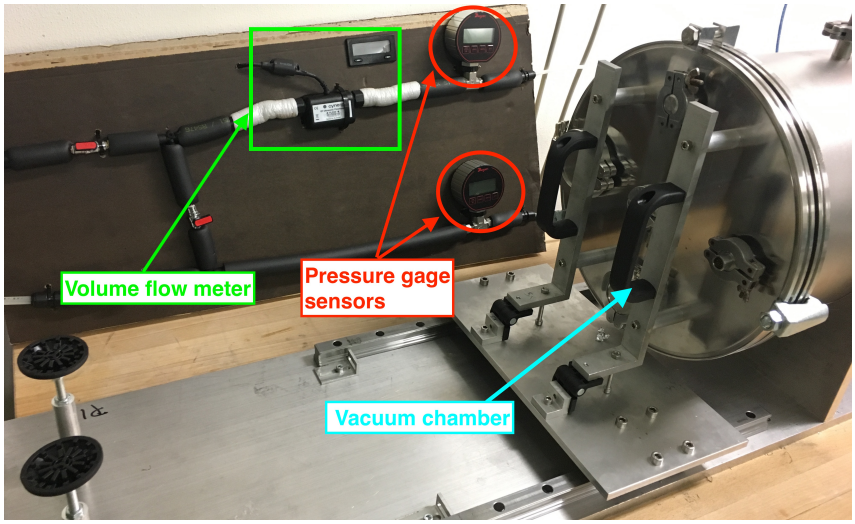

(b) Detailed view of the panel which houses the pressure gage sensors and volume flow meter.

Fig. 6.4: Vacum and cooling tests apparatus in Pisa.

Bibliography

[1] P. Aurenche, *The Standard Model of particle physics*, ENSLAPP-A- 659/97, arXiv:hep-ph/9712342

[2] C. Burgess, G. Moore, *The Standard Model a primer*, Cambridge University Press, 2006

[3] `http://www.fnal.gov/pub/about/whatis/history.html`

[4] `http://www.nobelprize.org/nobel_prizes/physics/laureates/1938/fermi-bio.html`

[5] `http://www-bd.fnal.gov/public/index.html`

[6] L. Bartoszek et al., *Mu2e Technical Design Report*, Mu2e-docdb-4299, FERMILAB-TM-2594, arXiv:1501.05241, October 2014

[7] *Mu2e Document 1169-v7*, Ron E. Ray

[8] *Mu2e Document 4872-v1*, December, 2014

[9] D. Pasciuto, *Design of the cooling system of the Mu2e electromagnetic calorimeter at Fermi National Accelerator Laboratory*, University of Pisa, 2015

[10] F. Mosti, *Design and thermal analysis of the cooling system of the Mu2e electromagnetic calorimeter at Fermilab*, University of Pisa, 2016

[11] `http://cds.linear.com/docs/en/datasheet/8033fb.pdf`.

[12] `https://www.microsemi.com/document-portal/doc_view/131095-pd3068-package-mechanical-drawings`

[13] `https://www.microsemi.com/document-portal/doc_download/132042-ds0128-igloo2-and-smartfusion2-datasheet`

[14] `http://www.analog.com/media/en/technical-documentation/data-sheets/AD9230.pdf`

[15] https://schroff.pentair.com/wcsstore/AuroraStorefrontAssetStore/User%20Downloads/Literature%20Requests/Content_schroff_cat_cat00033d_calmark_retainers_2013_en.pdf

[16] Albin K J. Hasselström, U. Eskil Nilsson, *Thermal Contact Conductance in Bolted Joints*, Diploma work no 85/2012, Chalmers University of Technology http://publications.lib.chalmers.se/records/fulltext/159027.pdf

[17] I. E. Idelchik, *Handbook of Hydraulic Resistance*, 3rd Edition, Jaico Publishing House.

[18] *Mu2e Technical Design Report (TDR)*, Mu2e Document 4299-v15, 03/23/2015.

[19] A. Palladino, J. Quirk, J. Miller, *Mu2e Stopping-Target Monitor baseline design*, Mu2e document 6453, Boston University, 06/09/2016.

List of Figures

List of Tables